Universal quantum logic in hot silicon qubits

Petit, L.

DOI
10.4233/uuid:dd646e08-9839-4c17-b5cd-867c6f1e913d

Publication date
2020

Document Version
Final published version

Citation (APA)
Petit, L. (2020). *Universal quantum logic in hot silicon qubits*. [Dissertation (TU Delft), Delft University of Technology]. https://doi.org/10.4233/uuid:dd646e08-9839-4c17-b5cd-867c6f1e913d

UNIVERSAL QUANTUM LOGIC IN HOT SILICON QUBITS

UNIVERSAL QUANTUM LOGIC IN HOT SILICON QUBITS

Dissertation

for the purpose of obtaining the degree of doctor
at Delft University of Technology
by the authority of the Rector Magnificus, Prof.dr.ir. T.H.J.J. van der Hagen,
chair of the Board for Doctorates
to be defended publicly on
Thursday 7 January 2020 at 15:00 o'clock

by

Luca PETIT

Master of Science in Nanotechnologies for ICTs, Politecnico di Torino, Grenoble INP
Phelma and Ecole Polytechnique Fédérale de Lausanne
born in Rome, Italy

This dissertation has been approved by the promotors.

Composition of the doctoral committee:

Rector Magnificus,	chairperson
Prof.dr.ir. L. M. K. Vandersypen,	Delft University of Technology, promotor
Dr.ir. M. Veldhorst	Delft University of Technology, copromotor
Prof.dr.ir. R. Hanson	Delft University of Technology
Prof.dr. W. Tittel	Delft University of Technology
Prof.dr.ir. F. Zwanenburg	University of Twente
Dr. S. De Franceschi	Université Grenoble Alpes
Dr. V. V. Dobrovitski	Delft University of Technology

Casimir PhD Series, Delft-Leiden 2020-33

ISBN 978.90.8593.459.2

An electronic version of this dissertation is available at
`http://repository.tudelft.nl/`.

CONTENTS

1

INTRODUCTION

A drop of water contains several thousand million million million atoms. Each atom is about one-hundred-millionth of an inch in diameter. Here we marvel at the minute delicacy of the workmanship. But this is not the limit. Within the atom are much smaller electrons pursuing orbits, like planets around the sun, in a space which relatively to their size is no less roomy than the solar system. Nearly midway in the scale between the atom and the star is another structure no less marvelous - the human body. Man is slightly nearer to the atom than to the star. About 10^{27} *atoms build his body; about* 10^{28} *human bodies constitute enough material to build a star.*

From his central position man can survey the grandest works of Nature with the astronomer, or the minutest works with the physicist... I ask you to look both ways. For the road to knowledge of the stars leads through the atom. And important knowledge of the atom has been reached through the stars.

Arthur Eddington

1.1. COMPUTING WITH ELECTRONS

Sometimes I find that in physics the most elementary experiments are the most fascinating. If someone asked me what the most amazing thing is that we accomplish in our labs, I would have no doubts. It is the ability to isolate and control single-electrons. Yet, this is just the starting point of any experiment, and is often followed by more sophisticated physics like quantum superposition or entanglement. Nonetheless, I think nothing beats the feeling of observing an electron jumping in and out of a quantum dot in real time. The realization of such an experiment today is relatively simple and it can be explained as a pure electrostatic effect. By applying voltages to metallic gates on top of a semiconductor, it is possible to push and pull charges, until a single particle is isolated. Using the same electrodes it is possible to tune the strength of the confinement and make the electron move in and out of its ‘prison’. I am of course neglecting here all the technology behind the experiment, such as the ability to pattern gates at the nanoscale or the use of dilution refrigerators to cool the samples down to a fraction of a degree above absolute zero. However, I still think that the basic experimental concept is incredibly simple and is within everyone’s reach.

1.1.1. FROM CLASSICAL TO QUANTUM MACHINES

The same electrons that we hope one day to use in powerful quantum computers are also the foundations of classical information. A transistor is a switch that controls a current flow, which is nothing more than a collective motion of electrons. Since the first point-contact transistor was built in 1947, the development of integrated electronics has proceeded at a tremendous pace, and has subsequently changed our day-to-day lives. From the smartphones we have in our hands to the most powerful supercomputer, from pacemakers to MRI scanners, radio stations to satellites — all these technologies are ultimately powered by the same tiny pieces of silicon. Nevertheless, there are certain tasks that are still, and will always be, far beyond our capabilities to solve. The idea of a quantum computer was formulated for the precise reason of tackling this set of problems.

Quantum computing essentially explores the implications of replacing the fundamental notions of information and computation with quantum mechanical ones [1]. Interestingly, a classical computer also, as do all physical entities, obeys the rules of quantum mechanics. However, classical information is still encoded in a binary way and quantum interactions are usually irrelevant to the calculations. Instead, in a quantum computer the single bits are defined on quantum states, which, as we learn from physics, are described by a wavefunction. While a classical computer is at any instant in time in a definite state, a quantum computer can exist in all the possible states simultaneously. This means that a computation can be sped up significantly by splitting it up into multiple channels that evolve in parallel.

Exploiting this parallelism in an efficient way is at the core of developing quantum algorithms. During a measurement, only a particular state is observed with a certain probability. It is thus necessary to make all the different states interfere with each other in order to produce a definitive outcome. When this is achieved, certain tasks can be solved more efficiently than in a classical machine. For example in Shor’s algorithm an n-digit number can be factorized in a time that is polynomial in n, instead of exponential. In some other situations the speed-up is less pronounced. It is the case of Grover’s algorithm where locating an entry in a database with n entries takes a time proportional to $\sqrt{n}$ instead of n^2. There are some other cases where using a quantum computer has no gain at all.

The set of problems where it is possible to observe a quantum speedup over competing classical computers is broad and diverse. This includes for example optimization problems [2], machine learning [3] and chemistry [4]. In particular, as claimed by Feynman [5], quantum computers should have clear advantages in the simulation of strongly correlated states of matter. The reason behind this statement is very simple: nature behaves in a quantum mechanical way, and if one wishes to simulate it, a machine based on the same quantum principles make computations far easier. A quantum computer could therefore be able to dive into the physics of complex molecules or explore new materials.

Reaching the qubit count and quality needed by practical algorithms is very challenging. Quantum systems can in fact interact with their surrounding environment and loose their quantum properties, meaning that the perfect qubit lives ideally in a fully isolated world. However, qubits must also interact with each other to be able to perform computations, so they should also couple to their surroundings to some extent. This trade off is one of the main difficulties in building and controlling quantum machines. The solution to this problem is to accept the fact that one has to deal with noisy and imperfect qubits and employ quantum error correction protocols [6]. The basic idea behind quantum error correction is to spread a single bit of information onto a multi-qubit entangled state. When the environment interacts with the single qubits, errors can be detected and corrected, while not disturbing the encoded information. The price that one has to pay is that the more noisy the qubits are the more we need to store a single bit of quantum information. That is why a future quantum computer will require millions or billions of physical qubits.

State-of-the-art quantum systems are still far from the numbers just described. However, the field of quantum computing is now developed enough to enter the so called Noisy Intermediate Scale Quantum (NISQ) era [7]. This refers to the availability of quantum systems consisting of 50 to a few hundreds of ‘noisy’ qubits. This is an interesting range because 50 is roughly the maximum number of qubits that can be simulated today on classical supercomputers, which paves the way to the first demonstrations of quantum speedup. In a recent experiment, Google has indeed claimed to have achieved quantum supremacy — the ability to perform a task on a quantum device which is out of reach for any classical computer — on a 53-qubit chip [8]. While we might still be far from solving practical quantum algorithms, the NISQ era will already allow us to explore and simulate new physics, and will mark a crucial step in the development of future quantum technologies.

1.1.2. A SEMICONDUCTOR BASED QUANTUM COMPUTER

Building a quantum computer is a formidable task and it involves expertises from many different fields: physics, engineering and computer science, just to name a few. The worldwide effort in building high-quality qubits has resulted in multiple quantum computing platforms, like superconducting circuits, ion traps, quantum dots or N-V centers, and each one of them has its key advantages. Among all platforms, quantum dots stand out for their remarkable similarities to classical transistors. One can think of them as transistors where the current comes from single-electrons; this is the characteristic that allows quantum effects to emerge. It might be somehow surprising that the same technology that led us in today's information age can also take us to the next. But again, sometime the less complicated solution can be the most successful.

Any type of qubit needs to satisfy a set of requirements, known as the DiVincenzo criteria [9], in order to be considered a viable candidate for large-scale quantum computation. These include the ability to initialize the qubits and readout their states, sufficiently long coherence times and a universal set of quantum gates. In the last decade, the field of semiconductor based quantum dot qubits has witnessed an intense development, mostly due to progress in material science, facilitating demonstrations of each of these functionalities. Compared to other qubit platforms, spin qubits have key advantages in terms of gate-speed, coherence times and small dimensions. In addition to quantum computing applications, they can also be used for quantum sensing — spins are in fact excellent magnetometers and charge detectors — and for quantum simulations [10].

The most pressing challenge now is to increase the qubit count. State-of-the-art quantum dot systems still consist of only a few qubits and the question of what is the most promising pathway to a large-scale implementation remains open. In this era of scalability, quantum dots defined in silicon have great prospects because they are based on the same technology we find in classical computers. The similarities with conventional electronics give hope that silicon quantum dots can be fabricated one day in mass-manufacturing facilities. This process has already started in recent years, with the involvement of some of the most important semiconductor companies. However, while reliable and reproducible fabrication is a crucial requirement, building a large-scale quantum computer also comes with further challenges.

This thesis addresses some of these scalability issues and discusses possible solutions. The first five chapters deal with the problem that most quantum computing platforms currently operate at temperatures close to absolute zero. While this is beneficial for the coherence times and the stability of the qubits, it also imposes strict constraints when cooling down large systems. In this thesis I explore the possibility of shifting the operating temperature of silicon spin qubits from absolute zero to the Kelvin regime. Although this might seem like a small step in temperature, it makes the cooling of larger systems substantially easier. The last chapter focuses on the problem of wiring dense arrays of spin qubits. I propose a new qubit architecture, where a large number of qubits can be controlled and manipulated with a limited number of connections. The two parts are therefore strictly related and show that spin qubits have an inherent potential to be scaled up to the numbers required by practical quantum computing applications. Overall the results presented in this thesis give prospects for a quantum computer based on the same materials and technologies that enabled the last semiconductor revolution.

1.2. THESIS OUTLINE

Chapter 2 introduces the basic properties of spin qubits in quantum dots. I review the main material platforms where electrons or holes can be isolated in electrostatically defined quantum dots, and show how their properties can be described in terms of the Fermi-Hubbard model. Then, I illustrate the experimental implementation of the Di-

Vincenzo criteria for quantum computation [9]: readout and initialization, single-qubit control and two-qubit gates. The chapter ends with a discussion of the main challenges in scaling up spin qubits and the prospects for 'hot' qubit operation.

The next three chapters contain all the necessary steps that will lead to the main result of this thesis: a universal gate-set for spin qubits beyond 1 Kelvin. All successful spin qubit experiments starts with a well-defined quantum dot system and **chapter 3** focuses on a detailed characterization of a double quantum dot at 0.5 K. Despite the high temperature, the system shows great stability, exceptional charge readout fidelity and controllable tunnel couplings, making it the ideal starting point for all subsequent experiments.

In **chapter 4** the temperature dependence of two crucial parameters, the spin lifetime and the charge noise, is investigated. The temperature dependence of the spin relaxation time is explained in terms of two-phonon transitions. The results presented here show that these two parameters do not represent a roadblock for high temperature operation.

Chapter 5 contains the main result of this thesis. Building from the results of the previous chapters, qubit control is now added. The combination of readout, high fidelity single-qubit gates and a universal two-qubit gate at a temperature of 1.1 K showcases the potential of spin qubits to be operated in quantum integrated circuit, where qubits and control electronics lie on the same chip.

Chapter 6 focuses on the optimization of two-qubit gates on the same chip operated beyond one Kelvin. I discuss the implementation of several native two-qubit gates for spin qubits, optimize the control sequences and predict high fidelities despite the elevated temperature.

Finally, **chapter 7** describes the effort of finding suitable quantum computing architectures for large-scale systems. In this context, I propose a two-dimensional qubit array that can be controlled with a limited number of gates. Despite the shared control, the architecture allows for high-fidelity single- and two-qubit gates, fast readout and shuttling, providing prospects for the operation of large-scale quantum dot systems.

Chapter 8 concludes the thesis by discussing future research directions.

REFERENCES

[1] D. P. DiVincenzo, *Quantum computation,* Science **270**, 255 (1995).

[2] E. Farhi, J. Goldstone, and S. Gutmann, *A quantum approximate optimization algorithm,* arXiv preprint arXiv:1411.4028 (2014).

[3] J. Biamonte, P. Wittek, N. Pancotti, P. Rebentrost, N. Wiebe, and S. Lloyd, *Quantum machine learning,* Nature **549**, 195 (2017).

[4] D. Wecker, M. B. Hastings, N. Wiebe, B. K. Clark, C. Nayak, and M. Troyer, *Solving strongly correlated electron models on a quantum computer,* Physical Review A **92**, 062318 (2015).

[5] R. P. Feynman, *Simulating physics with computers,* International Journal of Theoretical Physics **21** (1982).

[6] D. Gottesman, *An introduction to quantum error correction and fault-tolerant quantum computation,* in *Quantum information science and its contributions to mathematics, Proceedings of Symposia in Applied Mathematics*, Vol. 68 (2010) pp. 13–58.

[7] J. Preskill, *Quantum computing in the nisq era and beyond,* Quantum **2**, 79 (2018).

[8] F. Arute, K. Arya, R. Babbush, D. Bacon, J. C. Bardin, R. Barends, R. Biswas, S. Boixo, F. G. Brandao, D. A. Buell, *et al.*, *Quantum supremacy using a programmable superconducting processor,* Nature **574**, 505 (2019).

[9] D. P. DiVincenzo, *The Physical Implementation of Quantum Computation,* Fortschritte der Physik **48**, 771 (2000).

[10] A. Chatterjee, P. Stevenson, S. De Franceschi, A. Morello, N. de Leon, and F. Kuemmeth, *Semiconductor qubits in practice,* arXiv preprint arXiv:2005.06564 (2020).

2

QUANTUM COMPUTATION WITH SPINS IN QUANTUM DOTS

This chapter illustrates how quantum operations can be realized with electron or hole spins in semiconductor quantum dots. The first section focuses on the various material stacks used to confine and isolate electrons or holes. Next, quantum dots are described within the formalism of the Fermi-Hubbard model, with particular focus on electrons in silicon. The chapter then, continues with a review of the possible experimental implementations of initialization, readout, single- and two-qubit gates. The conclusion includes a discussion on the scalability of spin qubits and how Si-MOS quantum dots are a promising platform for high temperature operation.

2.1. SEMICONDUCTOR QUANTUM DOTS

A quantum dot is a small semiconductor island where conduction electrons (or valence holes) can be isolated using a combination of electrostatic fields and interfaces between materials. Quantum dots have usually a small size, in the range of 10-100 nm, and the particles occupy discrete energy levels, as it happens for orbitals in an atom. The number of particles in a quantum dot can be precisely set via electrostatic control. In fact, electrons and holes carry a charge that makes them subjected to Coulomb repulsion. Hence, adding an extra particle to a quantum dot requires a finite amount of energy, called charging energy E_c, inversely proportional to the capacitance C of the island. This charging energy needs to be sufficiently larger than the thermal broadening, meaning that a small island and a low enough temperature are needed. A second requirement is that fluctuations in the number of particles are negligible over the time scale at which the island is charged. This requires a quantum dot weekly coupled to its reservoir. When these two criteria are met, the number of particles can be controlled down to the single-particle level.

Out of all the degrees of freedom that can be used to encode quantum bits, the spin of a single particle is the canonical example. Electrons are spin-1/2 particles, and an external magnetic field splits in energy the spin-up and the spin-down state. These two states can then be used as the computational basis for a type of qubit known as the Loss-DiVincenzo (LD) qubit [1].

The first pioneering works with electron spins in quantum dots [2–5] have been conducted in GaAS-AlGaAs heterostructures grown by molecular beam epitaxy. In this type of devices, electrons, coming from a thin Si delta-doping layer, accumulate at the GaAs-AlGaAs interface due to the mismatch in their band edges. The quantum well confines the electrons along the z direction, while metallic gates provide confinements along the other two axis. The small lattice mismatch between GaAs and AlGaAs, together with an intense development of growing techniques, have produced devices with extremely high mobilities (up to 10^7 cm^2/Vs) and very little level of disorder. The excellent control of the potential landscape has resulted in one- and two-dimensional arrays of quantum dots with great level of uniformity and control [6] that can be used for quantum simulations [7–9]. However, the interaction with the nuclear spins through the hyperfine coupling has limited qubit experiments.

More recently silicon has emerged as a promising platform for quantum computation. Natural silicon consists for 95% of zero-spin nuclei (^{28}Si and ^{30}Si) and can be further purified to nearly 100% non-magnetic isotopes. As a consequence, the effects of the hyperfine interaction are dumped by several orders of magnitude and this has resulted in the longest coherence times ever reported in quantum dots [10]. Spins in silicon can be defined in Si-SiGe heterostructures or at the Si-SiO$_2$ interface in metal-oxide-semiconductor (MOS) devices. In the first approach electrons are confined at the interface between strained silicon and silicon-germanium. Metallic gates can be either used to deplete a two dimensional electron gas (2DEG) induced by modulation doping (depletion mode) or to directly accumulate electrons (accumulation-mode). The attractive feature of Si-SiGe hetereostructures is the epitaxial interface, which results in mobilities of the order of 10^6 cm^2/Vs. As for GaAs, this facilitates the formation of low-disorder quantum dots that can be tuned up to a high degree of control. In silicon, the largest

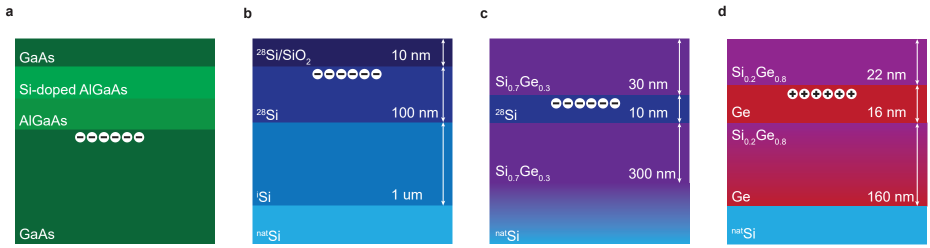

Figure 2.1: **a-d** Substrate schematics for GaAs (**a**), Si-SiO$_2$ (**b**), Si-SiGe (**c**), Ge-SiGe (**d**) devices. The dimensions refer to the structures grown in Qutech.

arrays of quantum dots have indeed been reported in Si-SiGe [11].

On the other hand, in MOS devices electrons are confined at the Si-SiO$_2$ interface, with a structure that greatly resembles classical transistors. The compatibility with conventional manufacturing technologies gives excellent prospects for a quantum computing platform that can be scaled up to millions of qubits. First of all, the know-how of the CMOS industry can be leveraged to improve yield, reproducibility and uniformity of quantum dot devices. Secondly, as we will see in the final section of this chapter, it can also be exploited for the realization of quantum integrated circuits where qubits and control electronics reside on the same chip. Isotopically enriched ^{28}Si/^{28}SiO$_2$ stacks have already been manufactured on 300 mm wafers in an industrial fab [12] and qubit experiments on these gate stacks have also been performed [13–16] paving the way to industrial spin qubits manufacturing. Compared to epitaxial structures, MOS devices have interfaces of lower quality with mobilities usually between 10^3-10^4 cm^2/Vs. This brings additional challenges in terms of limited uniformity, larger charge noise and in general a more complicated device tuning. However, as already discussed, significant improvements can be expected by moving from academic to industrial manufacturing facilities.

Finally, planar germanium heterostructures have also recently emerged as a compelling qubit platform for quantum computation and simulations [17, 18]. Here holes, instead of electrons, can be defined in a germanium quantum well deposited on a SiGe strained substrate. Germanium has one of the highest hole-mobility out of all semiconductors, exceeding 10^6 cm^2/Vs, which results in well controlled and uniform quantum dots. Furthermore holes have an intrinsic spin-orbit coupling that can be exploited for fast and fully electrical qubit control without the need of macroscopic structures such as local magnets or antennas. Most metals have also a Fermi level pinned to the valence band, which results in a strong coupling between metal and semiconductor material [19]. These unique characteristics make germanium a compelling platform for building hybrid quantum devices based on spins, topological states and superconducting structures.

2.2. MODELLING ELECTRONS IN QUANTUM DOTS

A system of coupled quantum dots can be efficiently described in terms of the extended Fermi-Hubbard model. In this description electrons are treated as weakly interacting particles in a simplified lattice, where each site represents a quantum dot. The hamiltonian of such a system reads as follows:

$$H = H_{\mathrm{E}} + H_{\mathrm{t}} + H_{\mathrm{U}}, \tag{2.1}$$

where H_{E} is the on-site energy, H_{t} represents quantum tunneling between sites and H_{U} describes the Coulomb interaction. Each of the terms in Eq. 2.1 consists of a sum over the degree of freedom of the electrons. The first is of course the spin, whose states are split in an external magnetic field B_{ext} by the Zeeman energy $E_{\mathrm{z}} = g\mu_{\mathrm{B}}B_{\mathrm{ext}}$, where g is the electron g-factor and μ_{B} the Bohr magneton.

Orbital levels are a second degree of freedom. In presence of a magnetic field and a simple parabolic confining potential the particle eigenenergies follow a spectrum known as the Fock-Darwin states:

$$E_{n,l} = \hbar(2n+|l|+1)\sqrt{\omega_0^2+\frac{\omega_c^2}{4}} - \frac{l\hbar\omega_0}{2}, \tag{2.2}$$

where $\hbar\omega_0$ is the electrostatic confinement energy, $\hbar\omega_c$ the cyclotron energy and $n = 0,1,2,...$ and $l = 0,\pm1,\pm2,...$ the two quantum numbers.

In silicon quantum dots there is finally another degree of freedom to be considered: the valleys. Bulk silicon has cubic symmetry and the minimum of the conduction band is six-fold degenerate. In bulk silicon the states are degenerate, but in a 2DEG the degeneracy is broken by the in-plane strain coming from the Si-SiO$_2$ or Si-SiGe interface. As a consequence, the energy of the 4 in-plane valleys are lifted by approximately 100 meV. The remaining two-fold degeneracy along the z-direction is broken by the electric fields coming from the interface and the confinement potentials. The two bare valley states are mixed into new energy eigenstates v_+ and v_- separated by the valley splitting energy E_{VS}. The magnitude of E_{VS} depends on how strongly the electrons are confined; in MOS devices the splitting is usually of the order of 0.2-0.8 meV, while in Si-SiGe heterostructures is usually below 0.2 meV. These values can also be further tuned by the electric fields generated by the gates [10]. In a silicon quantum dot, the orbital energies are usually larger than 1 meV [20], meaning that the two (excluding the spin degeneracy) lowest lying states are v_+ and v_- of the lowest orbital. A high valley splitting is therefore highly desirable, since low values can negatively impact spin lifetimes, initialization, readout and control fidelities.

We can now expand the terms in Eq. 2.1 in the case of a double quantum dot. We focus on the lowest orbital and we rewrite the three terms in Eq. 2.1 as sums over the spin ($s =\uparrow,\downarrow$), dot number ($d = 1,2$) and valley state ($v = +,-$) degree of freedom:

$$H_{\mathrm{E}} = \sum_{|s,d,v\rangle} n\epsilon + \frac{E_{\mathrm{Z}}}{2} \sum_{|d,v\rangle} (c^{\dagger}_{\uparrow\uparrow} c_{\uparrow\uparrow} - c^{\dagger}_{\downarrow\downarrow} c_{\downarrow\downarrow}) + \frac{E_{\mathrm{VS}}}{2} \sum_{|s,d\rangle} (c^{\dagger}_{+} c_{+} - c^{\dagger}_{-} c_{-}) \tag{2.3}$$

$$H_{\mathrm{t}} = -t \sum_{|d,v\rangle} \sum_{|d',v'\rangle} (c^{\dagger}_{\uparrow,d,v} c_{\uparrow,d',v'} - c^{\dagger}_{\downarrow,d,v} c_{\downarrow,d',v'}) \tag{2.4}$$

$$H_{\mathrm{U}} = \frac{U}{2} \sum_{|d\rangle} n(n-1) + V \sum_{|d\rangle} \sum_{|d'\rangle} n_d n_{d'} \tag{2.5}$$

where ϵ is the detuning between the two dots, t the tunnel coupling between the quantum dots, U the on-site Coulomb repulsion, V the Coulomb interaction between sites, c and $c^{\dagger}$ creation and annihilation operators and n the occupation number.

2.3. SPIN INITIALIZATION AND READOUT

An electron spin carries a small magnetic moment, making direct measurements impractical. Conversely, the electron charge can be efficiently sensed using on-chip electrometers such as Single-Electron-Transistors (SETs) or Quantum-Point-Contacts (QPCs). Spin readout techniques make use of this advantage, by first converting the spin information into different charge configurations and then by reading-out the charge.

Readout of spin qubits is usually accomplished via the Elzerman technique [2]. In this method the Fermi level of a reservoir is positioned between the two spin states such that the electron in the spin excited state can tunnel out of the dot whereas the transition from the spin ground state is energetically forbidden. This method, despite the relatively simple requirements, presents also some complications. First of all, the thermal broadening in the reservoir due to the non-zero electron temperature makes the probability of a spin-down transition larger than zero. This probability depends on the ratio of electron temperature and spin splitting, given by the external magnetic field. Fig 2.2a shows the readout fidelity as a function of electron temperature and Zeeman splitting with the assumption that the thermal broadening of the reservoir is the only cause of readout errors. Even in the ideal conditions of perfect charge readout we are assuming here, a high-fidelity region can only be found in the high-field and low-temperature regime. Large Zeeman splittings can compensate for the finite electron temperature, but high magnetic fields can negatively impact the spin lifetimes and also require exceptional high frequencies for driving the qubits. Practically, even when the electron temperature is around 100 mK the fidelity is below 99 % and the method is clearly impractical for high temperature operation.

Readout based on Pauli spin blockade (PSB) overcomes these problems at the cost of an additional dot used as ancilla. Fig. 2.2b shows the eigenergies of a double dot system as a function of the detuning between the two quantum dots, as obtained from diagonalization of Eq. 2.1. When the dots are not detuned and the coupling is low enough, the eigenstates are the four isolated electron spin states: $|\downarrow\downarrow\rangle$, $|\downarrow\uparrow\rangle$, $|\uparrow\downarrow\rangle$ and $|\uparrow\uparrow\rangle$. As we increase the detuning it becomes favorable for the electrons to occupy new states: the S(0,2) where the spins are in the lowest valley v_{-} of the same quantum dot and the four states where the spins are still in the same quantum dot but in different valleys, S_0(0,2), T_0(0,2), T_+(0,2), T_-(0,2). In the S(0,2) the spins must be in a singlet configuration and

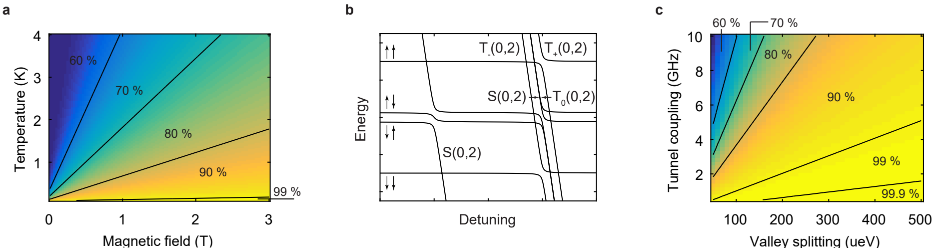

Figure 2.2: **a** Spin to charge conversion fidelity as a function of magnetic field and temperature. At each point the readout time is optimized according to the tunneling rates. Fidelities higher than 99 % can only be found in the regime T < 150 mK and B > 0.6 T. **b** Energy levels of two electrons in a double dot, as obtained from diagonalization of the hamiltonian in Eq. 2.1. The energy differences are exaggerated for clarity. c Spin to charge conversion fidelity in a scheme that employees PSB, as a function of tunnel coupling between the electrons and valley splitting.

therefore, out of the four isolated electron spin states, only the antiparallel one with the lowest energy couples to it, while the other three are blocked from tunneling because of Pauli exclusion principle. By detuning the two quantum dots even further, the high-energy valley becomes also energetically accessible and the blockade is lifted. If we focus on the subspace $|\downarrow\downarrow\rangle$-$|\downarrow\uparrow\rangle$ there is a detuning window, which equals the valley splitting energy, where it is possible to perform single-spin readout since the spins will tunnel into the same quantum dot only if antiparallel. In this readout scheme the relevant energy scale is therefore the singlet-triplet energy splitting, equal to E_{VS}. In particular in Si-MOS devices this splitting is large enough to make the readout scheme relatively independent of the electron temperature. Furthermore, readout fidelities do not depend on the external magnetic field, allowing independent tuning of the qubit resonance frequencies. Finally, readout based on PSB does not require any external reservoir making possible to readout spins also in large two-dimensional arrays of quantum dots. As we will see in chapter 4, removing 2DEGs in the proximity of the qubits can also significantly benefit their spin lifetimes.

A key point for the readout performance is the impact of the valleys. The optimal detuning position depends on the valley splitting E_{vs} and the tunnel coupling t_0. When the intra and inter-valley tunnel coupling are equal, the best readout position is $\epsilon = U + E_{\mathrm{vs}}/2$. Smaller detuning values decrease the probability that $|\downarrow\uparrow\rangle$ tunnels to the (0,2) charge state, while larger values increase the tunneling probability of the $|\downarrow\downarrow\rangle$ state. Fig. 2.2c shows the readout fidelity as a function of t_0 and E_{vs}. When the tunnel coupling is tuned to $\approx 1-2$ GHz, a valley splitting of 200 µeV is enough to get fidelities higher than 99%. Such values of valley splitting are routinely measured in Si-MOS samples, and can be tuned to even higher values by increasing the electric fields. A high fidelity conversion fidelity requires also to move adiabatically between the spin states to avoid ending up in an eigenstate mixture. The pulse speed depends on the value of tunnel coupling, and can be optimized by pulse shaping. Overall, readout fidelities beyond 99% using Pauli spin blockade are readily achievable and have indeed been reported in literature [21].

Initialization can be performed in an analogous way as readout. By starting in a singlet S(0,2) charge state the detuning between the two dots can be adiabatically decreased

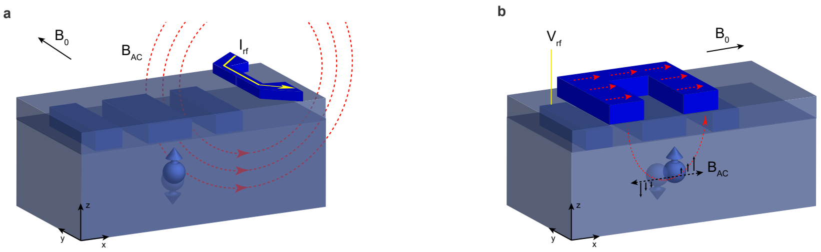

Figure 2.3: **a-b** Schematics of the two main driving techniques for spin qubits. In **a**, an AC current delivered to an on-chip microwave stripline generates a time dependent magnetic field B_{AC} perpendicular to the external magnetic field B_0. In **b** the electron is displaced in a magnetic gradient generated using an on-chip micromagnet, resulting in an effective B_{AC} perpendicular to B_0.

and the system initialized in the lowest antiparallel energy spin state. In order to achieve a good initialiation fidelity, the pulse speed must be slow enough compared to the tunnel coupling and the Zeeman difference between the two electrons. As for the readout, this initialization scheme is also relatively insensitive to the operating temperature.

Once the spin has been converted to charge, this needs to be readout. In the experiments discussed in this thesis, charge readout occurs by monitoring the DC current of an-on chip Single-Electron-Transistor via a room temperature I-V converter [2, 22]. In this case the detection bandwidth can be limited either by the signal-to-noise ratio or by the cut-off of the room temperature amplifier and its upper bound is usually around tens of KHz. In future experiments the detection bandwidth could be improved by using cryogenic amplifiers [23] or by connecting an rf tankcircuits to the ohmic of the sensor [24, 25]. Alternatevely it is also possible to use gate-based rf reflectometry to measure the change in quantum capacitance caused by the tunneling of electrons [26–28]. In all these cases it is possible to achieve detection bandwidths around 1 MHz.

2.4. SINGLE-QUBIT CONTROL

The electron spin degeneracy can be lifted by applying an external magnetic field B_{ext}. Spin transitions can then be obtained by applying a perpendicular oscillating magnetic field B_{AC} resonant with the energy splitting $g\mu_{\text{B}}B_{\text{ext}}$, where g is the electron g-factor and μ_B the Bohr magneton. For electrons in quantum dots different techniques can be used to deliver this oscillating magnetic term.

As shown in Fig. 2.3a, one first possibility is to perform electron-spin-resonance (ESR) using on-chip trasmission lines [4, 10, 29] designed to maximize the high frequency magnetic fields and at the same time minimizing electrical fields that could deteriorate the qubit performance. This method has been proven to achieve control fidelities exceeding 99.9 % [30], with driving speeds usually of the order 1-2 MHz. The use of ESR poses the challenge of qubit addressability, since the magnetic fields are applied to all qubits simultaneously. However, local g-factor variations in Si-MOS due to spin-orbit coupling result in Zeeman energy differences of around 40 MHz per Tesla, which can be further tuned with electric fields [10]. This means that spins can be addressed with high fidelity at MHz speeds down to very low magnetic fields. Higher driving speeds can in principle still be achieved by using pulse engineering techniques such as GRAPE [30], but at high powers self-heating can become the limiting factor.

Alternatively, as shown in Fig. 2.3b, the electron spin can be controlled via electron dipole spin resonance (EDSR), by shaking the electron in a magnetic field gradient induced by local micromagnets. The latter case offers also a convenient way to tune the qubit resonance frequencies, by using the transverse field for driving and the longitudinal field for qubit addressability. However, the same longitudinal fields can introduce a channel for spin decoherence in presence of charge noise. Driving with EDSR is routinely done for Si-SiGe quantum dots where fidelities exceeding 99.9 % have been obtained at a driving speed of 30 MHz [31]. In Si-MOS, where the electron wave function is less movable because of the strong confinement, EDSR has only recently been demonstrated [32, 33].

Alternatively, the intrinsic spin orbit coupling can be exploited to perform EDSR, since it couples the momentum and the spin degree of freedom. However, silicon has a weak spin-orbit coupling and EDSR can be achieved using hole as spin states [34], or by taking advantage of the valley-orbit coupling [35].

2.4.1. QUANTUM COHERENCE

The dephasing time is a fundamental concept in quantum computing, since it characterizes the timescale in which a quantum state looses its coherence. An electron spin in a superposition state, evolves in an external magnetic field B_{ext} according to: $\psi = (|\uparrow\rangle + |\downarrow\rangle\, e^{i g u_{\text{B}} B_{\text{ext}} t/\hbar})/\sqrt{2}$.

However, due to interactions with the environment, the phase evolution will become unknown after a time T_2. For an ensemble of spins, this timescale is usually masked by a much faster dephasing due to inhomogeneous broadening. In an experiment consisting of a single spin, there is no averaging over a spatial ensemble, but temporal averages are needed to measure the probability amplitudes for the qubit state. This kind of averaging also leads to a fast dephasing, defined by a timescale T_2^*, that can be extracted as the decay of Ramsey fringes.

In not isotopically enriched samples, like GaAs or natural Si, the dephasing time is limited by the magnetic fluctuations coming from the nuclei which effectively modify the Larmor frequency at which the spin processes. In isotopically purified silicon, the magnitude of these fluctuations is dumped by 1-2 orders of magnitude and this has allowed for the longest coherence times ever measured in quantum dots [10]. However, even in isotopically enriched samples, residual ^{29}Si nuclear spins can still limit the dephasing times, in particular at very low magnetic fields since nuclear spin flip probabilities scale as the inverse of the external magnetic field [36].

Even when the noise coming from the nuclei is suppressed other factors can limit the coherence, such as charge noise. Electrical fluctuations can couple in as an effective magnetic noise via different mechanisms. As discussed in the previous section, magnetic field gradients coming from micromagnets can introduce a channel for decoherence and this has been observed to be a limiting factor in Si-Si/Ge devices [31]. In the absence of these gradients electrical noise can still couple in via Stark-shift of the electron g-factor or detuning and tunnel coupling noise when the exchange interaction is not zero [3, 37].

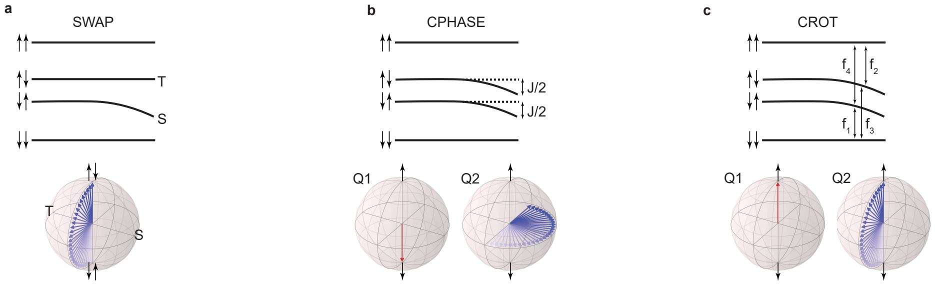

Figure 2.4: **a** When the exchange interaction dominates over the difference in Zeeman energy between the qubits, the eigenstates of the hamiltonian in Eq. 2.6 become the singlet and triplet states. If the system is initialized in the $|\downarrow\uparrow\rangle$, the evolution will be perpendicular to the singlet-triplet axis in the Bloch sphere. By tuning the interaction time, the population can be completely swapped to the $|\uparrow\downarrow\rangle$. **b** When the Zeeman interaction is dominant over the exchange, the eigenstates of the system remain approximately $|\downarrow\uparrow\rangle$ and $|\uparrow\downarrow\rangle$. In this case, an exchange pulse adds some phase to the antiparallel spin states. This effect can be seen in a Ramsey-like experiment where the system is first put in a state superposition $|\psi\rangle = |\downarrow\downarrow\rangle + |\downarrow\uparrow\rangle$ and then an exchange pulse brings the state to $|\psi\rangle = |\downarrow\downarrow\rangle + |\downarrow\uparrow\rangle e^{i\phi}$ **c** When the exchange interaction is non zero, the resonance frequencies of each of the qubit split in two, allowing for controlled rotations based on the state of the controlled qubit. The effect of driving the transition f_2 is schematically shown in the two bloch shperes.

2.5. QUBIT-QUBIT INTERACTION

As we discussed in the previous paragraphs, the behavior of electrons in a double quantum dot can be described in terms of the Fermi-Hubbard model. Two-qubit gates can be performed by tuning the system close to the (1,1)-(0,2) charge state anticrossing and by making use of the coupling between the singlet states S(1,1) and S(0,2). Furthermore, the generally large valley splitting in Si-MOS devices, allows to restrict the dynamics only on the lowest valley state. Under these assumptions the hamiltonian in Eq. 2.1 can be rewritten in the basis $\{|\uparrow\uparrow\rangle, |\uparrow\downarrow\rangle, |\downarrow\uparrow\rangle, |\downarrow\downarrow\rangle, S(0,2)\}$ as follows [38, 39]:

$$H = \begin{pmatrix} \bar{E}_Z & 0 & 0 & 0 & 0 \\ 0 & \Delta E_Z/2 & 0 & 0 & t_0^* \\ 0 & 0 & -\Delta E_Z/2 & 0 & -t_0^* \\ 0 & 0 & 0 & -\bar{E}_Z & 0 \\ 0 & t_0 & -t_0 & 0 & \varepsilon - U \end{pmatrix}, \tag{2.6}$$

where, $\bar{E}_Z$ is the mean Zeeman energy of the two dots, ΔE_Z the difference in Zeeman energy, t_0 the bare tunnel coupling, ϵ the detuning between the two quantum dots and U the onsite interaction. Using perturbation theory and considering $|\epsilon - U| \ll t_0$ one can get rid of the off diagonal terms between the antiparallel spin states and the S(0,2) state and obtain the following hamiltonian in the basis $|\uparrow\uparrow\rangle, |\uparrow\downarrow\rangle, |\downarrow\uparrow\rangle, |\downarrow\downarrow\rangle$:

$$H = \begin{pmatrix} \bar{E}_Z & 0 & 0 & 0 \\ 0 & \Delta E_Z/2 - J/2 & J/2 & 0 \\ 0 & J/2 & -\Delta E_Z/2 - J/2 & 0 \\ 0 & 0 & 0 & -\bar{E}_Z \end{pmatrix}, \tag{2.7}$$

where J is the exchange interaction given by:

$$J = \frac{t_0^2}{U - \epsilon - \Delta E_Z/2} + \frac{t_0^2}{U + \epsilon - \Delta E_Z/2}. \tag{2.8}$$

Gaining control over J is the key to perform two-qubit gates between the electron spins. In experiments J can be controlled either by dynamically pulsing the detuning ϵ or the tunnel coupling t_0. The first implementation can be easily realized by controlling the voltage on the plunger gates of the qubits, while the second one requires an additional barrier gate to directly control the coupling. Electrical fluctuations can directly modulate J through the detuning and severely impact the two-qubit gate performances. This effect can be mitigated by controlling J via the tunnel coupling and working at the so called symmetry point $\epsilon = 0$ where $\partial J(\epsilon = 0, t_0)/\partial\epsilon = 0$ and J is therefore to first order insensitive to detuning noise [40, 41].

The explicit form of two-qubit interaction depends on the ratio $J/\Delta E_Z$. In the following we will consider the various native two-qubit gate options for spins in quantum dots.

2.5.1. SWAP

When $J/\Delta E_Z \gg 1$ the hamiltonian can be approximated in the antiparallel spin states subspace as:

$$H = \begin{pmatrix} -J/2 & J/2 \\ J/2 & -J/2 \end{pmatrix}, \tag{2.9}$$

which means that the eigenstates of the system are $|\uparrow\downarrow\rangle, |\downarrow\uparrow\rangle$ for $J = 0$ and $S = (|\uparrow\downarrow\rangle - |\downarrow\uparrow\rangle)/\sqrt{2}$, $T = (|\uparrow\downarrow\rangle + |\downarrow\uparrow\rangle)/\sqrt{2}$ for J sufficiently large. By diabatically pulsing J from 0 to $\bar{J}$ the two antiparallel spin states will oscillate, resulting in a SWAP gate [1]. By timing the interaction such that $t = 1/2\bar{J}$, a $\sqrt{SWAP}$ can be realized in tens of nanoseconds. This is a universal two-qubit gate; as an example a CPHASE gate can be constructed out of two $\sqrt{SWAP}$ and single-qubit phases.

Clearly a perfect $\sqrt{SWAP}$ gate is realized only when $\Delta E_Z = 0$, a condition hardly met in experiments since a finite Zeeman difference is required for single-qubit control. However, with additional measures a high fidelity $\sqrt{SWAP}$ can still be realized even in presence of a finite Zeeman difference. One possibility is to drive the exchange in resonance with the frequency difference between the two qubits. In this way, unwanted rotations due to the finite Zeeman difference are effectively canceled out [42]. Alternatively, composite pulses can be used to overcome the finite Zeeman difference. These sequences will be discussed in detail in chapter 6.

2.5.2. CPHASE

The regime $J/\Delta E_Z \ll 1$ is instead convenient to realize a CPHASE gate. This condition is accurately met in devices with micromagnets, where it is possible to obtain Zeeman differences $\Delta E_Z > 100$ MHz. In this regime, the eigenstates of the double quantum dot system will remain $|\uparrow\downarrow\rangle, |\downarrow\uparrow\rangle$ even when $J \neq 0$, however the antiparallel spin states will acquire a phase with respect to the parallel spin states. The evolution can be therefore described by the unitary:

$$U = \begin{pmatrix} 1 & 0 & 0 & 0 \\ 0 & e^{i\phi_1} & 0 & 0 \\ 0 & 0 & e^{i\phi_2} & 0 \\ 0 & 0 & 0 & 1 \end{pmatrix}. \tag{2.10}$$

When the condition $\phi_1 + \phi_2 = \pi$ is met then the gate corresponds to a universal controlled π-phase gate (CPHASE) up to single qubit phases. As for a SWAP, this two-qubit gate can be realized in tens of nanoseconds and a fidelity of 92 % has been reported in the case of Si-SiGe sample with micromagnets [43].

Unwanted SWAP evolutions due to the finite J can in principle induce errors. These can be suppressed by pulsing the exchange adiabatically, such that the system is always in an instantaneous eigenstate of the hamiltonian. With this expedient a high-fidelity CPHASE gate can also be realized when ΔE_z is comparable to J, at the cost of a longer gate time. Shaped pulses can significantly suppress the ramping time needed to move between the hamiltonian eigenstates and shorten the gate time. Alternatively, J can be calibrated in a way that the total gate duration is synchronized with the unwanted exchange oscillations, such that the gate performs a CPHASE evolution while the SWAP oscillations performs a complete cycle [44]. This approach will also result in a faster gate time. An implementation of such a gate will be discussed in chapter 6.

2.5.3. CROT

When the exchange interaction $J = 0$, the two qubits have resonant frequencies $f_{q1} = \bar{E}_z - \Delta E_z$ and $f_{q2} = \bar{E}_z + \Delta E_z$. Turning on the exchange interaction lowers the energy of the antiparallel spin states with respect to the parallel ones and consequently f_{q1} and f_{q2} are each split into two more resonances [45]:

$$f_1 = \bar{E}_z - \sqrt{J^2 + \Delta E_z^2}/2 - J/2 \tag{2.11}$$

$$f_2 = \bar{E}_z - \sqrt{J^2 + \Delta E_z^2}/2 + J/2 \tag{2.12}$$

$$f_3 = \bar{E}_z + \sqrt{J^2 + \Delta E_z^2}/2 - J/2 \tag{2.13}$$

$$f_4 = \bar{E}_z + \sqrt{J^2 + \Delta E_z^2}/2 + J/2. \tag{2.14}$$

corresponding respectively to the transitions ($|\downarrow\uparrow\rangle \longrightarrow |\downarrow\downarrow\rangle$), ($|\uparrow\uparrow\rangle \longrightarrow |\uparrow\downarrow\rangle$), ($|\downarrow\downarrow\rangle \longrightarrow |\uparrow\downarrow\rangle$) and ($|\downarrow\uparrow\rangle \longrightarrow |\uparrow\uparrow\rangle$). Practically this means that it is possible to realize controlled rotations (CROTs), since driving one of the frequencies corresponds to drive a qubit depending on the state of the other one. This gate is equivalent to a CNOT gate apart from single-qubit phases to be applied on the control qubit.

A high-fidelity implementation of a CROT gate requires canceling out effects coming from off-resonant driving. The main source of errors comes from crosstalk between frequencies f_1, f_2 and f_3, f_4, since they are only separated by J. This crosstalk can be removed by appropriately timing the pulses according to [45]:

$$T_{\pi/2} = \frac{\sqrt{16n^2-1}}{4J}, \text{ where } n \geq 1$$

where $T_{\pi/2}$ is the time needed to complete a $\pi/2$ rotation. As for any two-qubit gate based on exchange, it is clear that the smaller J the slower the gate will be; larger J means faster operations but also larger sensitivity to electrical noise. A trade off must be therefore taken into account.

Compared to the CPHASE and SWAP gates, a CROT requires microwave driving, resulting usually in a lower gate speed. However, while the other gates require switching J on and off, a CROT can be implmented even with constant J, alleviating the requirements on quantum dot control. In Si-MOS devices this gate has been used to perform two-qubit randomized benchmarking [16, 46], yielding fidelities up to 98 %.

2.6. SCALING UP SPIN QUBITS

Electron spins in Si-MOS quantum dots have remarkable similarities with conventional CMOS technology, which enabled today's information age. This resemblance is of course an advantage when it comes to scale up these systems and it suggests that the same techniques used to build modern CPUs can be employed for large quantum dot systems, hosting million of qubits. However, this notion of scalability is clearly oversimplified and controlling such large amount of qubits involves many challenges ranging from architectures to long range coupling mechanisms and efficient readout schemes.

One of the major differences of today's quantum chips and conventional processors is the ratio of input-output connections (IOs) [47]. A recent high-end CPU contains over a billion of transistors, but the number of pins coming out of the chip is only in the range of the thousands. This makes the processors faster, affordable and easy to manufacture. Unfortunately, the same concept does not apply to quantum devices, where the number of connections is usually higher than the number of qubits. As we will see in the next chapters, a 3-qubit chip might require up to 12 connections, including 3 gates, 4 barriers, one reservoir, one SET and one microwave line. These connections need to be routed from the milliKelvin plate of a dilution refrigerator all the way up to the room temperature equipment. It is clear that this approach will not allow qubits to scale up to the millions required by practical algorithms. At the chip level a large number of control lines creates problems of fan out, and ultimately it is limited by the number of pins that can physically be connected to the device. Furthermore, wiring so many lines from room temperature to the quantum device causes an heat load that is incompatible with the cooling power available at the coldest stage of a dilution refrigerator.

Several strategies have been envisioned to tackle this interconnect bottleneck. At the device level, the number of connections required per qubit can be drastically reduced by combining two dimensional quantum dot arrays and a crossbar gating scheme, in analogy to modern dynamic random access memories (DRAMs). An example of such a scheme will be discussed in detail in chapter 7. The basic idea is that the same gates can be used to control the occupation and the coupling of several quantum dots. If this method greatly decrease the number of connections needed, on the other hand poses stringent requirements on the uniformity of the quantum dots. The involvement of industry is therefore crucial to improve yield and overall uniformity of the devices.

A second strategy to reduce the number of IOs is the integration of qubits and control electronics on the same chip, inspired by the similarities between quantum dots and classical transistors [48–50]. In the ideal scenario, pulse generation, microwave signals and digital-to-analogue converters (DACs) can all be realized on-chip such that only digital signals would flow from the chip up to room temperature. However, the extremely low temperatures at which qubits currently operate pose serious constraints to such integration. Modern dilution refrigerators make use of a ^{3}He/^{4}He mixture, which provides a cooling power of tens of μW at temperatures around 10 mK, not large enough to sustain the power dissipation of complex circuits. On the other hand, temperatures around 1-4 Kelvin can be reached with a combination of pulse tube coolers and a vacuum-pumped ^{4}He bath, which easily provide cooling powers of the order of Watts. Consequently, much more complex functions can be integrated on chip and the IOs reduced substantially.

A higher operating temperature is beneficial for the integration of the electronics on the same chip, but it also clearly affects qubit operation. Out of all the different quantum dot platforms, Si-MOS devices have the most potential to work at higher temperatures. The strong quantum dot confinement produces charging energies and orbital energies around 10 mV, much larger than the thermal energy at 4 K, which is 340 μeV. Additionally, the strong vertical confinement at the Si-SiO$_2$ interface guarantees a valley splitting of several hundreds of μeV. This high energy splitting is needed to achieve 'hot' spin readout and initialization using PSB and also to prevent unwanted excitations to higher states. As it will be discussed in chapter 4, the spin relaxation time strongly depends on temperature due to the onset of two-phonon processes. However, spin qubits have in general very long T_1 times, often in the order of seconds, and this gives enough margin to compensate for the steep T_1 rise as a function of temperature. Another key point is the impact of charge noise. Larger thermal fluctuations can in fact increase the low and high frequency noise coming from two-level fluctuators, which can negatively impact single and two-qubit gates. As discussed in chapter 4, the charge noise is only moderately affected by the temperature and this allows to still achieve good qubit control, as shown in chapter 5 and 6.

It is important to highlight that moving from academic to industrial cleanrooms can drastically improve the robustness of spin qubits to thermal noise. While the spin lifetime can ultimately be limited by the interaction with phonons, the valley splitting and the charge noise strictly depends on the material and interface quality. In particular for Si-MOS, significant improvements can be expected in this area by leveraging the process control and the state-of-the-art manufacturing lines developed for scaled transistors.

2.7. EXPERIMENTAL SETUP

The experiment in chapter 4 has been conducted in a dilution refrigerator Bluefors LD400 with a base temperature of around 10 mK, while the experiments in chapters 3, 5 and 6 in a dilution refrigerator Bluefors LD-HE with a base temperature of around 500 mK. In both cases the temperature control is achieved by controlling the circulation of ^{3}He/^{4}He and by using heaters located at the mixing chamber and the still plate of the dilution refrigerators.

The samples are glued to a printed circuit board (PCB), which is anchored to the cold finger of the dilution refrigerators. The PCB supports 33 DC lines, which can be connected via a 50-pin flexible flat cable (FFC), and 10 high frequency (hf) lines connected using SMP connectors. Out of 10 hf lines, 9 are used to deliver microwave signals and fast pulses to the gates via bias tees with an RC cutoff frequency of ≈ 100 Hz. The remaining hf line can used for radio reflectometry (RF) measurements. Here, 4 lines are multiplexed, each connected to a different inductor glued on the PCB. In this way up to four different charge sensors can be connected to different LCR resonant circuits.

2.7.1. DC COMPONENTS

Starting from the PCB the 50 DC lines go through a Cu-powder filter, where high frequency signals (> 1 GHz) are attenuated via the eddy currents created in the copper grains. Then the lines are filtered in a double stage low-pass filter board, mounted to the mixing chamber or still plate of the dilution refrigerator. The cut-off frequencies are 30 Hz for the gates and 150 kHz for the ohmic contacts. From the filter board the signal reaches th room temperature matrix modules as twisted pairs, thermally anchored and fixed to every stage of the dilution refrigerator.

At room temperature DC voltages are supplied via home-built digital-to-analog (DACs) converters. These can supply voltages in the range -4 to 4 Volts with 16 bit resolution. The current of the charge sensors is monitored with a current-to-voltage (I-V) converter with a cut-off frequency of ≈ 50 kHz. In order to limit possible noise sources, the DACs and the I-V converter are part of a rack separated from the AC electronics, connected to the computer via an optic fiber and powered by batteries.

The DC signal coming out of the I-V converter is further amplified, low-pass filtered and measured with a digitizer, either a Spectrum 4421 with 16 bit resolution and a sampling rate of 250 MS/s, or a Keysight M3102A with 14 bit resolution and a sampling rate of 500 MS/s. As discussed more in detail in the next section the latter option offers faster measurements thanks to a better integration with the arbitrary waveform generator (AWG). The Keysight M3102A has also an integrated Field Programmable Gate Arrays (FPGA) that can be programmed to perform on-board averaging.

2.7.2. HIGH-FREQUENCY COMPONENTS

The hf lines are connected from the sample to the mixing chamber (or still) plate via flexible graphite-coated cables with a cut-off frequency of ≈ 1 GHz. The use of cables with graphite coating on the outside of the dielectric can help reducing triboelectric effects due to rubbing against the outer conductor [51]. For the lines carrying microwave signals for qubit driving the graphite-coated cable is replaced with a semi-rigid coax cable with a higher cut-off frequency. From the mixing chamber (or still) plate to room temperature the signal is carried in CuNi coax cables (or graphite coated cables in case of the experiment in chapter 4). The attenuation along the lines is a trade-off between maximal voltage swing on the gates and noise reduction; the gates have usually an attenuation of $\approx 15-25$ db, while the microwave lines $\approx 6-15$ db.

A key element in qubit control is the AWG. In the experiments of chapters 3 and 4 we use a 4-channels Tektronik 5014C with 14 bit resolution and a sampling rate of 1.2 GS/s, connected to the computer via an ethernet cable. The experiments of chapters 5 and 6 made instead use of two 4-channel Keysight M3202A with 14 bit resolution and 1 GS/s. The AWGs are embedded in a rack that includes also the digitizer and com-

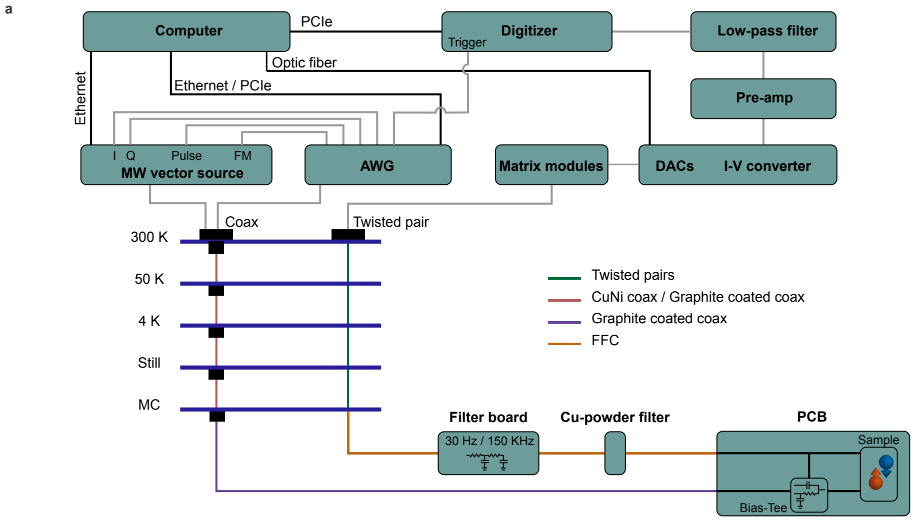

Figure 2.5: **a** Schematic of the experimental setup as discussed in the main text. The AWG channels are used to send pulses to the gates, to the IQ, pulse (PM) and frequency modulation (FM) of the microwave vector source and to the trigger of the digitizer (when not built in the AWG itself). In the case of the dilution refrigerator LD-HE, the cold finger and the filter boards are connected to the still instead of the mixing chamber plate.

municate with the computer via PCI Express. Compared to the Tektronik, the Keysight offers a much faster waveform upload ($< 10\,\text{ms}$) and it is therefore advantageous for fast measurements. Moreover, the AWGs and the FPGA on the digitizer can be programmed to perform real-time feedback, even though this feature has not been used in the experiments described in this thesis. In the future, real-time feedback could be used, for example to run quantum error-correction experiments.

The microwave signals used for qubit control are delivered via a Keysight E8267D, which provides driving in the range 250 KHz - 20 GHz and up to 30 dbm of output power. In the experiments it is possible to achieve 1 MHz Rabi frequency with $10-20$ dbm depending on the particular qubit resonant frequency.

REFERENCES

[1] D. Loss and D. P. DiVincenzo, *Quantum computation with quantum dots,* Physical Review A **57**, 120 (1998).

[2] J. Elzerman, R. Hanson, L. W. Van Beveren, B. Witkamp, L. Vandersypen, and L. P. Kouwenhoven, *Single-shot read-out of an individual electron spin in a quantum dot,* Nature **430**, 431 (2004).

[3] J. R. Petta, A. C. Johnson, J. M. Taylor, E. A. Laird, A. Yacoby, M. D. Lukin, C. M. Marcus, M. P. Hanson, and A. C. Gossard, *Coherent Manipulation of Coupled Electron Spins in Semiconductor Quantum Dots,* Science **309**, 2180 (2005).

[4] F. H. Koppens, C. Buizert, K.-J. Tielrooij, I. T. Vink, K. C. Nowack, T. Meunier, L. Kouwenhoven, and L. Vandersypen, *Driven coherent oscillations of a single electron spin in a quantum dot,* Nature **442**, 766 (2006).

[5] K. C. Nowack, F. Koppens, Y. V. Nazarov, and L. Vandersypen, *Coherent control of a single electron spin with electric fields,* Science **318**, 1430 (2007).

[6] C. Volk, A. Zwerver, U. Mukhopadhyay, P. Eendebak, C. Van Diepen, J. Dehollain, T. Hensgens, T. Fujita, C. Reichl, W. Wegscheider, *et al.*, *Loading a quantum-dot based "qubyte" register,* npj Quantum Information **5**, 1 (2019).

[7] M. Seo, H. Choi, S.-Y. Lee, N. Kim, Y. Chung, H.-S. Sim, V. Umansky, and D. Mahalu, *Charge frustration in a triangular triple quantum dot,* Physical Review Letters **110**, 046803 (2013).

[8] T. Hensgens, T. Fujita, L. Janssen, X. Li, C. J. Van Diepen, C. Reichl, W. Wegscheider, S. Das Sarma, and L. M. K. Vandersypen, *Quantum simulation of a Fermi–Hubbard model using a semiconductor quantum dot array,* Nature **548**, 70 (2017).

[9] J. P. Dehollain, U. Mukhopadhyay, V. P. Michal, Y. Wang, B. Wunsch, C. Reichl, W. Wegscheider, M. S. Rudner, E. Demler, and L. M. Vandersypen, *Nagaoka ferromagnetism observed in a quantum dot plaquette,* Nature **579**, 528 (2020).

[10] M. Veldhorst, J. Hwang, C. Yang, A. Leenstra, B. de Ronde, J. Dehollain, J. Muhonen, F. Hudson, K. M. Itoh, A. Morello, *et al.*, *An addressable quantum dot qubit with fault-tolerant control-fidelity,* Nature Nanotechnology **9**, 981 (2014).

[11] D. Zajac, T. Hazard, X. Mi, E. Nielsen, and J. R. Petta, *Scalable gate architecture for a one-dimensional array of semiconductor spin qubits,* Physical Review Applied **6**, 054013 (2016).

[12] D. Sabbagh, N. Thomas, J. Torres, R. Pillarisetty, P. Amin, H. George, K. Singh, A. Budrevich, M. Robinson, D. Merrill, *et al.*, *Quantum transport properties of industrial si 28/si o 2 28,* Physical Review Applied **12**, 014013 (2019).

[13] W. Lawrie, H. Eenink, N. Hendrickx, J. Boter, L. Petit, S. Amitonov, M. Lodari, B. Paquelet Wuetz, C. Volk, S. Philips, *et al.*, *Quantum dot arrays in silicon and germanium,* Applied Physics Letters **116**, 080501 (2020).

[14] L. Petit, J. Boter, H. Eenink, G. Droulers, M. Tagliaferri, R. Li, D. Franke, K. Singh, J. Clarke, R. Schouten, *et al.*, *Spin lifetime and charge noise in hot silicon quantum dot qubits,* Physical Review Letters **121**, 076801 (2018).

[15] H. Eenink, L. Petit, W. Lawrie, J. Clarke, L. Vandersypen, and M. Veldhorst, *Tunable coupling and isolation of single electrons in silicon metal-oxide-semiconductor quantum dots,* Nano letters **19**, 8653 (2019).

[16] L. Petit, H. Eenink, M. Russ, W. Lawrie, N. Hendrickx, S. Philips, J. Clarke, L. Vandersypen, and M. Veldhorst, *Universal quantum logic in hot silicon qubits,* Nature **580**, 355 (2020).

[17] N. Hendrickx, D. Franke, A. Sammak, M. Kouwenhoven, D. Sabbagh, L. Yeoh, R. Li, M. Tagliaferri, M. Virgilio, G. Capellini, *et al.*, *Gate-controlled quantum dots and superconductivity in planar germanium,* Nature communications **9**, 2835 (2018).

[18] N. Hendrickx, D. Franke, A. Sammak, G. Scappucci, and M. Veldhorst, *Fast two-qubit logic with holes in germanium,* Nature **577**, 487 (2020).

[19] G. Scappucci, C. Kloeffel, F. A. Zwanenburg, D. Loss, M. Myronov, J.-J. Zhang, S. De Franceschi, G. Katsaros, and M. Veldhorst, *The germanium quantum information route,* arXiv preprint arXiv:2004.08133 (2020).

[20] C. H. Yang, W. H. Lim, N. S. Lai, A. Rossi, A. Morello, and A. S. Dzurak, *Orbital and valley state spectra of a few-electron silicon quantum dot,* Physical Review B **86**, 115319 (2012).

[21] P. Harvey-Collard, B. D'Anjou, M. Rudolph, N. T. Jacobson, J. Dominguez, G. A. Ten Eyck, J. R. Wendt, T. Pluym, M. P. Lilly, W. A. Coish, *et al.*, *High-fidelity single-shot readout for a spin qubit via an enhanced latching mechanism,* Physical Review X **8**, 021046 (2018).

[22] J. Elzerman, R. Hanson, J. Greidanus, L. W. Van Beveren, S. De Franceschi, L. Vandersypen, S. Tarucha, and L. Kouwenhoven, *Few-electron quantum dot circuit with integrated charge read out,* Physical Review B **67**, 161308 (2003).

[23] L. A. Tracy, D. R. Luhman, S. M. Carr, N. C. Bishop, G. A. Ten Eyck, T. Pluym, J. R. Wendt, M. P. Lilly, and M. S. Carroll, *Single shot spin readout using a cryogenic high-electron-mobility transistor amplifier at sub-kelvin temperatures,* Applied Physics Letters **108**, 063101 (2016).

[24] R. Schoelkopf, P. Wahlgren, A. Kozhevnikov, P. Delsing, and D. Prober, *The radio-frequency single-electron transistor (rf-set): A fast and ultrasensitive electrometer,* Science **280**, 1238 (1998).

[25] S. Angus, A. Ferguson, A. Dzurak, and R. Clark, *A silicon radio-frequency single electron transistor,* Applied Physics Letters **92**, 112103 (2008).

[26] K. Petersson, C. Smith, D. Anderson, P. Atkinson, G. Jones, and D. Ritchie, *Charge and spin state readout of a double quantum dot coupled to a resonator,* Nano letters **10**, 2789 (2010).

[27] J. Colless, A. Mahoney, J. Hornibrook, A. Doherty, H. Lu, A. Gossard, and D. Reilly, *Dispersive readout of a few-electron double quantum dot with fast rf gate sensors,* Physical Review Letters **110**, 046805 (2013).

[28] A. West, B. Hensen, A. Jouan, T. Tanttu, C.-H. Yang, A. Rossi, M. F. Gonzalez-Zalba, F. Hudson, A. Morello, D. J. Reilly, *et al.*, *Gate-based single-shot readout of spins in silicon,* Nature Nanotechnology **14**, 437 (2019).

[29] J. Dehollain, J. Pla, E. Siew, K. Tan, A. Dzurak, and A. Morello, *Nanoscale broadband transmission lines for spin qubit control,* Nanotechnology **24**, 015202 (2012).

[30] C. Yang, K. Chan, R. Harper, W. Huang, T. Evans, J. Hwang, B. Hensen, A. Laucht, T. Tanttu, F. Hudson, *et al.*, *Silicon qubit fidelities approaching incoherent noise limits via pulse engineering,* Nature Electronics **2**, 151 (2019).

[31] J. Yoneda, K. Takeda, T. Otsuka, T. Nakajima, M. R. Delbecq, G. Allison, T. Honda, T. Kodera, S. Oda, Y. Hoshi, *et al.*, *A quantum-dot spin qubit with coherence limited by charge noise and fidelity higher than 99.9%,* Nature Nanotechnology **13**, 102 (2018).

[32] R. Leon, C. H. Yang, J. Hwang, J. C. Lemyre, T. Tanttu, W. Huang, K. W. Chan, K. Tan, F. Hudson, K. Itoh, *et al.*, *Coherent spin control of s-, p-, d-and f-electrons in a silicon quantum dot,* Nature communications **11**, 1 (2020).

[33] C. H. Yang, R. Leon, J. Hwang, A. Saraiva, T. Tanttu, W. Huang, J. C. Lemyre, K. W. Chan, K. Tan, F. E. Hudson, *et al.*, *Operation of a silicon quantum processor unit cell above one kelvin,* Nature **580**, 350 (2020).

[34] R. Maurand, X. Jehl, D. Kotekar-Patil, A. Corna, H. Bohuslavskyi, R. Laviéville, L. Hutin, S. Barraud, M. Vinet, M. Sanquer, *et al.*, *A cmos silicon spin qubit,* Nature communications **7**, 13575 (2016).

[35] A. Corna, L. Bourdet, R. Maurand, A. Crippa, D. Kotekar-Patil, H. Bohuslavskyi, R. Laviéville, L. Hutin, S. Barraud, X. Jehl, *et al.*, *Electrically driven electron spin resonance mediated by spin–valley–orbit coupling in a silicon quantum dot,* npj Quantum Information **4**, 6 (2018).

[36] R. Zhao, T. Tanttu, K. Y. Tan, B. Hensen, K. W. Chan, J. Hwang, R. Leon, C. H. Yang, W. Gilbert, F. Hudson, *et al.*, *Single-spin qubits in isotopically enriched silicon at low magnetic field,* Nature Communications **10**, 1 (2019).

[37] R. Ruskov, M. Veldhorst, A. S. Dzurak, and C. Tahan, *Electron g-factor of valley states in realistic silicon quantum dots,* Physical Review B **98**, 245424 (2018).

[38] G. Burkard, D. Loss, and D. P. DiVincenzo, *Coupled quantum dots as quantum gates,* Physical Review B **59**, 2070 (1999).

[39] T. Meunier, V. Calado, and L. Vandersypen, *Efficient controlled-phase gate for single-spin qubits in quantum dots,* Physical Review B **83**, 121403 (2011).

[40] M. Reed, B. Maune, R. Andrews, M. Borselli, K. Eng, M. Jura, A. Kiselev, T. Ladd, S. Merkel, I. Milosavljevic, *et al.*, *Reduced sensitivity to charge noise in semiconductor spin qubits via symmetric operation,* Physical Review Letters **116**, 110402 (2016).

[41] F. Martins, F. K. Malinowski, P. D. Nissen, E. Barnes, S. Fallahi, G. C. Gardner, M. J. Manfra, C. M. Marcus, and F. Kuemmeth, *Noise suppression using symmetric exchange gates in spin qubits,* Physical Review Letters **116**, 116801 (2016).

[42] A. Sigillito, M. Gullans, L. Edge, M. Borselli, and J. Petta, *Coherent transfer of quantum information in a silicon double quantum dot using resonant swap gates,* npj Quantum Information **5**, 1 (2019).

[43] X. Xue, T. Watson, J. Helsen, D. R. Ward, D. E. Savage, M. G. Lagally, S. N. Coppersmith, M. Eriksson, S. Wehner, and L. Vandersypen, *Benchmarking gate fidelities in a si/sige two-qubit device,* Physical Review X **9**, 021011 (2019).

[44] G. Burkard, D. Loss, D. P. DiVincenzo, and J. A. Smolin, *Physical optimization of quantum error correction circuits,* Physical Review B **60**, 11404 (1999).

[45] M. Russ, D. M. Zajac, A. J. Sigillito, F. Borjans, J. M. Taylor, J. R. Petta, and G. Burkard, *High-fidelity quantum gates in si/sige double quantum dots,* Physical Review B **97**, 085421 (2018).

[46] W. Huang, C. Yang, K. Chan, T. Tanttu, B. Hensen, R. Leon, M. Fogarty, J. Hwang, F. Hudson, K. M. Itoh, *et al., Fidelity benchmarks for two-qubit gates in silicon,* Nature **569**, 532 (2019).

[47] D. P. Franke, J. S. Clarke, L. M. Vandersypen, and M. Veldhorst, *Rent's rule and extensibility in quantum computing,* Microprocessors and Microsystems **67**, 1 (2019).

[48] M. Veldhorst, H. G. J. Eenink, C. H. Yang, and A. S. Dzurak, *Silicon CMOS architecture for a spin-based quantum computer,* Nature Communication **8**, 1766 (2017).

[49] L. M. K. Vandersypen, H. Bluhm, J. S. Clarke, A. S. Dzurak, R. Ishihara, A. Morello, D. J. Reilly, L. R. Schreiber, and M. Veldhorst, *Interfacing spin qubits in quantum dots and donors—hot, dense, and coherent,* npj Quantum Information **3**, 34 (2017).

[50] R. Li, L. Petit, D. P. Franke, J. P. Dehollain, J. Helsen, M. Steudtner, N. K. Thomas, Z. R. Yoscovits, K. J. Singh, S. Wehner, *et al., A crossbar network for silicon quantum dot qubits,* Science Advances **4**, eaar3960 (2018).

[51] R. Kalra, A. Laucht, J. P. Dehollain, D. Bar, S. Freer, S. Simmons, J. T. Muhonen, and A. Morello, *Vibration-induced electrical noise in a cryogen-free dilution refrigerator: Characterization, mitigation, and impact on qubit coherence,* Review of Scientific Instruments **87**, 073905 (2016).

3

TUNABLE COUPLING AND ISOLATION OF SINGLE ELECTRONS IN A SI-MOS DEVICE

Long coherence times, excellent single-qubit gate fidelities and two-qubit logic have been demonstrated with silicon metal-oxide-semiconductor spin qubits, making it one of the leading platforms for quantum information processing. However, a long-standing challenge in this system has been the demonstration of tunable couplings. In this chapter, we overcome this hurdle and demonstrate a double quantum dot that can be tuned and controlled to a high degree of freedom at a temperature of 0.5 K. We start with the characterization of a double quantum dot, highlighting its uniformity and stability. We focus on the (1,1)-(0,2) charge anticrossing and demonstrate tunable couplings up to 13 GHz, obtained by fitting the charge polarization lines, and tunable tunnel rates down to below 1 Hz, deduced from the random telegraph signal. Additionally, the electrons can be completely isolated from the reservoir, giving prospects for the operation of large systems where only a few quantum dots can be coupled to near two-dimensional electron gases. We also study the response of the charge sensor, which we find, despite the high temperature, to be very sensitive to the (1,1)-(0,2) charge transition paving the way for high-fidelity spin readout based on Pauli spin blockade.

Parts of this chapter have been published in **Nano letters 19**, 8653-8657 (2019) [1].

3.1. CONTROLLING THE COUPLING BETWEEN TWO ELECTRON SPINS

Quantum computation with quantum dots has been proposed using qubits defined on the spin states of one [2], two [3] or more [4, 5] electrons. In all these proposals, a crucial element required to realize a universal quantum gate set is the exchange interaction between electrons. The exchange interaction is set by the tunnel coupling and the detuning, and gaining precise control over these parameters enables to define and operate qubits at their optimal points [6–9]. Excellent control has already been reported in GaAs [6, 7, 10], strained silicon [11, 12] and more recently in strained germanium [13, 14]. Reaching this level of control in silicon metal-oxide-semiconductor (Si-MOS) quantum dots is highly desired as this platform has a high potential for complete integration with classical manufacturing technology [15–17]. This becomes apparent from many proposals of architectures for large-scale quantum computation [2, 18–23] that make use of full control over the exchange interaction. However, current two-qubit logic with single spins in Si-MOS is based on controlling the exchange using the detuning only [24] or is executed at fixed exchange interaction [25]. Ideally, the exchange should be turned on only for two-qubit logic and single-qubit gates should be realized when all the couplings have been switched off in order to maximize qubit coherence. Moreover, tunnel coupling control is also beneficial in other scenarios. For example, when spin readout is accomplished via Pauli spin blockade, the tunnel coupling must be set to an intermediate value to maximize spin-to-charge conversion fidelity. When qubits need to be shuttled as a mean for long-range coupling tunnel couplings must be also turned on and off for a fast and high-fidelity spin transfer.

The main challenge for Si-MOS devices is that electrons live in close proximity of the Si-SiO_2 interface. Compared to the epitaxial interface of Si-SiGe heterostructures, this is usually characterized by a higher level of disorder and can limit the tunability of devices. However, in this context much can be gained by moving from academic to industrial cleanrooms where these interfaces are expected to show a superior quality.

A first step toward the required control has been the demonstration of tunable coupling in a double quantum dot system operated in the many-electron regime, where gaining control is more accessible owing to the larger electron wave function [26, 27]. More recently, exchange-controlled two-qubit operations have been shown with three-electron quantum dots [28]. However, tunnel couplings between single electrons that can be switched off and turned on for qubit operation still remain to be shown in Si-MOS.

3.2. CHARACTERIZATION OF THE DOUBLE QUANTUM DOT

Figure 3.1a shows a scanning electron micrograph (SEM) of a Si-MOS device nominally identical to the one measured and a schematic cross-section of the quantum dot region along the dashed line in the SEM image. A high quality wafer is realized [15] with a 100 nm ^{28}Si epilayer with an 800 ppm residual ^{29}Si concentration [29], covered by 10 nm of thermally grown SiO_2. Ohmic contacts are made by defining highly doped n^{++} regions by phosphorus-ion implantation. We use an overlapping gate integration scheme [11, 30, 31] and use palladium (Pd) gates, which have the beneficial property of small

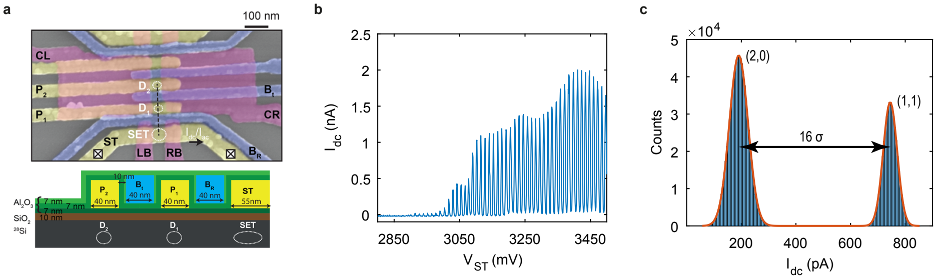

Figure 3.1: **a** False-color scanning electron micrograph (SEM) of a device identical to the one measured. Purple, yellow, and blue correspond to the first, second, and third metal layers, respectively. Crossed boxes indicate the ohmic source and drain contacts used to measure I_{dc} and I_{ac}, and circles indicate the intended location of the quantum dots D1 and D2 and the single-electron transistor (SET).The quantum dots are defined using gate electrodes P1 and P2, confined laterally using CL and CR. B_t controls the tunnel coupling between the quantum dots, and B_R controls the tunnel coupling to the SET. **b** Transport source-drain current I_{dc} versus top-gate voltage V_{ST} of the SET defined using the gate electrodes ST, LB and RB. The regular spacing of Coulomb peaks indicates a well defined quantum dot, ideal for charge sensing. **c** Histogram of the charge sensor current in response to (2,0)-(1,1) tunneling events. The counts are extracted from 4655 single-shot traces with integration time τ = 82µs, measurement bandwidth 50 kHz, and bin size b = 5 pA. The peaks are fitted with a double Gaussian with $\sigma_{(2,0)}$ = 34.1 pA and $\sigma_{(1,1)}$ = 25.5 pA, giving a peak spacing of $> 16\sigma_{(2,0)}$.

grain size [32]. The gates are electrically isolated by an Al_2O_3 layer grown by atomic layer deposition. The sample is annealed at 400 °C in a hydrogen atmosphere to repair e-beam induced damage to the silicon oxide and to reduce the charge trap density [33, 34].

Figure 3.1b shows the current through the SET, electrostatically defined using the gates ST, LB and RB, and it is used both as charge sensor and as an electron reservoir. The highly regular coulomb peak spacing indicates a well defined quantum dot, which has a constant charging energy of approximately 0.9 meV. We extract a gate capacitance of 13 aF, in agreement with a simple parallel plate capacitor model. We form a double quantum dot between the confinement barriers CL and CR, using the gates P_1 and P_2 to tune the quantum dot potentials. B_t and B_R are used to control the tunnel coupling between the quantum dots and from the quantum dots to the SET, respectively. We note here that the size of the quantum dot defined under the gate ST is by design larger than the ones below the plunger gates P_1 and P_2. This allows to increase the capacitance coupling of the SET to its surroundings, improving the charge sensitivity. On the other hand, a smaller size can be beneficial for the quantum dots used as qubits, since it decouples them from the environment, potentially increasing the spin lifetime and the coherence.

We characterize the charge readout sensitivity by recording the random telegraph signal (RTS) originating from the tunneling of the electrons between the (2,0) and (1,1) charge states with inter-dot tunnel rate $\Gamma_c \approx 48$ Hz. The (2,0)-(1,1) charge transition is particularly relevant when spin readout is performed using PSB, and it is therefore of particular interest for ‘hot’ qubit operation. In this case the response of the SET is lower than in the case of a pure charge transition and a latched readout protocol is often used to improve the sensitivity [35]. In the device in Fig. 3.1a the SET is positioned with respect to the double quantum dot in such a way that its sensitivity to inter-dot transitions is maximized and very similar to the one of normal charge additions. Figure 3.1c shows

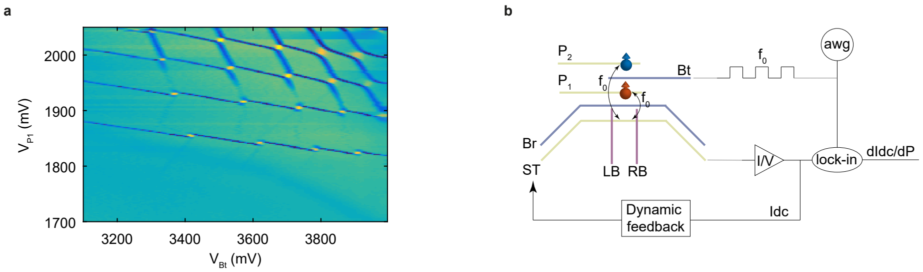

Figure 3.2: **a** Charge stability diagram as a function of V_{P1} and $V_{\mathrm{B_t}}$, confirming that both quantum dots can be fully depleted. At higher fillings the tunnel coupling between the two dots increases due to the larger wavefunction. **b** Schematic of the charge stability diagram detection technique. The electrons in the two quantum dots tunnel in and out of the reservoir at a frequency f_0, corresponding to the square wave excitation applied to the gate B_t. The component of the current of the SET oscillating at f_0 gives the transconductance response. Finally, a dynamic feedback keeps the current of the SET at the most sensitive point by correcting the voltage applied to ST. This compensates for the finite cross capacitances between gates as well as charge jumps in the device.

a histogram of the measured readout signal, using an integration time $\tau = 82\,\mu\mathrm{s}$. We fit the counts with a double Gaussian curve with $\mu_{(2,0),(1,1)}$ and $\sigma_{(2,0),(1,1)}$ the mean and standard deviation of the Gaussian distributions corresponding to the two charge states. We find $\Delta\mu_{(2,0)-(1,1)} > 16\sigma_{(2,0)}$ corresponding to an excellent discrimination between the (2,0) and (1,1) charge states.

To precisely measure charge transitions, we implement charge sensing using a lock-in amplifier and apply a square wave excitation at $f_{\mathrm{ac}} = 77\,\mathrm{Hz}$ on the gate $\mathrm{B_t}$. When the gate voltages are swept over a charge transition, the electron jumps back and forth from the quantum at a frequency f_{ac}, provided that the tunneling rate is sufficiently high. By monitoring the current of the SET with a lock-in amplifier is then possible to detect any charge event. This method is used in combination with an active feedback loop that keeps the current of the SET constant during the measurement. A detailed discussion of this charge detection technique can be found in ref. [36].

The double dot charge stability diagram is shown in Fig. 3.2a. Regular transitions are observed for both quantum dots, without significant charge jumps over the few hours needed for the measurement. Horizontal and vertical blue lines indicate the loading of an additional electron from the SET to quantum dots $\mathrm{D_1}$ (located under the gate $\mathrm{P_1}$) and $\mathrm{D_2}$ (located under $\mathrm{P_2}$) respectively, while diagonal yellow lines indicate electron transitions between the two quantum dots. We do not observe more charge transitions at voltages lower than the measured range and we conclude that the double quantum dot is in the single electron regime. When $\mathrm{P_1}$ is decreased the tunneling rate of the quantum dot further from the reservoir drops below 77 Hz and the charge transitions lines disappear. The tunnel coupling between the two quantum dots can be controlled with the gate Bt. Figure 3.3a and b show the double quantum dot charge stability diagrams as a function of $V_{\mathrm{P_2}}$ and $V_{\mathrm{P_1}}$ for weak ($V_{\mathrm{Bt}} = 2.9\,\mathrm{V}$) and strong ($V_{\mathrm{Bt}} = 3.6\,\mathrm{V}$) coupling. In order to highlight the difference between weak and strong coupling, Fig. 3.3c and d show higher resolution maps of the (2,0)-(1,1) anticrossing.

When we set a weak inter-dot coupling, charge addition lines of $\mathrm{D_2}$ are barely visible

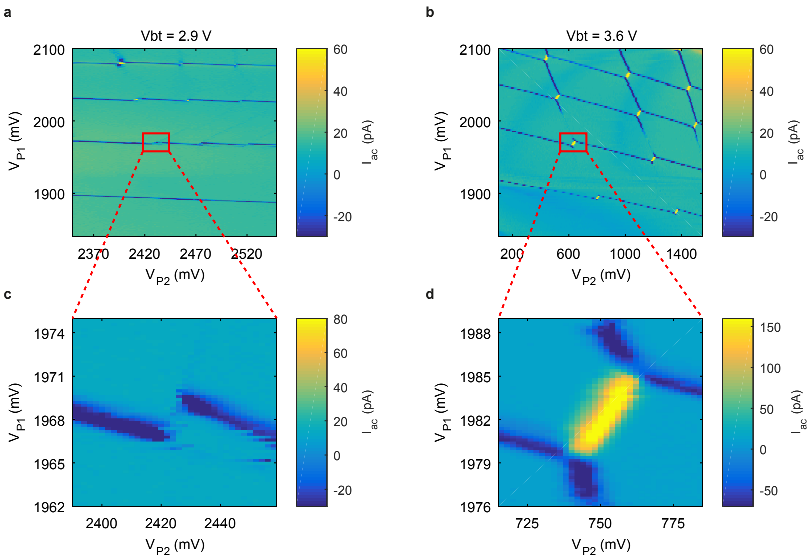

Figure 3.3: **a,b** Charge stability diagrams of the charge sensor response I_{ac} as a function of voltages V_{P2} and V_{P1} of the double quantum dot for weak (V_{B_t} = 2.9 V in **a**) and strong (V_{B_t} = 3.6 V in **b**) coupling. Electrons are loaded from the SET. Transitions with a tunnel rate $\Gamma < f_{ac}$ are not visible. **c,d** High-resolution zoom-in of the (2,0)-(1,1) anticrossing for both **c** weak and **d** strong tunnel coupling.

in the charge stability diagram, because of the low tunnel rate between D_2 and the reservoir. Similarly, at the (2,0)-(1,1) inter-dot transition, no transitions between the quantum dots can be observed because of the low inter-dot coupling t_c. The loading of the first electron in D_2 can only be observed from the shift of the D_1 charge addition line, caused by the mutual capacitance E_m of the two quantum dots. Only in the multi-electron regime where the quantum dot wave functions are larger and have more overlap, the coupling is sufficiently high to observe charge transition lines. When the inter-dot coupling is strong, charge addition lines belonging to D_2 are visible near the anticrossings and at high V_{P_1}, where Γ_{R2} is increased. Additionally, t_c and E_m are increased and we observe a honeycomb shaped charge stability diagram, with clearly visible inter-dot transition lines, even when only a single electron is loaded on each quantum dot.

We estimate the relative location and size of the quantum dots from the gate voltage differences $\Delta V_{P_{1(2)}}$ needed to load the second electron with respect to the first electron. We additionally use the cross-capacitances $\alpha_{r1(2)}$ of the plunger gates, determined by measuring the shift in $\Delta V_{P_{1(2)}}$ of the charge transition line of the first electron in $D_{1(2)}$ as a function of a step in $\Delta V_{P_{2(1)}}$, where $\alpha_{r1(2)}$ is the ratio between the shift and the step.

When the coupling is weak, we find $\Delta V_{P_1} \approx 70\,\text{mV}$, $\alpha_{r1} < 0.05$ for D_1 and $\Delta V_{P_2} \approx 50\,\text{mV}$, $\alpha_{r2} \approx 0.33$ for D_2. We conclude that we have a system of two weakly coupled quantum dots located under P_1 and P_2. For D_1, both ΔV_{P_1} and α_{r1} are almost independent of the coupling. For D_2, ΔV_{P_2} increases by a factor 11, from $\Delta V_{P_2} \approx 50\,\text{mV}$ for weak coupling to $\Delta V_{P_2} \approx 550\,\text{mV}$ for strong coupling, while α_{r2} increases by a factor 5, from 0.3 to 1.5. The increase in α_{r2} can be explained by a change in the location of D_2 from

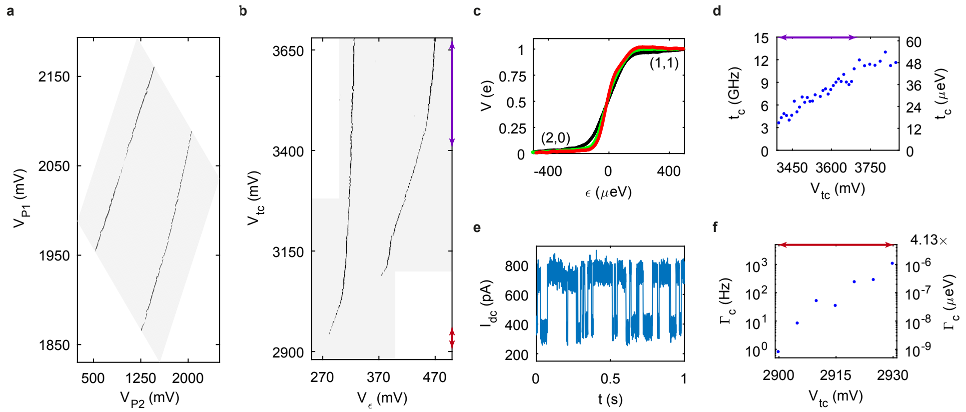

Figure 3.4: **a** Map of the isolated (2,0)-(1,1) and (1,1)-(0,2) anticrossings as a function of V_{P2} and V_{P1}. No additional electrons are loaded into the quantum dot islands due to a negligible Γ_R. **b** Map of the (2,0)-(1,1) and (1,1)-(0,2) anticrossings as a function of detuning and barrier voltage. The relative lever arm between V_{t_c} and V_ϵ changes at lower barrier voltages due to a change in quantum dot location. The orange and purple arrows indicate the ranges in which the tunnel coupling was determined using RTS and polarization line measurements, respectively. **c** Polarization lines (excess charge as a function of detuning) across the anticrossing for high t_c (black, V_{t_c}= 3.85 V), intermediate t_c (green, V_{t_c} = 3.6 V), and relatively low t_c (red, V_{t_c} = 3.4 V). **d** Extracted t_c from polarization lines as a function of V_{t_c}, where we find tunable t_c up to 13 GHz. **e** RTS for weak coupling V_{t_c} = 2.910 V. **f** Extracted Γ_c from RTS measurements as a function of V_{t_c}, demonstrating tunable tunnel rates down to <1 Hz.

the gate P_2, to a position partly below the gate B_t. This change of quantum dot location will decrease the lever arm and this is likely the cause of the increase in ΔV_{P2}. We conclude that tuning from weak to strong coupling causes the location of D_2 to shift from a position mostly under P_2 to a position partly below B_t, while D_1 is stationary under P_1. The ease with which D_2 can be displaced additionally suggests that no unintentional quantum dots are formed between barrier gates.

3.3. ISOLATED ELECTRONS AND TUNNEL COUPLING MEASUREMENTS

By reducing V_{BR}, the tunnel rate Γ_R between the the SET reservoir and the quantum dots can be reduced and the loading and unloading of electrons can be prevented, resulting in an isolated quantum dot system [28, 37]. Because the reservoir is connected to room temperature electronics, decoupling the quantum dot from it may provide the advantage of reduced noise [38]. Figure 3.4a shows the (2,0)-(1,1) and (1,1)-(0,2) anticrossings as a function of V_{P_2} and V_{P_1} when the coupling is strong. Only inter-dot transition lines are present over a wide range of voltages, where one would normally expect multiple charge transition lines. This implies that no additional electrons are loaded, as a result of a negligible coupling to the reservoir. The ability to control the inter-dot transitions of a double quantum dot without loading additional electrons provides good prospects for the operation of quantum dot arrays that are only remotely coupled to reservoirs, as proposed in quantum information architectures [18, 20, 21].

In this isolated regime we control the tunnel coupling t_c with the gate Bt from ≈ 0 up to $\approx 10\,\mathrm{GHz}$. As discussed in the previous section the gate Bt is significantly coupled to one of the two dots. Therefore, we define a new set of virtual gates [10, 39, 40] in order to have an independent control over the tunnel coupling and to compensate for the influence of V_Bt on the detuning between the two quantum dots. Consequently we convert V_{P_2}, V_{P_1} and V_Bt to detuning V_ϵ, on site potential V_U and tunnel coupling voltage V_{t_c}. Figure 3.4b shows the (2,0)-(1,1) and (1,1)-(0,2) anticrossings as a function of the new set of virtual gates V_ϵ and V_{t_c}. For both transitions the inter-dot line vanishes at low V_{t_c}, meaning that the coupling has been largely switched off. We observe that for the (1,1)-(0,2) anticrossing, the transition line disappears at $V_{t_\mathrm{c}} < 3.1\,\mathrm{V}$, while for the (2,0)-(1,1) anticrossing this happens for $V_{t_\mathrm{c}} < 2.95\,\mathrm{V}$. The variation may come from a small asymmetry in the system.

We tune the double quantum dot to a significantly coupled regime and quantitatively analyze the system by taking charge polarization lines. Figure 3.4c shows charge polarization lines at high, intermediate and relatively low tunnel couplings within this regime. We measure the charge sensor response Q as a function of detuning ϵ and fit the data according to a two level model that includes cross-talk of ϵ to the charge sensor and the influence of the quantum dot charge state on the charge sensor sensitivity [10, 41]. From the thermal broadening of the polarization line at low tunnel coupling, we extract the lever arm of the virtual gate V_ϵ, $\alpha_\epsilon \approx 0.04\,\mathrm{eV/mV}$, by assuming the electron temperature to be equal to the fridge temperature of 0.44 K.

For relatively low tunnel couplings, we observe in the charge polarization lines deviations from the model for a two-level system [41] (see the red curve in Fig. 3.4c with $\epsilon > 0$). This deviation can also not be explained by a modified model that includes valley states, considering an adiabatic detuning sweep and assuming zero temperature [42]. While these measurements were done adiabatically, the elevated temperature of 0.44 K can cause a non-negligible population of valley or other excited states. These excited states can cause a charge transition at a different detuning energy, thereby giving rise to a deviation. A large tunnel coupling can increase the relaxation rate of these excited states and thus decrease their population. As a consequence, the charge polarization lines are in agreement with the model for a two-level system [41] at larger tunnel couplings.

At tunnel couplings below 3 GHz, the thermal broadening of the polarization line prevents accurate fitting. Instead of the tunnel coupling energy t_c we determine the inter-dot tunnel rate Γ_c, which is proportional to the square of the tunnel coupling [43–45]. We measure the RTS (Fig. 3e) at the (2,0)-(1,1) transition and fit the counts C of a histogram of the tunnel times T to $C = Ae^{-\Gamma_c T}$, where A is a normalisation constant. In the measurements we have tuned V_ϵ such that $\Gamma_{c(2,0)-(1,1)} \approx \Gamma_{c(1,1)-(2,0)}$.

Figure 3.4d shows t_c as a function of V_{t_c}, demonstrating tunable tunnel coupling in the strong coupling regime and Fig. 3.4f shows the obtained Γ_c as a function of V_{t_c} from 1 kHz down to below 1 Hz. We note that we can further reduce the tunnel rate to even smaller rates simply by further reducing V_tc.

A change in barrier height or width results in an exponential change in t_c and in Γ_c. When the tunnel coupling is low, D_2 is located mainly under P_2, and a change in V_{t_c} has a significant impact on the barrier. Correspondingly, we observe an exponential dependence of Γ_c versus V_{t_c}. When the tunnel coupling is high, D_2 is located mostly under

$\mathrm{B_t}$ and the impact of V_{t_c} on the barrier is vanishing. As a result we observe a seemingly linear dependence of t_c versus V_{t_c} from 3 up to 11 GHz that saturates around 13 GHz for $V_{t_c} > 3675$ mV.

REFERENCES

[1] H. Eenink, L. Petit, W. Lawrie, J. Clarke, L. Vandersypen, and M. Veldhorst, *Tunable coupling and isolation of single electrons in silicon metal-oxide-semiconductor quantum dots,* Nano letters **19**, 8653 (2019).

[2] D. Loss and D. P. DiVincenzo, *Quantum computation with quantum dots,* Physical Review A **57**, 120 (1998).

[3] J. Levy, *Universal quantum computation with spin-1/2 pairs and heisenberg exchange,* Physical Review Letters **89**, 147902 (2002).

[4] D. P. DiVincenzo, D. Bacon, J. Kempe, G. Burkard, and K. B. Whaley, *Universal quantum computation with the exchange interaction,* Nature **408**, 339 (2000).

[5] Z. Shi, C. Simmons, J. Prance, J. K. Gamble, T. S. Koh, Y.-P. Shim, X. Hu, D. Savage, M. Lagally, M. Eriksson, *et al.*, *Fast hybrid silicon double-quantum-dot qubit,* Physical Review Letters **108**, 140503 (2012).

[6] F. Martins, F. K. Malinowski, P. D. Nissen, E. Barnes, S. Fallahi, G. C. Gardner, M. J. Manfra, C. M. Marcus, and F. Kuemmeth, *Noise Suppression Using Symmetric Exchange Gates in Spin Qubits,* Physical Review Letters **116**, 116801 (2016).

[7] M. Reed, B. Maune, R. Andrews, M. Borselli, K. Eng, M. Jura, A. Kiselev, T. Ladd, S. Merkel, I. Milosavljevic, *et al.*, *Reduced sensitivity to charge noise in semiconductor spin qubits via symmetric operation,* Physical Review Letters **116**, 110402 (2016).

[8] J. M. Taylor, V. Srinivasa, and J. Medford, *Electrically protected resonant exchange qubits in triple quantum dots,* Physical Review Letters **111**, 050502 (2013).

[9] D. Kim, Z. Shi, C. Simmons, D. Ward, J. Prance, T. S. Koh, J. K. Gamble, D. Savage, M. Lagally, M. Friesen, *et al.*, *Quantum control and process tomography of a semiconductor quantum dot hybrid qubit,* Nature **511**, 70 (2014).

[10] T. Hensgens, T. Fujita, L. Janssen, X. Li, C. J. Van Diepen, C. Reichl, W. Wegscheider, S. Das Sarma, and L. M. K. Vandersypen, *Quantum simulation of a Fermi–Hubbard model using a semiconductor quantum dot array,* Nature **548**, 70 (2017).

[11] M. G. Borselli, K. Eng, R. S. Ross, T. M. Hazard, K. S. Holabird, B. Huang, A. A. Kiselev, P. W. Deelman, L. D. Warren, I. Milosavljevic, *et al.*, *Undoped accumulation-mode si/sige quantum dots,* Nanotechnology **26**, 375202 (2015).

[12] D. M. Zajac, A. J. Sigillito, M. Russ, F. Borjans, J. M. Taylor, G. Burkard, and J. R. Petta, *Resonantly driven CNOT gate for electron spins,* Science **359**, 439 (2018).

[13] N. Hendrickx, D. Franke, A. Sammak, M. Kouwenhoven, D. Sabbagh, L. Yeoh, R. Li, M. Tagliaferri, M. Virgilio, G. Capellini, *et al.*, *Gate-controlled quantum dots and superconductivity in planar germanium,* Nature communications **9**, 2835 (2018).

[14] N. Hendrickx, D. Franke, A. Sammak, G. Scappucci, and M. Veldhorst, *Fast two-qubit logic with holes in germanium,* Nature **577**, 487 (2020).

[15] D. Sabbagh, N. Thomas, J. Torres, R. Pillarisetty, P. Amin, H. George, K. Singh, A. Budrevich, M. Robinson, D. Merrill, *et al.*, *Quantum transport properties of industrial si 28/si o 2 28,* Physical Review Applied **12**, 014013 (2019).

[16] V. Mazzocchi, P. Sennikov, A. Bulanov, M. Churbanov, B. Bertrand, L. Hutin, J. Barnes, M. Drozdov, J. Hartmann, and M. Sanquer, *99.992% 28si cvd-grown epilayer on 300 mm substrates for large scale integration of silicon spin qubits,* Journal of Crystal Growth **509**, 1 (2019).

[17] R. Maurand, X. Jehl, D. Kotekar-Patil, A. Corna, H. Bohuslavskyi, R. Laviéville, L. Hutin, S. Barraud, M. Vinet, M. Sanquer, *et al.*, *A cmos silicon spin qubit,* Nature communications **7**, 13575 (2016).

[18] M. Veldhorst, H. G. J. Eenink, C. H. Yang, and A. S. Dzurak, *Silicon CMOS architecture for a spin-based quantum computer,* Nature Communication **8**, 1766 (2017).

[19] L. M. K. Vandersypen, H. Bluhm, J. S. Clarke, A. S. Dzurak, R. Ishihara, A. Morello, D. J. Reilly, L. R. Schreiber, and M. Veldhorst, *Interfacing spin qubits in quantum dots and donors—hot, dense, and coherent,* npj Quantum Information **3**, 34 (2017).

[20] R. Li, L. Petit, D. P. Franke, J. P. Dehollain, J. Helsen, M. Steudtner, N. K. Thomas, Z. R. Yoscovits, K. J. Singh, S. Wehner, *et al.*, *A crossbar network for silicon quantum dot qubits,* Science Advances **4**, eaar3960 (2018).

[21] J. Taylor, H.-A. Engel, W. Dür, A. Yacoby, C. Marcus, P. Zoller, and M. Lukin, *Fault-tolerant architecture for quantum computation using electrically controlled semiconductor spins,* Nature Physics **1**, 177 (2005).

[22] M. Friesen, A. Biswas, X. Hu, and D. Lidar, *Efficient multiqubit entanglement via a spin bus,* Physical Review Letters **98**, 230503 (2007).

[23] B. Trauzettel, D. V. Bulaev, D. Loss, and G. Burkard, *Spin qubits in graphene quantum dots,* Nature Physics **3**, 192 (2007).

[24] M. Veldhorst, C. H. Yang, J. C. C. Hwang, W. Huang, J. P. Dehollain, J. T. Muhonen, S. Simmons, A. Laucht, F. E. Hudson, K. M. Itoh, A. Morello, and A. S. Dzurak, *A two-qubit logic gate in silicon,* Nature **526**, 410 (2015).

[25] W. Huang, C. Yang, K. Chan, T. Tanttu, B. Hensen, R. Leon, M. Fogarty, J. Hwang, F. Hudson, K. M. Itoh, *et al.*, *Fidelity benchmarks for two-qubit gates in silicon,* Nature **569**, 532 (2019).

[26] L. A. Tracy, E. Nordberg, R. Young, C. Borras Pinilla, H. Stalford, G. A. Ten Eyck, K. Eng, K. D. Childs, J. R. Wendt, R. K. Grubbs, *et al.*, *Double quantum dot with tunable coupling in an enhancement-mode silicon metal-oxide semiconductor device with lateral geometry,* Applied Physics Letters **97**, 192110 (2010).

[27] N. Lai, W. Lim, C. Yang, F. Zwanenburg, W. Coish, F. Qassemi, A. Morello, and A. Dzurak, *Pauli spin blockade in a highly tunable silicon double quantum dot,* Scientific reports **1**, 110 (2011).

[28] C. H. Yang, R. Leon, J. Hwang, A. Saraiva, T. Tanttu, W. Huang, J. C. Lemyre, K. W. Chan, K. Tan, F. E. Hudson, *et al.*, *Operation of a silicon quantum processor unit cell above one kelvin,* Nature **580**, 350 (2020).

[29] M. Veldhorst, J. Hwang, C. Yang, A. Leenstra, B. de Ronde, J. Dehollain, J. Muhonen, F. Hudson, K. M. Itoh, A. Morello, *et al.*, *An addressable quantum dot qubit with fault-tolerant control-fidelity,* Nature Nanotechnology **9**, 981 (2014).

[30] S. J. Angus, A. J. Ferguson, A. S. Dzurak, and R. G. Clark, *Gate-defined quantum dots in intrinsic silicon,* Nano letters **7**, 2051 (2007).

[31] D. Zajac, T. Hazard, X. Mi, E. Nielsen, and J. R. Petta, *Scalable gate architecture for a one-dimensional array of semiconductor spin qubits,* Physical Review Applied **6**, 054013 (2016).

[32] M. Brauns, S. V. Amitonov, P.-C. Spruijtenburg, and F. A. Zwanenburg, *Palladium gates for reproducible quantum dots in silicon,* Scientific reports **8**, 1 (2018).

[33] J.-S. Kim, A. M. Tyryshkin, and S. A. Lyon, *Annealing shallow si/sio2 interface traps in electron-beam irradiated high-mobility metal-oxide-silicon transistors,* Applied Physics Letters **110**, 123505 (2017).

[34] E. Nordberg, G. Ten Eyck, H. Stalford, R. Muller, R. Young, K. Eng, L. Tracy, K. Childs, J. Wendt, R. Grubbs, *et al.*, *Enhancement-mode double-top-gated metal-oxide-semiconductor nanostructures with tunable lateral geometry,* Physical Review B **80**, 115331 (2009).

[35] P. Harvey-Collard, B. D'Anjou, M. Rudolph, N. T. Jacobson, J. Dominguez, G. A. Ten Eyck, J. R. Wendt, T. Pluym, M. P. Lilly, W. A. Coish, *et al.*, *High-fidelity single-shot readout for a spin qubit via an enhanced latching mechanism,* Physical Review X **8**, 021046 (2018).

[36] C. H. Yang, W. H. Lim, F. A. Zwanenburg, and A. S. Dzurak, *Dynamically controlled charge sensing of a few-electron silicon quantum dot,* AIP Advances **1**, 042111 (2011).

[37] B. Bertrand, H. Flentje, S. Takada, M. Yamamoto, S. Tarucha, A. Ludwig, A. D. Wieck, C. Bäuerle, and T. Meunier, *Quantum manipulation of two-electron spin states in isolated double quantum dots,* Physical Review Letters **115**, 096801 (2015).

[38] A. Rossi, T. Ferrus, and D. Williams, *Electron temperature in electrically isolated si double quantum dots,* Applied Physics Letters **100**, 133503 (2012).

[39] T. A. Baart, M. Shafiei, T. Fujita, C. Reichl, W. Wegscheider, and L. M. K. Vandersypen, *Single-spin ccd,* Nature Nanotechnology **11**, 330 (2016).

[40] A. Mills, D. Zajac, M. Gullans, F. Schupp, T. Hazard, and J. R. Petta, *Shuttling a single charge across a one-dimensional array of silicon quantum dots,* Nature communications **10**, 1 (2019).

[41] L. DiCarlo, H. Lynch, A. Johnson, L. Childress, K. Crockett, C. Marcus, M. Hanson, and A. Gossard, *Differential charge sensing and charge delocalization in a tunable double quantum dot,* Physical Review Letters **92**, 226801 (2004).

[42] X. Zhao and X. Hu, *Coherent electron transport in silicon quantum dots,* arXiv preprint arXiv:1803.00749 (2018).

[43] F. R. Braakman, P. Barthelemy, C. Reichl, W. Wegscheider, and L. M. Vandersypen, *Long-distance coherent coupling in a quantum dot array,* Nature Nanotechnology **8**, 432 (2013).

[44] J. K. Gamble, M. Friesen, S. Coppersmith, and X. Hu, *Two-electron dephasing in single si and gaas quantum dots,* Physical Review B **86**, 035302 (2012).

[45] A. N. Korotkov, *Continuous quantum measurement of a double dot,* Physical Review B **60**, 5737 (1999).

4

SPIN LIFETIME AND CHARGE NOISE IN HOT SILICON SPIN QUBITS

In this chapter we discuss in detail the temperature dependence of the spin relaxation and the charge noise of a Si-MOS quantum dot. These two parameters show a significant temperature dependence and therefore this study is fundamental to identify a suitable temperature range where spin qubits can still efficiently operate. We start by investigating the magnetic field and temperature dependence of the spin lifetime and we measure T_1 *of 145 ms at base temperature and 2.8 ms at 1.1 K. In order to explain the data we construct a model based on direct and two-phonon transitions including all spin and valley states of the lowest orbital. We find good agreement between the model and the experiments and conclude that while at low temperatures* T_1 *is limited by Johnson noise, likely originating from the two-dimensional electron gas (2DEG) channels present in the device, two-phonon processes determine the relaxation rate above 200 mK. Based on our results we also predict how the spin lifetime can be further improved by decreasing the magnetic field and increasing the valley-splitting energy. Finally, we investigate the charge noise, measured as current fluctuations of the single-electron-transistor used for charge sensing, and measure a rather weak temperature dependence from 100 mK to 4 K.*

Parts of this chapter have been published in **Physical Review Letters 121**, 076801 (2018) [1].

4.1. TWO CRUCIAL PARAMETERS FOR SPIN QUBITS

The spin relaxation and the charge noise are two essential metrics for quantum dot qubits. The spin lifetime T_1 can be of the order of seconds in silicon quantum dots [2–4], exceeding by orders of magnitude the dephasing time T_2^* [5]. This means that in experiments the spin relaxation time does not pose any limitation and qubit performances are entirely limited by the dephasing time. However, temperature can strongly affect T_1. Below 100 mK, T_1 scales roughly linearly with temperature due to single-phonon interactions, but at higher temperatures two-phonon processes can give a much steeper rise as it has been seen for donors [6]. While the low temperature spin relaxation mechanisms are well known and studied, the temperature dependence of T_1 remains an open question and it is not known whether it might become the shortest timescale for quantum operations at elevated temperatures.

Moreover, spin qubits are also sensitive to charge noise, and electrical fluctuations can reduce qubit readout and control fidelities. In particular, electrical noise can affect the resonance frequencies of the qubits via the Stark shift of the electron g-factor and via the exchange interaction. Even when qubits are operated at the charge symmetry point [7, 8] electrical noise can still couple in as tunnel coupling fluctuations. In presence of micromagnets the sensitivity to charge noise is even higher, due to additional magnetic field gradients. All these mechanisms directly affect the qubit performances and reduce the coherence times. Low-frequency charge fluctuations are also equally crucial, since they impact the stability of the device and set the frequency at which qubit parameters, such as the readout point, the resonance frequencies or the exchange interaction need to be retuned. While the physical origin of charge noise is not completely understood, a basic description often involves an ensemble of two-level fluctuators coupled to the spin. These fluctuators are thermally activated and therefore temperature affects the total noise amplitude.

The temperature dependence of spin relaxation and charge noise captures most of the challenges of operating qubits at higher temperatures. Investigating their temperature dependence and understanding their limiting mechanisms is therefore vital in evaluating the prospects for ‘hot’ spin qubits.

4.2. DEVICE CHARACTERIZATION AND LOW TEMPERATURE MEASUREMENTS

Figure 4.1a shows a scanning electron microscope (SEM) image of a quantum dot device, realized in isotopically enriched silicon (^{28}Si), identical in design to the one measured. Figure 4.1b presents the charge stability diagram of the device, showing charge transitions originating from three quantum dots under the gates P1, P2 and B2. Two quantum dots are left empty and we fill the one under P1 with one electron. Charge loading happens via the reservoir R and the tunneling rate is controlled via a combination of B1 and P2, which moves the position of the quantum dot thereby changing the distance to the reservoir. Fig. 4.1c shows how P2 can be used to control the tunneling rate over two orders of magnitude in an exponential way. During the experiments, since the DC signal of the sensing dot is filtered with a 2 kHz low pass filter, the dot-reservoir tunnel rate is set to approximately 700 Hz. From the temperature dependence of the transition width

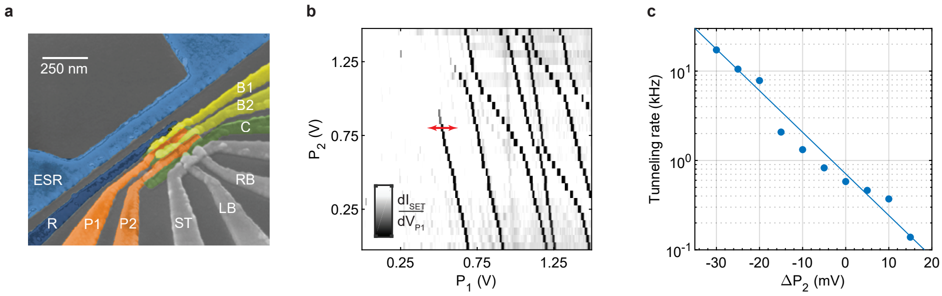

Figure 4.1: **a** Scanning electron microscope image of a device identical to the one measured. R is the reservoir gate, P1, P2, B1 and B2 are the plunger gates, and C confines the electrons in the dots. LB and RB are the left and right barrier of the quantum dot used for sensing, and ST is used both as top gate and reservoir. The ESR line can be used for spin manipulation. **b** Charge stability diagram of the device measured via a double lock-in technique [9]. The transition lines, due to the different slope, can be attributed to three coupled quantum dots. The red arrow shows the (0→1) charge transition relevant for the experiment. **c** Tunneling rate between the dot and the reservoir as a function of V_{P2}, as measured from the random telegraphic signal. $\Delta V_{\mathrm{P2}} = 0$ corresponds to the value set during the experiment. The red line is an exponential fit.

(see Sec. 4.7) we extract a lever arm $\alpha_{\mathrm{P1}} = 0.12$ eV/V.

As shown in Fig. 4.2a, we measure the spin lifetime by applying a three-level voltage pulse to the gate P1, while monitoring the DC current of the sensing dot. First, we inject an electron into the quantum dot, we read out the spin state, and we finally empty the quantum dot [10]. An additional level is added to the pulse after the empty phase in order to cancel out any DC offset. This allows to neglect the slow charging of the capacitors in the bias tee on the PCB. We measure the spin-up fraction as a function of load time and extract T_1 by fitting the data with a single exponential decay.

The measured T_1 as a function of magnetic field (applied in the [010] direction) is plotted in Fig. 4.2c and the temperature dependence for three different magnetic fields is shown in Fig. 4.3a. As discussed in chapter 2, the Elzerman readout technique is strongly affected by temperature and thus the thermal broadening of the reservoir limits the experimentally accessible regime to ≈ 1 K. At base temperature (fridge temperature < 10 mK, electron temperature 108 mK, see Sec. 4.7) we measure a maximum T_1 of 145 ms at $B_0 = 1$ T. We find that even when increasing the temperature to 1.1 K, T_1 is 2.8 ms. This is more than an order of magnitude larger than the longest T_2^* reported in silicon quantum dots [5], and suggests that the dephasing time remains the limiting timescale for qubit control.

4.3. SPIN RELAXATION IN SILICON QUANTUM DOTS

In order to understand the magnetic field and temperature dependence of the relaxation rate, we need to consider the mixing between spin and valley. In silicon the four lowest spin-valley states are [11]: $|1\rangle = |v_-,\downarrow\rangle$, $|2\rangle = |v_-,\uparrow\rangle$, $|3\rangle = |v_+,\downarrow\rangle$, $|4\rangle = |v_+,\uparrow\rangle$ (see Fig. 4.2 (a)). In presence of interface disorder, spin-orbit interaction can couple states with different valleys and spins, introducing a channel for spin relaxation [4]. This leads to the eigenstates $|1\rangle, |\bar{2}\rangle, |\bar{3}\rangle, |4\rangle$, where:

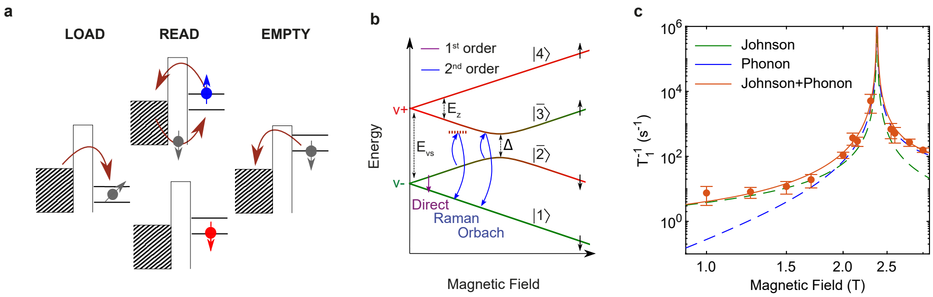

Figure 4.2: **a** Pulsing sequence used to perform single-shot readout of the electron spin [10] in the case $E_Z < E_{\mathrm{VS}}$. Above the valley splitting there is also an intermediate level between the ground and excited spin state, corresponding to the spin-down state of the excited valley. **b** Energy levels in a silicon quantum dot, showing both valley and spin degrees of freedom. As an example, the transition $\Gamma_{\bar{2}\bar{1}}$ is sketched in first-order and in second-order via virtual and resonant transitions. **c** Relaxation rate as a function of magnetic field. The fittings include contributions from Johnson and phonon mediated relaxation obtained through the model explained in the main text. From the fittings of the magnetic field and temperature dependence we extract $E_{\mathrm{VS}} = 275\,\mu\mathrm{eV}$, $\Gamma_0^J(E_{\mathrm{VS}}/\hbar) = 2\cdot 10^{-12}\mathrm{sec}$, $\Gamma_0^{ph}(E_{\mathrm{VS}}/\hbar) = 6\cdot 10^{-12}\mathrm{sec}$ and $\Delta = 0.4\,\mathrm{neV}$.

$$\left|\bar{2}\right\rangle = \left(\frac{1-a}{2}\right)^{1/2}|2\rangle - \left(\frac{1+a}{2}\right)^{1/2}|3\rangle \tag{4.1}$$

$$\left|\bar{3}\right\rangle = \left(\frac{1+a}{2}\right)^{1/2}|2\rangle + \left(\frac{1-a}{2}\right)^{1/2}|3\rangle\,. \tag{4.2}$$

Here we have $a = -(E_{\mathrm{VS}} - \hbar\omega_{\mathrm{Z}})/\sqrt{(E_{\mathrm{VS}} - \hbar\omega_{\mathrm{Z}})^2 + \Delta^2}$, where Δ is the splitting at the anticrossing point of the states $|2\rangle$ and $|3\rangle$, E_{VS} is the valley splitting and $\hbar\omega_{\mathrm{Z}}$ the Zeeman energy. In the presence of electric fields, the electrons in the excited states $\left|\bar{2}\right\rangle$ and $\left|\bar{3}\right\rangle$ can relax to the ground state $|1\rangle$, because they are in an admixture of spin and valley states. We define a relaxation rate Γ_{sv}, corresponding to $\Gamma_{\bar{2}1}$ and $\Gamma_{\bar{3}1}$ before and after the anticrossing, respectively. The resulting expression is [12]:

$$\Gamma_{\mathrm{SV}} = \Gamma_{\mathrm{V_+V_-}}(\omega_{\mathrm{Z}})F_{\mathrm{SV}}(\omega_{\mathrm{Z}}) \tag{4.3}$$

where $\Gamma_{\mathrm{V_+V_-}}$ is the pure valley relaxation rate and $F_{\mathrm{SV}}(\omega_z) = (1-|a(\omega_z)|)$. When $E_{\mathrm{VS}} = E_{\mathrm{Z}}$, the function F_{SV} peaks and the spin relaxation equals the fast pure valley relaxation [4]. From the location of this relaxation hot spot we determine a valley splitting E_{VS} of 275 μeV, comparable with values reported in other works [5].

Possible sources of electrical noise include $1/f$ charge noise, Johnson noise and phonon noise. We measure small values for charge noise (see Fig. 4.3d-e) and thus neglect their contribution, further justified by the high frequencies of 20-100 GHz, associated with the Zeeman energies studied here ($1\,\mathrm{T} < B_0 < 3\,\mathrm{T}$). We also neglect the Johnson noise coming from the circuits outside the dilution refrigerator since all room temperature electronics are well filtered. The most relevant of these noise sources is the arbitrary waveform generator used to apply voltage pulses. However, the corresponding lines are attenuated by 12 dB and have an intrinsic cut-off frequency of 1 GHz, making the noise in the

20-100 GHz range negligible. Another possible source of Johnson noise is the resistive 2DEG, which generates electric field fluctuations that have a capacitive coupling to the quantum dot. In the present device, the main contribution is likely due to the 2DEG underneath the reservoir gate, which is in close proximity to the quantum dot.

The remaining contributions are Johnson noise and phonons. The pure valley relaxation for these two cases is given by [4, 12]:

$$\Gamma^{\mathrm{J}}_{\mathrm{v_+v_-}}(\omega) = \Gamma^{\mathrm{J}}_0 \cdot \left(\frac{\omega}{\omega_{\mathrm{vs}}}\right)[1 + 2n_b(\hbar\omega, k_{\mathrm{B}}T)] \tag{4.4}$$

$$\Gamma^{\mathrm{ph}}_{\mathrm{v_+v_-}}(\omega) = \Gamma^{\mathrm{ph}}_0 \cdot \left(\frac{\omega}{\omega_{\mathrm{vs}}}\right)^5 [1 + 2n_b(\hbar\omega, k_{\mathrm{B}}T)], \tag{4.5}$$

where $\hbar\omega$ is the energy difference, $\omega_{\mathrm{vs}} = E_{\mathrm{vs}}/\hbar$ is a normalization constant and n_b is the Bose-Einstein distribution. The two contributions can be distinguished by the different magnetic field dependence that follows from $\omega_{\mathrm{z}} F_{\mathrm{sv}}(\omega_{\mathrm{z}})$ in the case of Johnson noise and from $\omega_{\mathrm{z}}^5 F_{\mathrm{sv}}(\omega_{\mathrm{z}})$ for phonons. As shown in Fig. 4.2c the magnetic field dependence of T_1 at base electron temperature can be explained in terms of Johnson mediated relaxation dominant at low fields, and a phonon contribution, mainly relevant for $\hbar\omega_{\mathrm{z}} > E_{\mathrm{vs}}$.

4.4. TEMPERATURE DEPENDENCE OF THE RELAXATION RATE

We now discuss the temperature dependence, shown in Fig. 4.3a. As shown in Eq. (4.4) and (4.5), the temperature dependence is the same to first-order for phonon and Johnson noise and given by $1 + 2n_b(\hbar\omega_{\mathrm{z}}, k_{\mathrm{B}}T)$. If $\hbar\omega_{\mathrm{z}} \gg k_{\mathrm{B}}T$ spontaneous phonon emission dominates and the relaxation rate is temperature independent, while for $\hbar\omega_{\mathrm{z}} \ll k_{\mathrm{B}}T$ it increases linearly with temperature. The relaxation rates caused by first-order processes are shown by the blue lines in Fig. 4.3a, which fit the low temperature region of the plots. However, the same processes cannot justify the rapid increase of T_1 measured at higher temperatures. In order to explain the full temperature dependence we also need to take into account two-phonon processes.

As depicted in Fig. 4.2 (b), these transitions happen in a two-step process via intermediate states. These intermediate transitions can be energy-conserving and energy non-conserving (virtual) processes, since energy must be conserved only between the initial and the final state. We obtain a two-phonon process by expanding the spin-phonon interaction in second-order perturbation theory [13]:

$$\Gamma^{(2)}_{if} = \frac{2\pi}{\hbar}\left|\sum_k \frac{V_{fk}V_{ki}}{E_i - E_k + \frac{1}{2}i\hbar\Gamma_k}\right|^2 \delta(E_i - E_f), \tag{4.6}$$

where V_{fk}, V_{ki} are the matrix elements between the states and $1/\Gamma_k$ is the lifetime of the intermediate state, which depends on all first-order processes between k and the other states. The square of the matrix elements is proportional to the valley relaxation rate $\Gamma_{\mathrm{v_+v_-}}$. Relaxation through Johnson noise can also be expanded in second-order perturbation theory, however the temperature dependence is much weaker (see Sec. 4.6) and its contribution will therefore be neglected.

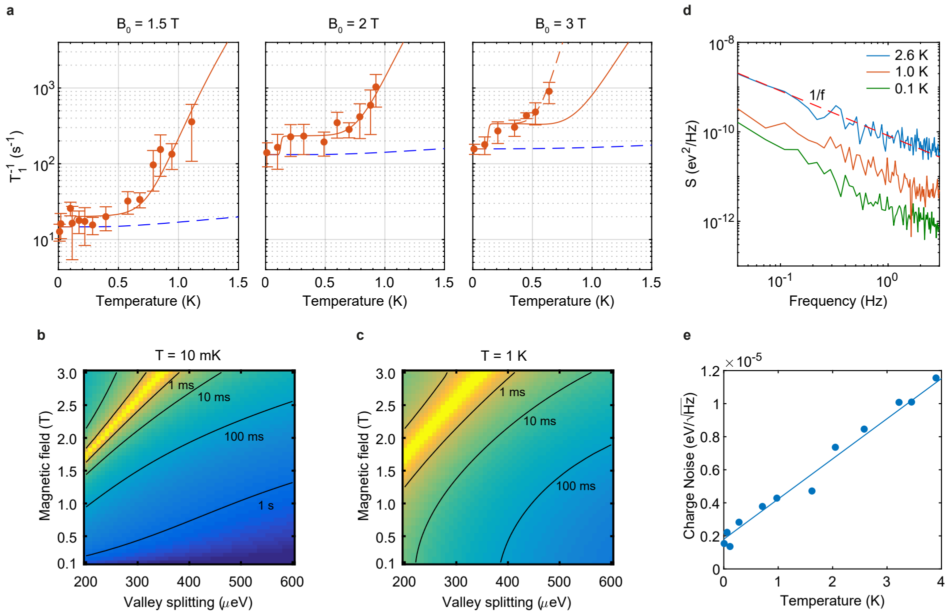

Figure 4.3: **a** Temperature dependence of the relaxation rate at B_0 =1.5 T, 2 T and 3 T. The red line is a fit taking into account Johnson and phonon noise in first and second-order. The red dashed line includes possible contributions coming from the coupling with the excited orbital states. First-order processes are shown in the dashed blue line. **b, c** Relaxation rate as a function of magnetic field and valley splitting for $T = 10\,\mathrm{mK}$ **b** and for $T = 1\,\mathrm{K}$ **c** as extracted from the model discussed in the main text. **d** Charge noise spectra obtained for three different temperatures. At higher frequencies the 1/f signal is masked by white noise. **e** Charge noise at a frequency of 1 Hz as a function of temperature fitted with a linear function.

Since the thermal energy is comparable to the level splitting in the temperature window 0.5-1 K, absorption processes cannot be neglected. In order to understand the relaxation dynamics we have developed a model that includes all possible transitions between the four spin-valley states in first and second-order. For completeness, we have also included in the model the weak coupling between the states $|1\rangle$ and $|4\rangle$. We evaluate all the transition rates and we use them to solve a 4x4 system of coupled differential rate equations given by:

$$\frac{dN_i}{dt} = -N_i \sum_{j\neq i} \Gamma_{ij} + \sum_{j\neq i} \Gamma_{ji} N_j \quad \text{for} \quad i,j = 1,\bar{2},\bar{3},4, \tag{4.7}$$

N_i being the population of the state i. The red lines in the plots in Fig. 4.3 (a) show the relaxation rates as obtained from Eq. 4.3, 4.6 and 4.7 (see also Sec. 4.6). The good agreement between model and experiment provides an indication that, even at high temperatures, relaxation is dominated by spin-valley physics. The rates relevant to the relaxation process are found to be the spin-flip transitions involving the three lowest states: $\Gamma_{\bar{2},1}$, $\Gamma_{\bar{2},\bar{3}}$ and $\Gamma_{\bar{3},1}$, $\Gamma_{\bar{3},\bar{2}}$ at E_z below and above E_{vs} respectively. The relaxation rate above 200 mK consists of a flat region followed by a rising part. We attribute this behavior to the second-order process described by Eq. 4.6. We consider separately the contributions of the resonant ($|E_i - E_k| \ll \hbar\Gamma_k$) and off-resonant transitions ($|E_i - E_k| \gg \hbar\Gamma_k$). In the first case, known as Orbach process [14], the second-order relaxation is proportional to $\left|V_{fk}V_{ki}\right|^2/\Gamma_k$ (see Sec. 4.6). At sufficiently low temperatures, the spin lifetime depends exponentially on the temperature since the numerator is proportional to n_b and the denominator is temperature independent. We therefore theoretically predict the brief steep rise around 150-200 mK. At high temperatures Γ_k also becomes proportional to n_b and the temperature dependence vanishes. This explains the main flat region that we observe in Fig. 4.3 (a), (b) and (c). For an off-resonant transition, known as Raman process, the relaxation rate scales polynomially with the temperature. As discussed in Sec. 4.6, in case of phonon-mediated transitions, a T^9 temperature dependence is obtained. The Raman process dominates over the Orbach process above 500 mK (see Fig. 4.3 (a)).

As we can see from the temperature dependence of the relaxation rate at $B_0 = 3$ T (see Fig. 4.3 (a)), the data do not match the model predictions above 500 mK, suggesting contributions to the relaxation from a different source rather than the valley mixing. We rule out second-order contributions from Johnson noise because of the much weaker temperature dependence. Possible contributions might come from a second-order process involving the excited orbital states, which is expected to give a T^{11} temperature dependence as discussed in Sec. 4.6. Coupling to orbital states can potentially give a magnetic field dependence that would make it not observable at lower fields. Coupling to orbital states mediated by direct processes give rise to a B_0^2 field dependence; this phenomenon is known as Van Vleck cancellation, a consequence of Kramer's theorem [15]. For two-phonon processes, Van Vleck cancellation together with the spin-valley mixing can potentially give an even stronger field dependence.

The spin lifetime can be increased by reducing the spin-valley coupling. As shown in Eq. 4.1 and 4.2, it can be strongly increased by reducing the applied magnetic field or by increasing the valley splitting energy. In Si-MOS the valley splitting can be electrically controlled and increased to $E_{\text{vs}} \approx 1$ meV [5, 16]. Figure 4.3b,c show the magnetic field and the valley splitting energy dependence of the relaxation rate for $T = 10\,\text{mK}$ and $T = 1\,\text{K}$, using the parameters extracted from our numerical fittings of the experimental data. These results predict a spin lifetime at 1 K of approximately 500 ms, when $B_0 = 0.1$ T and $E_{\text{vs}} = 575\,\mu\text{eV}$. The relaxation at low magnetic fields is predicted to be dominated by second-order processes even at low temperature, due to the stronger field dependence of the first-order processes.

4.5. TEMPERATURE DEPENDENCE OF THE CHARGE NOISE

Charge noise can be attributed to defects that can trap or release charges, giving rise to electrical noise. In a minimal model, these defects are treated as two-level systems with a lorentzian power spectrum $L(\omega,\gamma)$, where γ is the relaxation rate [17]. The total noise spectrum can then be obtained by integrating over all the fluctuators:

$$S(\omega) \approx \int_0^\infty L(\omega,\gamma)P(\gamma)\mathrm{d}\gamma, \tag{4.8}$$

where $P(\gamma)$ is the probability distribution of the relaxation rates. Among all processes it is common to assume thermally activated fluctuators where the switching rate exponentially depends on the inverse of the temperature $\gamma = \gamma_0 e^{-E/k_\mathrm{B}T}$, where E is the activation energy. The problem of the distrubution of the relaxation rates has now become a problem of the distribution of activation energies E. By substituing in Eq. 4.8 we obtain:

$$S(\omega) \approx \int_0^\infty L_\gamma(\omega, E) \frac{k_\mathrm{B}T}{\gamma} P(E)\mathrm{d}E, \tag{4.9}$$

where $P(E)$ is the distribution of activation energies. When $P(E)$ is constant, a $1/f$ spectrum and a linear temperature dependence are obtained. When the two-level fluctuators have a non-uniform distribution of activation energies, $S(\omega)$ will deviate both from the $1/f$ spectrum and the linear temperature dependence. These anomalies dependencies have also been observed in Si-SiGe samples [18].

We measure the charge noise in our device as current fluctuations of the sensing dot tuned to a regime with a high slope dI/dV, to maximize the sensitivity. The time trace of the current is converted to voltage noise by dividing by the slope; then the spectrum is obtained through a Fourier transform. The same process is repeated in Coulomb blockade in order to subtract the baseline noise coming from the electronics [19]. Finally, the voltage fluctuations are converted to energy fluctuations by using the lever arm α_ST = 0.18 eV/V of the sensing dot. The spectra shown in Fig. 4.3d, scale as 1/f for the probed frequency regime. Fig. 4.3e shows the temperature dependence of the charge noise at a fixed frequency of 1 Hz. We observe a linear increase of the charge noise over more than one decade of temperature (0.1-4 K), changing from approximately 2 $\mu\mathrm{eV}/\sqrt{\mathrm{Hz}}$ to 12 $\mu\mathrm{eV}/\sqrt{\mathrm{Hz}}$. This is indicating a different relation than the simple model discussed above, which assumes an equal distribution of thermally activated fluctuators. The offset measured at low temperature can be attributed to electrical noise that couples to the sensing dot via the gates.

4.6. SECOND-ORDER PROCESSES AND RATE EQUATIONS

We will now provide a more rigorous justification for the conclusions we drew in the previous sections about the temperature dependence of the spin relaxation process. As an example, we will analyse the relevant contributions to the relaxation rate for $B_0 = 2$ T, shown in Figure 4.4a and b. The low temperature regime is dominated by a first-order process between the states $|\bar{2}\rangle$ and $|1\rangle$. According to Eq. 4.4 and 4.5 of the main text, it is composed of a flat initial part followed by a linear increase. At higher temperatures, the second-order process mediated by phonons between the states $|\bar{2}\rangle$ and $|\bar{3}\rangle$ becomes dominant. We can better understand its functional form by expanding the terms in Eq. 4.6 of the main text:

$$\Gamma^{(2)}_{\bar{2}\bar{3}} \propto \int_0^{\omega_d} \int_0^{\omega_d} \left| \sum_{k \neq 2,3} \frac{c_{2k}\, c_{k3}}{\Delta E_{\bar{2}k} - \hbar\omega' + \frac{1}{2} i\hbar\Gamma_k} \right|^2 \omega'^5 \omega''^5 [1 + n_b(\hbar\omega')] n_b(\hbar\omega'') \\ \delta(\Delta E_{\bar{3}\bar{2}} + \hbar\omega' - \hbar\omega'') d\omega' d\omega'', \tag{4.10}$$

where ω_d is the Debye frequency and the coefficients c_{ij} come from the overlap between the states i, j due to mixing between spin and valley. In silicon, the electron-phonon interaction is mediated by deformation potential phonons. Therefore, the matrix elements have an additional factor ω^2 with respect to the standard interaction with piezoelectric phonons, because of the $\sqrt{q}$ dependence of the strain caused by deformation potential phonons, where q is the wave number.

As discussed in the main text, $\frac{1}{2}\hbar\Gamma_k$ represents the energy width of the k state, determined by its lifetime. Since the ground state of the system $|1\rangle$ has, at least at low temperature, a long lifetime compared to the state $|4\rangle$, $\Gamma_4 \gg \Gamma_1$, we can neglect the transitions through the state $|4\rangle$ in the sum of Eq. 4.10. In the following, we will consider separately the contributions to the integral coming from off-resonant ($\hbar\omega' \neq \Delta E_{\bar{2}1}$) and resonant ($\hbar\omega' \approx \Delta E_{\bar{2}1}$) phonons.

In the off-resonant case and at sufficiently high temperatures, phonons with frequencies $\hbar\omega \gg \Delta E_{\bar{2}1}, \Delta E_{\bar{3}\bar{2}}$ are well populated and Eq. 4.10 can be rewritten as:

$$\Gamma^{(2)}_{\bar{2}\bar{3}} = C_R T^9 \int_0^{\hbar\omega_d/k_\mathrm{B}T} \frac{e^x}{(e^x-1)^2} dx \tag{4.11}$$

and the relaxation rate scales to a good approximation as T^9. In the intermediate regime $\Delta E_{\bar{2}1} \gg \hbar\omega \gg \Delta E_{\bar{3}\bar{2}}$, the term $\hbar\omega'$ in the denominator of Eq. 4.10 can be neglected and the relaxation rate scales as T^{11}. In our experimental case, the energy differences between the levels are comparable with each other and thus this last regime is not visible in the experimental data. Instead, if we consider coupling with orbital states, these conditions apply and a T^{11} dependence is expected. The power laws we found are strictly related to the power of the ω terms in Eq.4.10, which depends on the particular nature of the electron-phonon interaction. For example, in GaAs, where piezoelectric phonons dominates over deformation potential phonons, the power is reduced to three instead of five, which leads to a T^5 and T^7 temperature dependence. In case of Johnson mediated relaxation an even weaker temperature dependence is obtained.

In the resonant case, we have $\hbar\omega' \approx \Delta E_{\bar{2}1}$ and Eq. 4.10 can be approximated as:

$$\Gamma^{(2)}_{\bar{2}\bar{3}} = C_O \frac{[1 + n_b(\Delta E_{\bar{2}1})]\, n_b(\Delta E_{\bar{2}1} + \Delta E_{\bar{2}\bar{3}})}{\Gamma_1}, \tag{4.12}$$

where the lifetime of the k state is in general evaluated as the inverse of the sum of all first-order processes between k and the other states and it is ultimately limited by the time scale of the experiment. At sufficiently low temperatures, Γ_k is temperature independent and the relaxation rate depends exponentially on the temperature according to $\Gamma^{(2)}_{\bar{2}\bar{3}} \propto n_b(\Delta E_{\bar{2}1} + \Delta E_{\bar{2}\bar{3}})$. At higher temperatures, Γ_k becomes also proportional to $n_b(\Delta E_{\bar{2}1} + \Delta E_{\bar{2}\bar{3}})$ and the relaxation rate is given approximately by $1 + n_b(\Delta E_{\bar{2}1})$, which is temperature independent for $k_\mathrm{B}T \ll \Delta E_{\bar{2}1}$ and linear dependent for $k_\mathrm{B}T \gg \Delta E_{\bar{2}1}$. In our experimental case, this linear dependence is masked by the the Raman process. The resonant and off-resonant transitions can thereby explain all the different regimes that we see in Fig. 4.4a.

The rates in first and second-order are used to solve the 4x4 system of coupled differential rate equations:

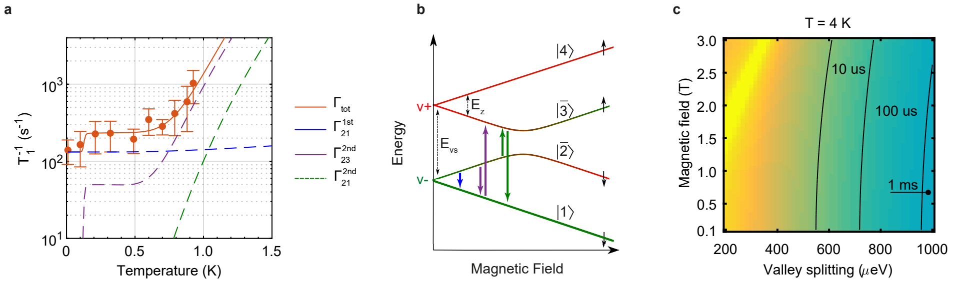

Figure 4.4: **a** Relaxation rate as a function of temperature for $B_0 = 2\,\mathrm{T}$. The dashed coloured lines show the relevant transition rates, including the first-order process between the states $|\bar{2}\rangle$ and $|1\rangle$ and second-order transitions via the states $|1\rangle$ and $|\bar{3}\rangle$. **b** The relevant transitions shown in the plot in **a** are sketched in an energy diagram. **c** Magnetic field and valley splitting dependence of the relaxation rate at a temperature of 4 K. Lifetimes larger than 1 ms are accessible with a valley splitting close to 1 meV.

$$\begin{bmatrix} \dot{N}_1 \\ \dot{N}_2 \\ \dot{N}_3 \\ \dot{N}_4 \end{bmatrix} = \begin{bmatrix} -\sum\limits_{j\neq 1}\Gamma_{1j} & \Gamma_{21} & \Gamma_{31} & \Gamma_{41} \\ \Gamma_{12} & -\sum\limits_{j\neq 2}\Gamma_{2j} & \Gamma_{32} & \Gamma_{42} \\ \Gamma_{13} & \Gamma_{23} & -\sum\limits_{j\neq 3}\Gamma_{3j} & \Gamma_{43} \\ \Gamma_{14} & \Gamma_{24} & \Gamma_{34} & -\sum\limits_{j\neq 4}\Gamma_{4j} \end{bmatrix} \cdot \begin{bmatrix} N_1 \\ N_2 \\ N_3 \\ N_4 \end{bmatrix}. \tag{4.13}$$

N_i being the population of the state i. For each temperature we extract the four eigenvalues of the matrix. Among the four, one equals zero and corresponds to the stationary population of the levels after the relaxation process is over. Two are much greater than the inverse time scale of the experiment and are therefore discarded, since they correspond to exponential decays not observable in the experiment. Finally, the remaining one represents the time constant that characterizes the single exponential decay of the spin-up fraction as a function of load time. This rate is shown in Fig. 4.3a-c.

We did not discuss relaxation due to the residual ^{29}Si nuclei. However, the presence of nuclei mainly affects the dephasing of the electron spin rather than relaxation, due to the large Zeeman energy mismatch. The modulation of hyperfine coupling by phonons is also suppressed in natural silicon due the low concentration of ^{29}Si nuclei [20]. The effect can be expected to be even smaller in our case, where the substrate is made of ^{28}Si.

As discussed in the previous section, the spin lifetime can be further improved by working in a low magnetic field and high valley splitting regime. Fig. 4.4c show this depedence at a temperature of 4 K, where second-order phonon processes dominate the relaxation process. Even at this relatevely high temperature, we extract lifetimes larger than 1 ms for a valley splitting close to 1 meV, which is a very promising result for qubits operating at a temperature of 4 K.

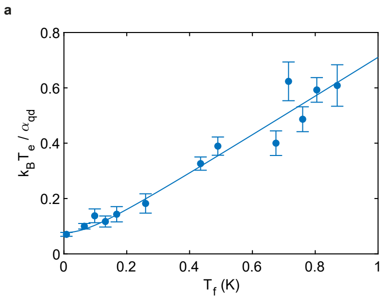

Figure 4.5: **a** Width of the (0→1) charge-state transition as a function of the fridge temperature. The red line is a fit according to Eq. 4.14 and 4.15. At sufficiently high temperatures, T_e equals T_f and the transition width increases linearly with a slope proportional to the inverse of the lever arm. At low temperature T_f becomes smaller than T_0 and the transition width becomes independent of T_f.

4.7. MEASUREMENT OF THE ELECTRON TEMPERATURE AND THE LEVER ARM OF THE QUANTUM DOT

Both the base electron temperature and the lever arm of the quantum dot have been extracted by a unique measurement, where the width of the charge transition (0→1) shown by the red arrow in Fig. 1 (b) of the main text is measured as a function of the nominal fridge temperature [21]. The charge stability diagram shown in Fig. 1 (b), is measured via a double-lockin technique, where the transconductance dI_s/dP_1 of the sensing dot is measured by applying an AC excitation V_{AC} to the gate P1. During the map, the current I_s of the sensing dot is kept at the most sensitive point by using a digitally-controlled feedback. The width of the transition is determined by V_{AC} for large AC excitations and by the thermal broadening due to the finite electron temperature T_e when $V_{AC} \ll k_\mathrm{B} T_e$. In these conditions the transconductance dI_s/dP_1 is proportional to the derivative of the Fermi-Dirac distribution:

$$\frac{dI_s}{dP_1} = a\cosh^{-2}\left(\frac{\alpha_{P1}(P_1 - b)}{2k_\mathrm{B}T_e}\right) + c, \tag{4.14}$$

where a, b and c are fitting parameters and α_{P1} is the lever arm of the quantum dot. The electron temperature T_e depends on the nominal fridge temperature T_f and the base electron temperature T_0 according to:

$$T_e = \sqrt{T_0^2 + T_f^2}. \tag{4.15}$$

We fix the gate P2 such that the tunneling rate between dot and reservoir is maximized and therefore the signal to noise ratio in the charge stability diagram is also maximized. We sweep the gate P1 in the direction of the first charge transition. During the sweep we apply an AC excitation to the gate P1 of 15 μV at 133 Hz.

Fig. 4.5 shows the width of the transition as a function of T_f. The width is for all points much higher than the excitation applied to the gate P1 meaning that we are in the conditions of a thermally limited transition. From the fit we extract a lever arm of $\alpha_{P1} = 0.122 \pm 0.005$ eV/V and a base electron temperature of $T_0 = 108 \pm 13$ mK.

REFERENCES

[1] L. Petit, J. Boter, H. Eenink, G. Droulers, M. Tagliaferri, R. Li, D. Franke, K. Singh, J. Clarke, R. Schouten, *et al.*, *Spin lifetime and charge noise in hot silicon quantum dot qubits,* Physical Review Letters **121**, 076801 (2018).

[2] M. Xiao, M. House, and H. Jiang, *Measurement of the spin relaxation time of single electrons in a silicon metal-oxide-semiconductor-based quantum dot,* Physical Review Letters **104**, 096801 (2010).

[3] C. Simmons, J. Prance, B. Van Bael, T. S. Koh, Z. Shi, D. Savage, M. Lagally, R. Joynt, M. Friesen, S. Coppersmith, *et al.*, *Tunable spin loading and t 1 of a silicon spin qubit measured by single-shot readout,* Physical Review Letters **106**, 156804 (2011).

[4] C. H. Yang, A. Rossi, R. Ruskov, N. S. Lai, F. A. Mohiyaddin, S. Lee, C. Tahan, G. Klimeck, A. Morello, and A. S. Dzurak, *Spin-valley lifetimes in a silicon quantum dot with tunable valley splitting,* Nature Communications **4**, 2069 (2013).

[5] M. Veldhorst, J. Hwang, C. Yang, A. Leenstra, B. de Ronde, J. Dehollain, J. Muhonen, F. Hudson, K. M. Itoh, A. Morello, *et al.*, *An addressable quantum dot qubit with fault-tolerant control-fidelity,* Nature Nanotechnology **9**, 981 (2014).

[6] T. Castner Jr, *Direct measurement of the valley-orbit splitting of shallow donors in silicon,* Physical Review Letters **8**, 13 (1962).

[7] M. Reed, B. Maune, R. Andrews, M. Borselli, K. Eng, M. Jura, A. Kiselev, T. Ladd, S. Merkel, I. Milosavljevic, *et al.*, *Reduced sensitivity to charge noise in semiconductor spin qubits via symmetric operation,* Physical Review Letters **116**, 110402 (2016).

[8] F. Martins, F. K. Malinowski, P. D. Nissen, E. Barnes, S. Fallahi, G. C. Gardner, M. J. Manfra, C. M. Marcus, and F. Kuemmeth, *Noise suppression using symmetric exchange gates in spin qubits,* Physical Review Letters **116**, 116801 (2016).

[9] C. H. Yang, W. H. Lim, F. A. Zwanenburg, and A. S. Dzurak, *Dynamically controlled charge sensing of a few-electron silicon quantum dot,* AIP Advances **1**, 042111 (2011).

[10] J. Elzerman, R. Hanson, L. W. Van Beveren, B. Witkamp, L. Vandersypen, and L. P. Kouwenhoven, *Single-shot read-out of an individual electron spin in a quantum dot,* Nature **430**, 431 (2004).

[11] F. A. Zwanenburg, A. S. Dzurak, A. Morello, M. Y. Simmons, L. C. L. Hollenberg, G. Klimeck, S. Rogge, S. N. Coppersmith, and M. A. Eriksson, *Silicon quantum electronics,* Reviews of Modern Physics **85**, 961 (2013).

[12] P. Huang and X. Hu, *Spin relaxation in a si quantum dot due to spin-valley mixing,* Physical Review B **90**, 235315 (2014).

[13] K. Shrivastava, *Theory of spin–lattice relaxation,* physica status solidi (b) **117**, 437 (1983).

[14] R. Orbach, *Spin-lattice relaxation in rare-earth salts,* in *Proceedings of the Royal Society of London A: Mathematical, Physical and Engineering Sciences*, Vol. 264 (The Royal Society, 1961) pp. 458–484.

[15] A. Abragam and B. Bleaney, *Electron paramagnetic resonance of transition ions* (OUP Oxford, 2012).

[16] A. Laucht, J. T. Muhonen, F. A. Mohiyaddin, R. Kalra, J. P. Dehollain, S. Freer, F. E. Hudson, M. Veldhorst, R. Rahman, G. Klimeck, *et al.*, *Electrically controlling single-spin qubits in a continuous microwave field,* Science advances **1**, e1500022 (2015).

[17] E. Paladino, Y. Galperin, G. Falci, and B. Altshuler, *1/f noise: Implications for solid-state quantum information,* Reviews of Modern Physics **86**, 361 (2014).

[18] E. J. Connors, J. Nelson, H. Qiao, L. F. Edge, and J. M. Nichol, *Low-frequency charge noise in si/sige quantum dots,* Physical Review B **100**, 165305 (2019).

[19] B. M. Freeman, J. S. Schoenfield, and H. Jiang, *Comparison of low frequency charge noise in identically patterned si/sio2 and si/sige quantum dots,* Applied Physics Letters **108**, 253108 (2016).

[20] C. Tahan and R. Joynt, *Relaxation of excited spin, orbital, and valley qubit states in ideal silicon quantum dots,* Physical Review B **89**, 075302 (2014).

[21] J. Prance, Z. Shi, C. Simmons, D. Savage, M. Lagally, L. Schreiber, L. Vandersypen, M. Friesen, R. Joynt, S. Coppersmith, *et al.*, *Single-shot measurement of triplet-singlet relaxation in a si/sige double quantum dot,* Physical Review Letters **108**, 046808 (2012).

5

UNIVERSAL QUANTUM LOGIC IN HOT SILICON QUBITS

The investigation of 'hot' qubit operation began in chapter 3 with the demonstration of a double quantum dot that can be formed and precisely controlled despite the elevated temperature. Chapter 4 addresses the problem of the two main temperature dependent parameters for spin qubits: spin lifetime and charge noise. Despite both being affected by temperature, sufficiently long lifetimes and moderately high charge noise values have been measured above 1 K, demonstrating that the temperature dependence of these two parameters do not present a roadblock for 'hot' qubit operation. In this chapter we add the last piece to the picture and show control of a two-qubit system operating at a temperature of 1.1 K. The two qubits reside in a double quantum dot where initialization and readout occur via Pauli-spin-blockade to mitigate the effect of temperature. We drive the single-qubit gates using an on-chip microwave antenna and characterize their performances, revealing control fidelities of 98.7 % and 99.3 %. By switching on the exchange interaction between the two electrons we achieve coherent controlled-rotations and test the universality of our gate set via two-qubit randomized benchmarking. Additionally, we investigate the limiting factors to the dephasing times, and characterize their weak temperature dependence.

Parts of this chapter have been published in **Nature 580**, 355-359 (2020) [1].

5.1. A QUANTUM INTEGRATED CIRCUIT

Spin qubits based on quantum dots are among the most promising candidates for large-scale quantum computation [2–4]. Quantum coherence can be maintained in these systems for extremely long times [5] by using isotopically enriched silicon (^{28}Si) as the host material [6]. This has enabled the demonstration of single-qubit control with fidelities exceeding 99.9% [7, 8] and the execution of two-qubit logic [9–12]. The challenge is now to increase the qubit count and demonstrate that quantum operations can still be efficiently performed in large arrays.

The potential to build large systems with quantum dots manifests in the ability to deterministically engineer and optimize qubit locations and interactions using a technology that greatly resembles today's complementary metal-oxide semiconductor (CMOS) manufacturing. Nonetheless, quantum error correction schemes predict that millions to billions of qubits will be needed for practical quantum information [13]. Considering that today's devices make use of more than one terminal per qubit [14], wiring up such large systems remains a formidable task. In order to avoid an interconnect bottleneck, quantum integrated circuits hosting the qubits and their electronic control on the same chip have been proposed [4, 15, 16]. Inspired by their classical counterpart where only a few control lines are needed to interact with billions of transistors, a quantum integrated circuit hosts the quantum hardware and its electronic control on the same chip to provide a scalable solution. While these architectures provide an elegant way to increase the qubit count to large numbers by leveraging the success of classical integrated circuits, a key question is whether the qubits will be robust against the thermal noise imposed by the power dissipation of the electronics. Demonstrating a universal gate set at elevated temperatures is therefore a milestone in the effort towards scalable quantum systems.

Here, we solve this challenge and combine initialization, readout, single-qubit rotations and two-qubit gates, to demonstrate full two-qubit logic in a quantum circuit operating at 1.1 Kelvin. We furthermore examine the temperature dependence of the quantum coherence which we find, unlike the relaxation process [17], to be hardly affected in a temperature range T = 0.45 K - 1.25 K.

5.2. HIGH TEMPERATURE READOUT AND INITIALIZATION

Figure 5.1a shows the silicon quantum dot device. The qubits are realized in an isotopically purified ^{28}Si epi-layer with a ^{29}Si residual concentration of 800 ppm. The fabrication of the quantum dot device is based on an overlapping gate-scheme to allow for tightly confined quantum dots [20, 21]. Electrons can be loaded either from the reservoir or from the single-electron-transistor (SET) [18], which is also used for charge sensing. To allow for coherent control over the electron spins, AC currents are applied through the on-chip aluminum microwave antenna.

Figure 5.1b shows a charge stability diagram of the double quantum dot, where the qubits Q1 and Q2 and their coupling are defined by using the gates P1, B12, and P2. Since we can freely choose the occupancy of the two quantum dots we tune to the regime where we obtain optimal exchange coupling, which we find with one and five electrons for Q1 and Q2 respectively. We then operate the system close to the (5,1)-(4,2) charge anticrossing.

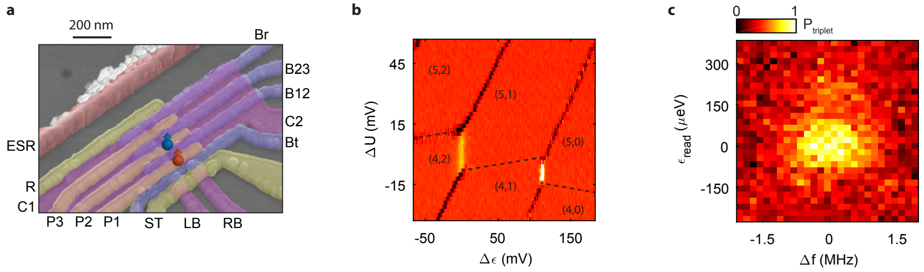

Figure 5.1: **a** Scanning Electron Microscope (SEM) image of a quantum device identical to the one measured. Gates P1 and P2 define the two quantum dots and the gate B12 control the inter-dot tunnel coupling. The SET is defined by the top gate ST and the two barriers RB and LB, and it is used both as charge sensor and as reservoir [18], while the tunnel rate is controlled by Bt. The gates C1 and C2 confine the electrons in the three quantum dots. Gates R, Br, P3 and B23 are kept grounded during the experiment. **b** Electron occupancy as a function of detuning energy between the two quantum dots ϵ and on-site repulsion energy U. The data have been centered at the (4,2)-(5,1) anticrossing. The electron transitions have been measured via a lock-in technique [19], by applying an excitation of 133 Hz on the gate B12. Both electrons are loaded from the SET, with Q2 having a tunneling rate significantly lower than Q1. **c** Readout signal as a function of readout position ϵ_{read} and microwave frequency applied to Q2. When the readout level is positioned between the singlet-triplet energy splitting and the microwave frequency matches the resonance frequency of Q2, we correctly read out the transition from the state $|\downarrow\uparrow\rangle$ to the blocked state $|\uparrow\uparrow\rangle$.

Single spins are often initialized via energy-selective tunneling to a nearby reservoir [22]. However, this method requires a Zeeman splitting much higher than the thermal broadening, limiting the fidelity and making the method unpractical for high temperature operation. Instead, Pauli spin blockade offers a convenient mechanism to perform initialization and readout [4, 23], with a relevant energy scale corresponding to the singlet-triplet energy splitting, which is set by the large and tunable valley splitting energy in silicon metal-oxide-semiconductor (SiMOS) devices [24]. This method is more robust against thermal noise and enables independent optimization of the qubit operation frequency. We choose to set the magnetic field to $B = 0.25$ T, which corresponds to addressable qubits with Larmor frequencies $\nu_{Q1} = 6.949$ GHz and $\nu_{Q2} = 6.958$ GHz in the absence of exchange interaction. This low frequency operation reduces the qubit sensitivity to electrical noise that couples in via the spin-orbit coupling [25]. Additionally it also simplifies the demands on the electronic control circuits and reduces the cable losses.

The pulse sequence used in the experiment is schematically shown in Fig. 5.3a. The sequence starts by pulsing deep into the (4,2) charge state, where the spins quickly relax to the singlet state. An adiabatic pulse to the (5,1) regime is applied to initialize the system in the $|\downarrow\uparrow\rangle$ state. At this position in detuning energy ϵ, single- and two-qubit gate operations are performed by applying a microwave burst with variable frequency and duration. The sequence ends by adiabatically pulsing to the anticrossing where readout is performed. The antiparallel spin state with the lowest energy (which is in this experiment the state $|\downarrow\uparrow\rangle$) couples directly to the singlet (4,2) charge state. The remaining antiparallel spin state ($|\uparrow\downarrow\rangle$) and the two parallel spin states ($|\uparrow\uparrow\rangle$, $|\downarrow\downarrow\rangle$) couple to the three triplet (4,2) charge states. This allows to map the $|\downarrow\uparrow\rangle$ and the other basis states to different charge configurations ((4,2) or (5,1) states), which can be read out using the SET. As

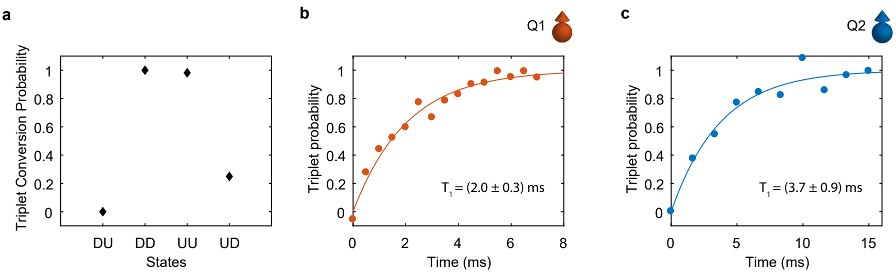

Figure 5.2: **a** Normalized probability of detecting the four two-electron spin states as a triplet state (U, spin up; D, spin down). The probability that the triplet antiparallel spin state is correctly identified as a triplet can be reduced by the non-perfect adiabaticity of the pulse and by a faster triplet–singlet relaxation. **b-c** Single-spin relaxation times of Q1 and Q2. The measurements are performed by fitting the decay of the states $|\downarrow\uparrow\rangle$ and $|\uparrow\downarrow\rangle$ to the $|\downarrow\downarrow\rangle$ state. We extract $T_{1(Q1)} = 2.0$ ms and $T_{1(Q2)} = 3.7$ ms, consistent with [17]. Triplet probabilities have been normalized to remove readout errors.

shown in Fig. 5.1c, the optimal readout position can be obtained by sweeping ϵ and applying a π-pulse to Q2. From the detuning lever arm of $\alpha_\epsilon = 0.044$ eV/V, extracted from the thermal broadening of the polarization line, we find a readout window of 155 µeV where we can efficiently discriminate between the singlet and triplet states.

In this high temperature operation mode, the readout visibility is mainly limited by the broadening of the SET peaks. In order to maximize our sensitivity we subtract a reference signal from each trace, obtained from a sequence where no microwave pulses are applied. Finally we average and normalize the resulting signal. Relaxation processes can in principle differ for the four two-electron spin states, leading to a different spin conversion probability to the (4,2) charge state. Fig. 5.2a shows the normalized readout amplitude for all the four states. We note that the probability for the $|\uparrow\downarrow\rangle$ state is significantly lower than for two parallel spin states. This can be attributed to a faster relaxation that can occur via some finite coupling between the $\mathrm{T}_{(1,5)}$ and $\mathrm{S}_{(1,5)}$. A non-perfect adiabaticity of the pulse can also reduce conversion fidelities. In this experiment we use a ramp of 1 µs and an integration time of 40 µs limited by the cut-off of the current to voltage converter.

Furthermore we measure the spin lifetimes of the two qubits (see Fig. 5.2b and c) by measuring the decay of the states $|\downarrow\uparrow\rangle$ and $|\uparrow\downarrow\rangle$ to the $|\downarrow\downarrow\rangle$. The state $|\uparrow\downarrow\rangle$ is initialized via a double spin flip following the PSB initialization discussed above. We find values of $T_{1(\mathrm{Q1})} = 2.0$ ms and $T_{1(\mathrm{Q2})} = 3.7$ ms, consistent with values reported in the previous chapter at a similar operating temperature [17].

5.3. HOT AND UNIVERSAL QUANTUM LOGIC

Figure 5.3b-g shows the single-qubit characterization of the two-qubit system. We observe clear Rabi oscillations for both qubits (Fig. 5.3b and c) as a function of the microwave burst duration. From the decay of the Ramsey fringes (Fig. 5.3d and e) we extract dephasing times $T^*_{2(\mathrm{Q1})} = 2.1$ µs and $T^*_{2(\mathrm{Q2})} = 2.7$ µs , comparable to experiments at similar high temperature [26]. These times are significantly shorter than the longest reported times for ^{28}Si [5], however they are still longer than the dephasing times for

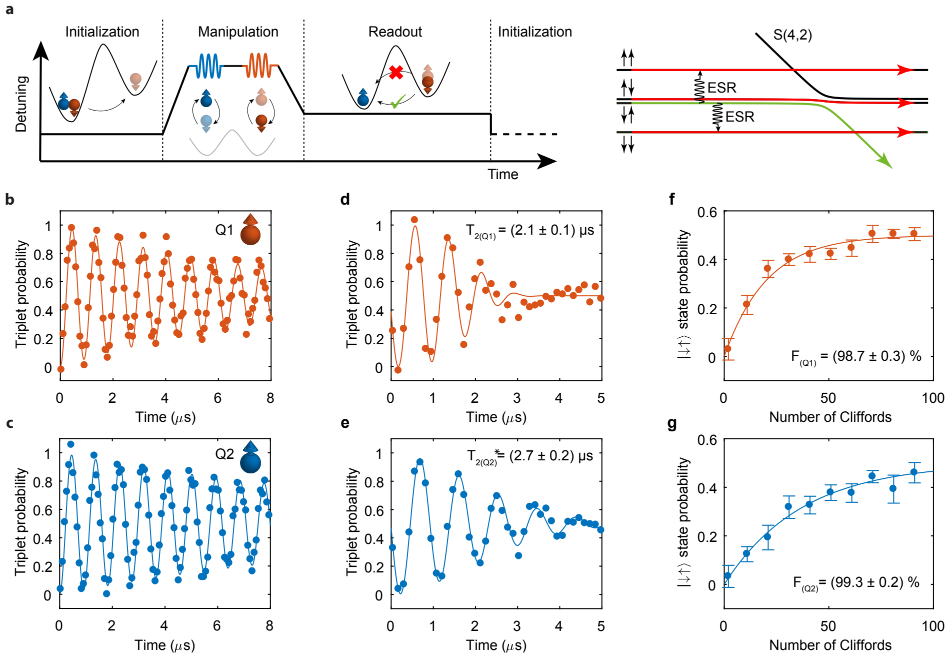

Figure 5.3: **a** Pulse sequence used for the experiments. Qubits Q1 and Q2 are defined on the spin states of single-electrons, the remaining four electrons in Q2 fill the first levels and do not contribute to the experiment. A voltage ramp allows adiabatic transitions between the (5,1) and (4,2) charge states. Each measurement cycle consists of two of these sequences. The second cycle contains no microwave pulses and it is used as a reference to cancel low-frequency drifts during readout. **b-c** Rabi oscillations for both qubits as a function of the microwave pulse duration. We extract decay time constants $T_{2(\mathrm{Q1})}^{\mathrm{Rabi}} = 8\,\mu\mathrm{s}$ and $T_{2(\mathrm{Q2})}^{\mathrm{Rabi}} = 14\,\mu\mathrm{s}$. **d-e** Decay of the Ramsey fringes for both qubits. The data correspond to the average of four traces where each point is obtained from 500 single-shot traces. **f-g** Randomized benchmarking of the single-qubit gates for both qubits. Each data point is obtained from 500 averages of 20 Clifford sequences, for a total of 10.000 single-shot traces. The fidelity reported refers to the primitive gates, while a Clifford-gate contains on average 1.875 primitive gates. We have normalized the state probabilities to remove the readout errors.

natural silicon at base temperature [10, 11].

We characterize the performance of the single-qubit gates of the two qubits by performing randomized benchmarking [27]. In the manipulation phase we apply sequences of random gates extracted from the Clifford group, followed by a recovery gate that brings the system to the $|\downarrow\downarrow\rangle$ and $|\uparrow\uparrow\rangle$ states for Q1 and Q2 respectively. By fitting the decay of the readout signal as a function of the number of applied gates to an exponential decay we extract qubit fidelities $F_{\mathrm{Q1}} = 98.7 \pm 0.3$ % and $F_{\mathrm{Q2}} = 99.3 \pm 0.2$ %, with the second one above the fault tolerant threshold.

We now turn to the two-qubit gate characterization. The ability to tune the exchange interaction [2] is the basis to perform two-qubit operations with electrons in quantum dots. By turning on the exchange interaction, either by controlling the detuning energy or the tunnel coupling, the resonance frequencies of each qubit shift depending on the spin state of the other qubit. The plot in Fig. 5.4a shows this frequency shift for both

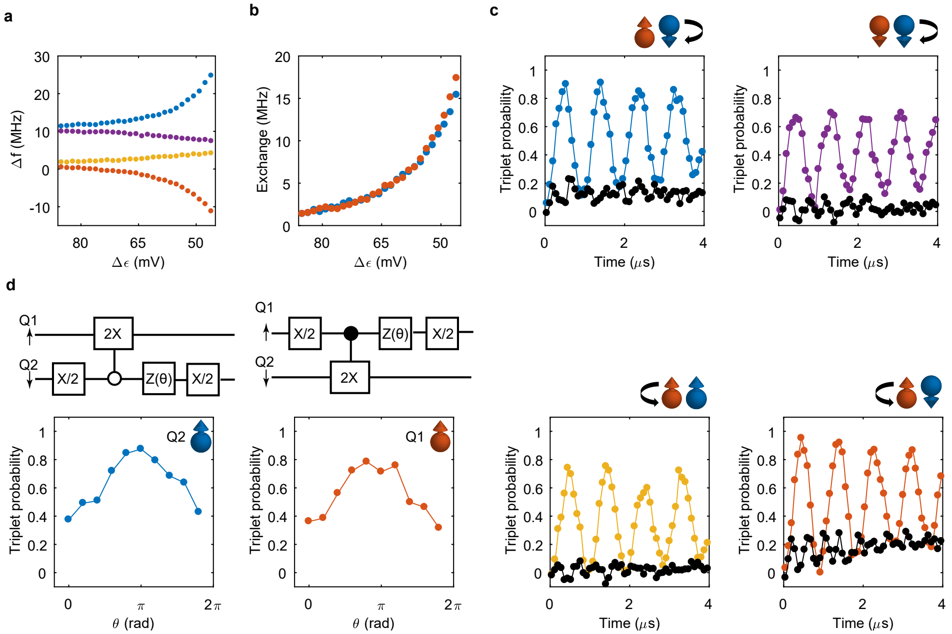

Figure 5.4: **a** Full exchange diagram of the resonance frequencies of both qubits. We measure the excited states by ESR controlled spin flips applied to the control qubit.The frequency offset is 6.948 GHz. **b** Exchange energy measured as a function of detuning. The data correspond to $f_2 - f_1$ and $f_4 - f_3$ as obtained from **a**. **c** Conditional rotations on all the frequencies f_i, the color code refers to the plot in **a**. The black lines correspond to the same transition f_i, driven with the control qubit in the opposite state. An initialization π-pulse and recovery π-pulse are applied to the control qubit for the sequences where either Q1 is in the spin down state or Q2 is in the spin up state. All Rabi frequencies are set to approximately 1 MHz by adjusting the power of the microwave source to compensate for the frequency dependent attenuation of the fridge line. **d** Phase acquired by the control qubit during a CROT operation. A CROT gate, together with a Z-rotation of $\pi/2$ on the control qubit is equivalent to a CNOT operation. Z gates are implemented by a software change of the reference frame.

qubits as a function of the detuning energy between the two quantum dots, with and without a π-pulse applied to flip the spin state of the other qubit. The full exchange spectrum is composed of the transitions f_1 ($|\downarrow\uparrow\rangle \longrightarrow |\downarrow\downarrow\rangle$), f_2 ($|\uparrow\uparrow\rangle \longrightarrow |\uparrow\downarrow\rangle$), f_3 ($|\downarrow\downarrow\rangle \longrightarrow |\uparrow\downarrow\rangle$) and f_4 ($|\downarrow\uparrow\rangle \longrightarrow |\uparrow\uparrow\rangle$). The exchange interaction J can be extracted as the differences $f_2 - f_1$ and $f_4 - f_3$, from which we measure tunable J in the range 0.5 - 18 MHz (see Fig. 5.4b). At even larger exchange couplings the readout visibility drastically reduces, which we attribute to a decrease of T_2^* (see Fig 5.5c). By fitting the exchange spectrum we extract a tunnel coupling t_c = 0.8 GHz and a Zeeman energy difference δE_Z= 9.1 MHz.

Having demonstrated the tunability of the exchange interaction, we use this to demonstrate two-qubit operation. When the exchange is turned on, the resulting shift in resonance frequency can be used to implement state selective ESR transitions (CROT), which are equivalent to a CNOT gate up to single-qubit phases. Figure 5.4c shows controlled oscillations for both qubits, with the control qubit set either to the spin down or spin up state, where we have set the exchange interaction to J = 2.5 MHz. When we prepare the state of the control qubit such that the target qubit is in resonance with the external

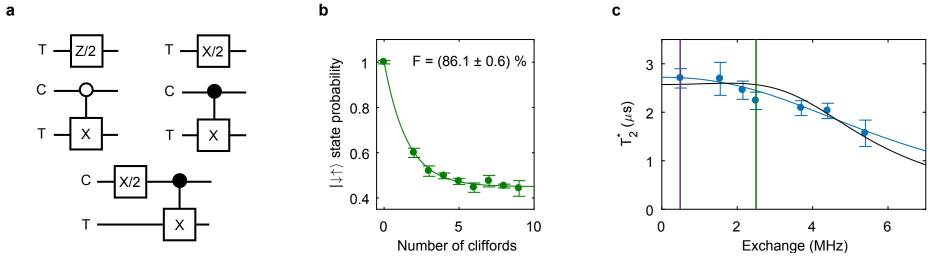

Figure 5.5: **a** Primitive gates used to generate the two-qubit Clifford group (11520 gates in total). On average, each Clifford contains 2.5694 primitive gates. Since the Z/2 gates are implemented via a software change of the reference frame, they are not included in the gate count. All gates shown in the figure (except for the Z/2 gate) are implemented with two $\pi/2$ controlled rotations. The compilation scheme is identical to the one in [12]. **b** Decay of the $|\downarrow\uparrow\rangle$ state probability as a function of the number of two-qubit Cliffords applied. A recovery gate returns the system to the $|\downarrow\uparrow\rangle$ state. Since we include the recovery gate in the Cliffords count, the first data point correponds to $N_{\text{Cliff}} = 2$. Each data point corresponds to the average of 150 random sequences. The fidelity F = 86.1 ± 0.6 % corresponds to the average fidelity of the primitve gates shown in **a**. **c** Dephasing time of Q2 as a function of the exchange interaction, fitted with a model taking into account gaussian quasi static noise, with fits accounting for fully correlated (blue line) and fully uncorrelated (black line) noise sources.

microwave control, we observe clear oscillations of the target qubit as a function of the microwave burst duration, with no significant decay after multiple rotations. When we flip the state of the control qubit, the resonance frequency of the target qubit is shifted and the target qubit is not driven by the microwave control.

In order to investigate the coherence of the two-qubit logic, we apply a sequence where we interleave a CROT operation with duration 2π in between two $\pi/2$ single-qubit gates applied to the control qubit with variable phase θ. As shown in Fig. 5.4d, when we invert the second $\pi/2$ pulse ($\theta = \pi$) this cancels out the π phase left by the CROT operation on the control qubit and we correctly measure transitions to the $|\downarrow\downarrow\rangle$ and $|\uparrow\uparrow\rangle$ states. This demonstrates the execution of a coherent CROT, since the control qubit maintains its coherence even when the target qubit is driven.

In order to show the universality of our gate set we also demonstrate two-qubit randomized benchmarking. We apply random gates from the 11520 two-qubit Clifford group, recover the state to the $|\downarrow\uparrow\rangle$ and measure how the singlet probability decays over the number of applied gates. The decay is shown in Fig. 5.5b and the primitive gates used in 5.5a. The lower fidelity (F = 86.1 ± 0.6 %) compared to the single-qubit benchmark can be attributed to the longer time spent by the qubits idling, which causes them to decohere faster. Possible improvements include simultaneous driving of two transitions to reduce idling times, optimized pulse shaping to reduce accidental excitations of nearby transitions and operation at the symmetry point [28, 29].

5.4. MODELLING THE NOISE IMPACTING THE QUANTUM COHERENCE

To further investigate the quantum coherence of the system we measure the decay of the Ramsey fringes for different values of the exchange interaction, see Fig. 5.5c. We find that by increasing the exchange interaction the coherence is reduced, which we explain by the increased qubit sensitivity to electrical noise. We can fit the data with a model that includes quasi-static electrical noise coupling in via the exchange interaction and via the Zeeman energy difference between the two qubits, that we discuss now in the following.

In a Ramsey experiment the qubits are initialized in the $|\downarrow\uparrow\rangle$ state, then brought into a superposition state different for the two qubits: $|Q2+\rangle = (|\downarrow\uparrow\rangle + |\uparrow\uparrow\rangle)/\sqrt{2}$ and $|Q1+\rangle = (|\downarrow\uparrow\rangle + |\downarrow\downarrow\rangle)/\sqrt{2}$, then mapped back after some waiting time, and finally measured. The phase $e^{-2\pi i\Phi(\tau)}$ the two qubits acquire during their free evolution is given by their energy difference $\Phi(\tau) = \int_0^\tau dt f_4$ and $\Phi(\tau) = \int_0^\tau dt f_1$. We assume that there are two dominating channels where noise can couple to the qubits, which is assumed to be longitudinal. We assume the noise comes from electrostatic fluctuations, which can couple via the detuning energy through the exchange interaction and through the g-factor modulation and spin-orbit coupling to the difference in Zeeman energy fields. The acquired phase for the two qubits are then given by

$$\Phi_{Q1,(Q2)}(t) = f_{4,(1)} + [\mathscr{D}_\epsilon \delta\epsilon(t) + \mathscr{D}_{\Delta E_z} \delta\Delta E_z(t)], \tag{5.1}$$

where $\mathscr{D}_\epsilon = \partial f_4/\partial J \times \partial J/\partial\epsilon$ and $\mathscr{D}_{\Delta E_z} = \partial f_4/\partial\Delta E_z$. The envelope of the Ramsey experiment is then given by the free induction decay [30]

$$2f(\tau) = 1 + \exp\left[-\pi i \left\langle \Phi(\tau)^2 \middle| \Phi(\tau)^2 \right\rangle\right] \tag{5.2}$$

$$1 + \exp\Big[-\pi t^2 \Big(\mathscr{D}_\epsilon^2 \sigma_\epsilon^2 + \mathscr{D}_{\Delta E_z}^2 \sigma_{\Delta E_z}^2 + \kappa^2 \mathscr{D}_\epsilon \mathscr{D}_{\Delta E_z} \sigma_\epsilon \sigma_{\Delta E_z}\Big)\Big)\Big] \tag{5.3}$$

under the assumption of Gaussian distributed noise and zero mean $\langle\Phi(\tau)|\Phi(\tau)\rangle = 0$. For the second line we assumed quasi-static noise with dispersion $\sigma_\epsilon = \int_{-\infty}^{\infty} S_\epsilon(\omega) d\omega$, where $S(\omega) = \int_{-\infty}^{\infty} \left\langle \delta\epsilon(t)^2 \middle| \delta\epsilon(t)^2 \right\rangle e^{-i\omega t} dt$ is the power spectral density of the noise. Similar expressions hold for $\sigma_{\Delta E_z}$. The correlation coefficient is defined $\kappa = \int_{-\infty}^{\infty} K_{\epsilon,\Delta E_z}(\omega) d\omega / (\sigma_\epsilon \sigma_{\Delta E_z})$ with the cross-spectral density $K_{\epsilon,\Delta E_z} = \int_{-\infty}^{\infty} \langle \delta\epsilon(t)\delta\Delta E_z(t) | \delta\epsilon(t)\delta\Delta E_z(t)\rangle e^{-i\omega t} dt$. The dephasing time is then given by

$$\left(T_2^*\right)^{-1} = \sqrt{\pi}\sqrt{\mathscr{D}_\epsilon^2 \sigma_\epsilon^2 + \mathscr{D}_{\Delta E_z}^2 \sigma_{\Delta E_z}^2 + \kappa^2 \mathscr{D}_\epsilon \mathscr{D}_{\Delta E_z} \sigma_\epsilon \sigma_{\Delta E_z}}. \tag{5.4}$$

We fit the dephasing times as a function of exchange with either a fully uncorrelated noise $\kappa = 0$ or a fully correlated $\kappa = 1$ ansatz. The fits can be seen in Fig. 5.5c. Our best fit yields $\sigma_\epsilon = 21\,\mu\text{eV}$, $\sigma_{\Delta E_z} = 400\,\text{kHz}$. Assuming that the origin of the noise is $1/f$ and knowing our measurement time, we can convert σ_ϵ to the value of its relative power spectrum at 1 Hz, a metric often reported in literature. We obtain $A_\epsilon \approx 6\ \mu\text{eV}/\sqrt{\text{Hz}}$ with $\sigma_\epsilon^2 = A_\epsilon^2 \log\left(f_{\text{uv}}/f_{\text{rf}}\right)$ [30]. The noise in ϵ is comparable with values extracted at fridge base temperature [31], and consistent with charge noise values extracted from current fluctuation measurements of SETs [17, 32]. The lower and higher cutoff $f_{\text{rf}} \sim 10^{-2}$ Hz and $f_{\text{uv}} \sim 10^3$ Hz are set by the experiment in the quasistatic approximation.

5.5. IMPACT OF TEMPERATURE ON QUBIT PERFORMANCE

To analyze the thermal impact, we characterize the temperature dependence of T_2^* for two values of exchange ($J = 0.5$ MHz and $J = 2.5$ MHz) and we find it to be approximately

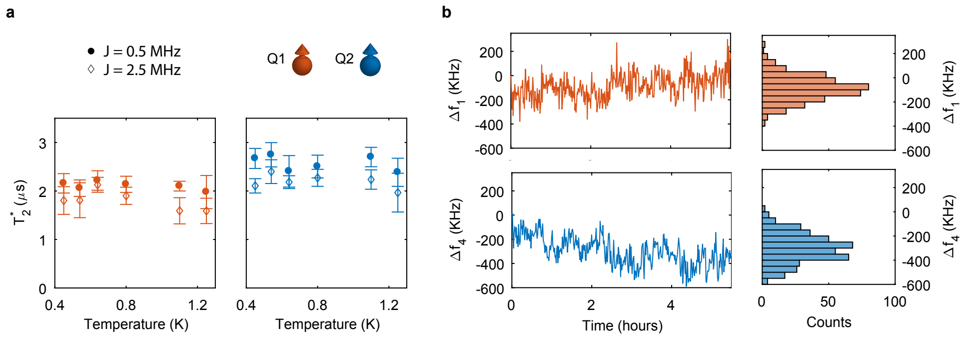

Figure 5.6: **a** Temperature dependence of the dephasing time with the exchange interaction set to the minimum obtained by sweeping ϵ ($J = 0.5$ MHz) and with the exchange interaction set to acquire the CROT operations of Fig. 5.4a ($J = 2.5$ MHz). **b** Time dependences of the resonance frequencies f1 and f4 of Q1 and Q2 respectively. The exchange interaction is set to 2.5 MHz. The data have been offset by 6.9491 GHz and 6.9620 GHz for f1 and f4 respectively.

stable in the range $T = 0.45$ K - 1.25 K (see Fig. 5.6a). While weak dependencies of T_2^* have been reported in other single-qubit experiments [26], we observe here that the weak temperature dependence is maintained even when the exchange interaction is set to an appreciable value where we can perform two-qubit logic.

The origin of the electrical noise limiting T_2^* can potentially come from extrinsic or intrinsic sources. Although we cannot rule out all extrinsic noise sources, we have confirmed that attenuating the transmission lines does not affect the T_2^* and we thus rule out a direct impact of the waveform generator and the microwave source. When intrinsic charge noise is the dominant contribution, a simple model based on an infinite number of two-level fluctuators (TLFs) predicts a square root dependence of the dephasing rate on the temperature [33]. For a large ensemble the noise spectral density reads [33]

$$S(\omega) \propto \int_{2\pi f_{\mathrm{rf}}}^{2\pi f_{\mathrm{uv}}} \mathscr{P}(\nu, T) S(\omega, \nu)\, d\nu, \tag{5.5}$$

where $\mathscr{P}(\nu, T)$ describes the contribution of the process with a switching rate between ν and $\nu + d\nu$, thus, the probability density of a TLFs that contributes to the dephasing process. Assuming a temperature dependent switching rate $\nu = \nu_0 e^{-E/(k_B T)}$ leads to $\mathscr{P}(\nu, T) = \mathscr{P}(E, T)|\partial\nu/\partial E|^{-1}$ and one finds $\mathscr{P}(\nu, T) = \mathscr{P}(E, T) k_B T/\nu$ [33]. Assuming a constant distribution of activation energies, $\mathscr{P}(E, T) =$ const and inserting this into Eq. 5.5 the characteristic $1/f$ noise with a linear temperature dependence can be reproduced [31],

$$S(\omega) \approx \mathscr{P}(E, T) k_B T \frac{2\pi}{\omega} \equiv \frac{A_\epsilon}{\omega} \tag{5.6}$$

for $2\pi f_{\mathrm{rf}} \leq \omega \leq 2\pi f_{\mathrm{uv}}$. However, recent work shows that the assumption of a constant distribution of activation energies $\mathscr{P}(E, T)$ is not entirely valid [34], and this can lead to anomalous temperature dependencies.

The small size of quantum dots, in particular SiMOS qubits, may lead to only a few TLFs being relevant for the dephasing and these may explain the observed weak temperature dependence. The power spectral density of a single TLF is given by [33]

$$S(\omega,\nu) = \frac{A}{2\cosh^2[E/(2k_B T)]}\frac{\nu}{\nu^2+\omega^2}. \tag{5.7}$$

Here, A is the coupling strength of the fluctuations, E the (activation) energy gap between the two states of the TLF, and ν the switching rate. An explanation for the weak temperature dependence of T_2^* arises from the fact that Eq. 5.7 saturates if $k_B T \gg E$. Assuming that only a few TLFs couple to our system there is only a small probability to find a TLF which has an activation energy E exactly in the temperature range between 0.4 K till 1.2 K. The same arguments hold if instead of a two-level fluctuator an Anderson impurity is the origin of charge noise [35].

In order to better quantify the imapct of temperature, we also analyze the stability of the system in the low frequency regime. Fig. 5.6b shows how the frequencies f_1 and f_4 drift over the course of 6 hours. Despite the elevated temperature, the frequency peaks, which are approximately 1 MHz broad, shift only by 200-300 KHz, making the calibration routines easy to implement. Since the exchange interaction is always on, every small variation in detuning ϵ and on-site energy U directly affects the qubit resonance frequencies. We can correlate the frequency fluctuations to variations in the readout point, meaning that low frequency charge noise dominates over magnetic noise. Therefore, the ability to turn the exchange interaction completely off should drastically reduce the magnitude of these fluctuations, simplifying even further calibration routines.

REFERENCES

[1] L. Petit, H. Eenink, M. Russ, W. Lawrie, N. Hendrickx, S. Philips, J. Clarke, L. Vandersypen, and M. Veldhorst, *Universal quantum logic in hot silicon qubits,* Nature **580**, 355 (2020).

[2] D. Loss and D. P. DiVincenzo, *Quantum computation with quantum dots,* Physical Review A **57**, 120 (1998).

[3] F. A. Zwanenburg, A. S. Dzurak, A. Morello, M. Y. Simmons, L. C. L. Hollenberg, G. Klimeck, S. Rogge, S. N. Coppersmith, and M. A. Eriksson, *Silicon quantum electronics,* Reviews of Modern Physics **85**, 961 (2013).

[4] L. M. K. Vandersypen, H. Bluhm, J. S. Clarke, A. S. Dzurak, R. Ishihara, A. Morello, D. J. Reilly, L. R. Schreiber, and M. Veldhorst, *Interfacing spin qubits in quantum dots and donors—hot, dense, and coherent,* npj Quantum Information **3**, 34 (2017).

[5] M. Veldhorst, J. Hwang, C. Yang, A. Leenstra, B. de Ronde, J. Dehollain, J. Muhonen, F. Hudson, K. M. Itoh, A. Morello, *et al., An addressable quantum dot qubit with fault-tolerant control-fidelity,* Nature Nanotechnology **9**, 981 (2014).

[6] K. M. Itoh and H. Watanabe, *Isotope engineering of silicon and diamond for quantum computing and sensing applications,* MRS Commun. **4**, 143 (2014).

[7] J. Yoneda, K. Takeda, T. Otsuka, T. Nakajima, M. R. Delbecq, G. Allison, T. Honda, T. Kodera, S. Oda, Y. Hoshi, *et al.*, *A quantum-dot spin qubit with coherence limited by charge noise and fidelity higher than 99.9%,* Nature Nanotechnology **13**, 102 (2018).

[8] C. Yang, K. Chan, R. Harper, W. Huang, T. Evans, J. Hwang, B. Hensen, A. Laucht, T. Tanttu, F. Hudson, *et al.*, *Silicon qubit fidelities approaching incoherent noise limits via pulse engineering,* Nature Electronics **2**, 151 (2019).

[9] M. Veldhorst, C. H. Yang, J. C. C. Hwang, W. Huang, J. P. Dehollain, J. T. Muhonen, S. Simmons, A. Laucht, F. E. Hudson, K. M. Itoh, A. Morello, and A. S. Dzurak, *A two-qubit logic gate in silicon,* Nature **526**, 410 (2015).

[10] D. M. Zajac, A. J. Sigillito, M. Russ, F. Borjans, J. M. Taylor, G. Burkard, and J. R. Petta, *Resonantly driven CNOT gate for electron spins,* Science **359**, 439 (2018).

[11] T. F. Watson, S. G. J. Philips, E. Kawakami, D. R. Ward, P. Scarlino, M. Veldhorst, D. E. Savage, M. G. Lagally, M. Friesen, S. N. Coppersmith, M. A. Eriksson, and L. M. K. Vandersypen, *A programmable two-qubit quantum processor in silicon,* Nature **555**, 633 (2018).

[12] W. Huang, C. Yang, K. Chan, T. Tanttu, B. Hensen, R. Leon, M. Fogarty, J. Hwang, F. Hudson, K. M. Itoh, *et al.*, *Fidelity benchmarks for two-qubit gates in silicon,* Nature **569**, 532 (2019).

[13] A. G. Fowler, M. Mariantoni, J. M. Martinis, and A. N. Cleland, *Surface codes: Towards practical large-scale quantum computation,* Physical Review A **86**, 032324 (2012).

[14] D. P. Franke, J. S. Clarke, L. M. Vandersypen, and M. Veldhorst, *Rent's rule and extensibility in quantum computing,* Microprocessors and Microsystems **67**, 1 (2019).

[15] M. Veldhorst, H. G. J. Eenink, C. H. Yang, and A. S. Dzurak, *Silicon CMOS architecture for a spin-based quantum computer,* Nature Communication **8**, 1766 (2017).

[16] R. Li, L. Petit, D. P. Franke, J. P. Dehollain, J. Helsen, M. Steudtner, N. K. Thomas, Z. R. Yoscovits, K. J. Singh, S. Wehner, *et al.*, *A crossbar network for silicon quantum dot qubits,* Science Advances **4**, eaar3960 (2018).

[17] L. Petit, J. Boter, H. Eenink, G. Droulers, M. Tagliaferri, R. Li, D. Franke, K. Singh, J. Clarke, R. Schouten, *et al.*, *Spin lifetime and charge noise in hot silicon quantum dot qubits,* Physical Review Letters **121**, 076801 (2018).

[18] A. Morello, J. J. Pla, F. A. Zwanenburg, K. W. Chan, K. Y. Tan, H. Huebl, M. Möttönen, C. D. Nugroho, C. Yang, J. A. v. Donkelaar, A. D. C. Alves, D. N. Jamieson, C. C. Escott, L. C. L. Hollenberg, R. G. Clark, and A. S. Dzurak, *Single-shot readout of an electron spin in silicon,* Nature **467**, 687 (2010).

[19] C. H. Yang, W. H. Lim, F. A. Zwanenburg, and A. S. Dzurak, *Dynamically controlled charge sensing of a few-electron silicon quantum dot,* AIP Advances **1**, 042111 (2011).

[20] W. Lawrie, H. Eenink, N. Hendrickx, J. Boter, L. Petit, S. Amitonov, M. Lodari, B. Paquelet Wuetz, C. Volk, S. Philips, *et al.*, *Quantum dot arrays in silicon and germanium,* Applied Physics Letters **116**, 080501 (2020).

[21] S. J. Angus, A. J. Ferguson, A. S. Dzurak, and R. G. Clark, *Gate-defined quantum dots in intrinsic silicon,* Nano letters **7**, 2051 (2007).

[22] J. Elzerman, R. Hanson, L. W. Van Beveren, B. Witkamp, L. Vandersypen, and L. P. Kouwenhoven, *Single-shot read-out of an individual electron spin in a quantum dot,* Nature **430**, 431 (2004).

[23] M. Urdampilleta, D. J. Niegemann, E. Chanrion, B. Jadot, C. Spence, P.-A. Mortemousque, L. Hutin, B. Bertrand, S. Barraud, R. Maurand, *et al.*, *Gate-based high fidelity spin read-out in a cmos device,* Nature Nanotechnology **14**, 737 (2019).

[24] C. H. Yang, A. Rossi, R. Ruskov, N. S. Lai, F. A. Mohiyaddin, S. Lee, C. Tahan, G. Klimeck, A. Morello, and A. S. Dzurak, *Spin-valley lifetimes in a silicon quantum dot with tunable valley splitting,* Nature Communications **4**, 2069 (2013).

[25] R. Ruskov, M. Veldhorst, A. S. Dzurak, and C. Tahan, *Electron g-factor of valley states in realistic silicon quantum dots,* Physical Review B **98**, 245424 (2018).

[26] C. H. Yang, R. Leon, J. Hwang, A. Saraiva, T. Tanttu, W. Huang, J. C. Lemyre, K. W. Chan, K. Tan, F. E. Hudson, *et al.*, *Operation of a silicon quantum processor unit cell above one kelvin,* Nature **580**, 350 (2020).

[27] E. Magesan, J. M. Gambetta, and J. Emerson, *Scalable and robust randomized benchmarking of quantum processes,* Physical Review Letters **106**, 180504 (2011).

[28] M. Reed, B. Maune, R. Andrews, M. Borselli, K. Eng, M. Jura, A. Kiselev, T. Ladd, S. Merkel, I. Milosavljevic, *et al.*, *Reduced sensitivity to charge noise in semiconductor spin qubits via symmetric operation,* Physical Review Letters **116**, 110402 (2016).

[29] F. Martins, F. K. Malinowski, P. D. Nissen, E. Barnes, S. Fallahi, G. C. Gardner, M. J. Manfra, C. M. Marcus, and F. Kuemmeth, *Noise Suppression Using Symmetric Exchange Gates in Spin Qubits,* Physical Review Letters **116**, 116801 (2016).

[30] G. Ithier, E. Collin, P. Joyez, P. Meeson, D. Vion, D. Esteve, F. Chiarello, A. Shnirman, Y. Makhlin, J. Schriefl, *et al.*, *Decoherence in a superconducting quantum bit circuit,* Physical Review B **72**, 134519 (2005).

[31] U. Güngördü and J. Kestner, *Pulse sequence designed for robust c-phase gates in simos and si/sige double quantum dots,* Physical Review B **98**, 165301 (2018).

[32] B. M. Freeman, J. S. Schoenfield, and H. Jiang, *Comparison of low frequency charge noise in identically patterned si/sio2 and si/sige quantum dots,* Applied Physics Letters **108**, 253108 (2016).

[33] E. Paladino, Y. Galperin, G. Falci, and B. Altshuler, *1/f noise: Implications for solid-state quantum information,* Reviews of Modern Physics **86**, 361 (2014).

[34] E. J. Connors, J. Nelson, H. Qiao, L. F. Edge, and J. M. Nichol, *Low-frequency charge noise in si/sige quantum dots,* Physical Review B **100**, 165305 (2019).

[35] F. Beaudoin and W. A. Coish, *Microscopic models for charge-noise-induced dephasing of solid-state qubits,* Physical Review B **91**, 165432 (2015).

6

HIGH-FIDELITY TWO-QUBIT GATES IN SILICON ABOVE ONE KELVIN

Engineering two-qubit interactions is a central aspect in the construction of a quantum computer and having at disposal a wide set of high-fidelity two-qubit gates is crucial to successfully implement quantum algorithms, error correction codes and long-range qubit couplings. While the previous chapter contains the demonstration of a universal gate set for silicon qubits at temperatures above one Kelvin, the fidelity of the two-qubit CROT gate is limited to 86%. In this chapter, we investigate new native two-qubit gates and discuss novel sequences to optimize their fidelities. In particular, we show the implementation of a CPHASE and a SWAP gate, in addition to the CROT, with adiabatic, diabatic and composite sequences to optimize the qubit control fidelity and the gate time. The gate performances are analyzed trough simulations and we predict, on the same device operating above one Kelvin, two-qubit gate fidelities above 99%.

Parts of this chapter have been published as a preprint in arXiv, arXiv-2007.09034 (2020) [1].

6.1. TWO-QUBIT GATES FOR ELECTRON SPINS

Two-qubit gates are at the heart of quantum information science, as they may be used to create entangled states with a complexity beyond what is classically simulatable [2], and ultimately may enable the execution of practically relevant quantum algorithms [3]. Optimizing two-qubit gates is therefore a central aspect across all qubit platforms [4]. In quantum dot systems, two-qubit gates can be naturally implemented using the exchange interaction between spin qubits in neighbouring quantum dots [5]. Pulsing the interaction drives SWAP oscillations when the exchange energy is much larger than the Zeeman energy difference of the qubits [5, 6], while it results in CPHASE oscillations when the Zeeman energy difference is much larger than the exchange energy [7]. Single-qubit gates need also to be implemented to access the full two-qubit Hilbert space, and this requires distinguishability between the qubits. This is commonly obtained through the spin-orbit coupling [8] or by integrating nanomagnets [9, 10], causing significant Zeeman energy differences. Realizing a high-fidelity SWAP-gate in this scenario would require extremely large values of exchange interaction. For this reason, the CPHASE operation has been the native gate in experimental demonstrations of two-qubit logic when the exchange interaction is pulsed [11–13]. An alternative implementation of two-qubit logic can be realized by driven rotations, which become state dependent in the presence of exchange interaction. This has been used to realize CROT [14–17] and resonant SWAP gates [18].

While universal quantum logic can be obtained by combinations of single- and two-qubit operations [19], the ability to directly execute a multitude of two-qubit gates would reduce the number of operations required to execute quantum algorithms. Here, we take this step and investigate on the same device the implementation of the CROT, SWAP, and CPHASE, which are all essential gates in applications ranging from quantum error correction to long-distance qubit connectivity. We furthermore focus on the optimal implementation of these two-qubit gates and find that in particular the CPHASE and the SWAP can be executed with high-fidelity and in short time scales. Moreover, we demonstrate these operations at temperatures exceeding one Kelvin. The cooling power at these elevated temperatures is much larger and thereby more compatible with the operation of classical electronics, such that quantum integrated circuits based on standard semiconductor technology become feasible [20–22].

The experimental two-qubit system is the same device described in the previous chapter, and here we recall the main characteristics. Qubits Q1 and Q2 are defined with $N_{\mathrm{Q1}} = 5$ and $N_{\mathrm{Q2}} = 1$, where N is the charge occupancy. Spin readout is performed at the (5,1)-(4,2) charge anticrossing, where the $|{\downarrow\uparrow}\rangle$ tunnels to the singlet (4,2) charge state, while the other spin states are blocked because of the Pauli exclusion principle. By using an adiabatic pulse from the (4,2) to the (5,1) region, we initialize the system in the $|{\downarrow\uparrow}\rangle$ state. Because of the limited sensitivity of the single-electron-transistor (SET) that we use for charge readout, we average the single-shot readout traces and subtract a reference signal. We therefore obtain a current signal, proportional to the probability to have a blocked state. We note that the readout fidelity can be further improved, even at these higher temperatures [23], but here we focus on the coherent control. We perform spin manipulation via electron spin resonance (ESR) using an on-chip aluminum microwave antenna. All measurements have been performed in a dilution refrigerator at a temper-

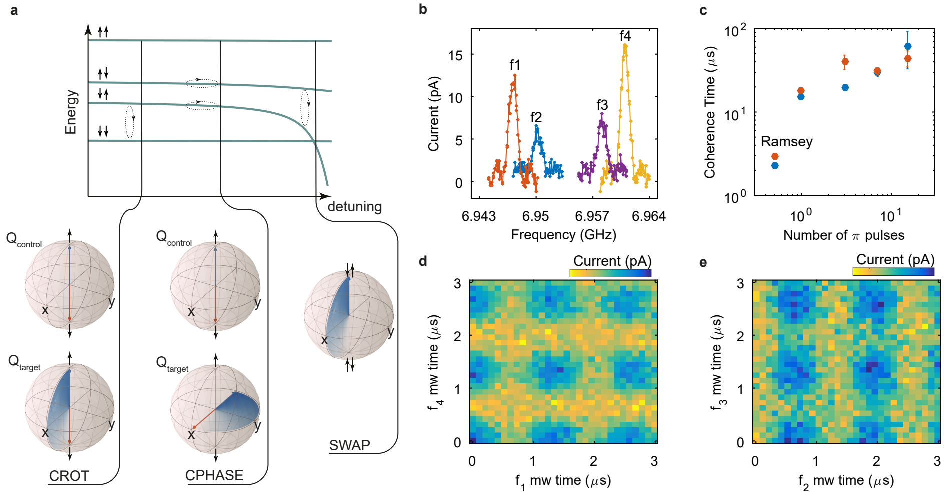

Figure 6.1: **a** The energy diagram displays the four electron spin states as a function of ϵ. We exploit both driven rotations and pulsed exchange for coherent control. Controlled rotations (CROTs) can in principle be executed at all points where $J \neq 0$, given that gate times are appropriately set. CPHASE gates are conveniently executed when the exchange interaction is much smaller than the Zeeman energy difference between the qubits, while SWAP oscillations can be realized when the exchange interaction is much larger. **b** Using ESR control we find the four resonance frequencies of the two-qubit system. Here, the exchange interaction is tuned to 3 MHz. **c** Coherence times as a function of the number of refocusing π pulses. Here, the exchange is set to 2 MHz. The plot includes the dephasing times measured through a Ramsey experiment to allow comparison. **d-e** Realization of CROT operations. Rabi oscillations of the target qubit are controlled by the spin state of the control qubit. We find controlled rotations on all the four resonance frequencies f_1, f_2, f_3, f_4.

ature of $T_{\text{fridge}} = 1.05\,\text{K}$ and with an external magnetic field of $B_{\text{ext}} = 250\,\text{mT}$.

6.2. CROT GATE

As discussed in the previous chapter, we control the exchange interaction J via the detuning ϵ between the two quantum dots and we measure couplings from $J = 2\,\text{MHz}$ up to $J = 45\,\text{MHz}$, as measured from the frequency of SWAP oscillations and the shift in energy of the qubit resonance frequencies. By fitting the exchange spectrum we extract a Zeeman energy difference between the two qubits $\Delta E_Z = 11\,\text{MHz}$. The fitting suggests a negligible dependence of ΔE_Z on detuning, further supported by the small magnetic field applied and the absence of external magnetic gradients. Figure 6.1b shows the four resonance frequencies of the two-qubit system when $J = 3\,\text{MHz}$. At this value of exchange interaction we tune the π-rotation times to be $t_{\text{CROT}} = 660\,\text{ns}$ such that we synchronize the Rabi oscillations of the target transition with the closest off-resonant transition in order to suppress crosstalk [24]. From Ramsey experiments on frequencies f_1 and f_4 we measure dephasing times $T^*_{2,\text{Q1}} = 2.3\,\mu\text{s}$ and $T^*_{2,\text{Q2}} = 2.9\,\mu\text{s}$. The Carr-Purcell-Meiboom-Gill (CPMG) pulse sequence can extend the coherence times, by filtering out the low frequency noise. As shown in Fig. 6.1c, we measure a maximum $T_{2,\text{Q1}} = 63\,\mu\text{s}$ and $T_{2,\text{Q2}} = 44\,\mu\text{s}$ when 15 refocusing pulses are applied, setting new benchmarks for the coherence time of quantum dot spin qubits at temperatures above one Kelvin.

When the exchange interaction is set to a non-zero value, it is possible to realize the CROT via driven rotations since the resonance frequency of one qubit depends on the state of the other qubit. This CROT gate is a universal two-qubit gate and equivalent to a CNOT gate up to single qubit phases [17]. Figures 6.1d-e show controlled rotations by setting both configurations of target and control qubits.

6.3. CPHASE GATE

An alternative way to achieve a universal gate set is through the implementation of the CPHASE gate. Moving in detuning energy toward the (5,1)-(4,2) charge anticrossing lowers the energy of the antiparallel $|\downarrow\uparrow\rangle$ and $|\uparrow\downarrow\rangle$ states with respect to the parallel $|\downarrow\downarrow\rangle$ and $|\uparrow\uparrow\rangle$ spin states. Therefore, pulsing the detuning for a time t results in a phase gate on the target qubit conditional on the spin state of the control qubit. When the total phase $\phi = \phi_{|\downarrow\uparrow\rangle} + \phi_{|\uparrow\downarrow\rangle} = (2n+1)\pi$ with n integer, a CPHASE gate is realized [7]. A high-fidelity implementation of such a gate requires a Zeeman energy difference between the two qubits much larger than the exchange interaction, in order to suppress the evolution of the exchange gate [5]. This condition is conveniently met in devices with micromagnets [12–14], where the CPHASE is the most natural choice as native two-qubit gate.

In our system, ΔE_z is comparable in magnitude to the accessible J, due to the small B_ext applied. This means that a detuning pulse will also cause the $|\downarrow\uparrow\rangle$ and $|\uparrow\downarrow\rangle$ states to undergo SWAP rotations. While these rotations occur along a tilted angle due to the non-zero ΔE_z, they can still reduce the fidelity of the CPHASE gate. In order to avoid unwanted SWAP rotations we implement an adiabatic detuning pulse, by ramping ϵ to the desired value instead of changing it instantaneously (see schematic in Fig. 6.3a). In this way, a high-fidelity CPHASE gate can still be realized with an arbitrarily small ΔE_z at the cost of a longer gate time. In Fig. 6.2a and b we change the duration of a detuning pulse in between a Ramsey-like experiment on Q1, with and without a π pulse applied to Q2. The frequency of the oscillations of Q1 depends strongly on the spin state of Q2, thereby demonstrating a controlled phase operation. Because of the finite Zeeman energy difference, the antiparallel $|\downarrow\uparrow\rangle$ state shifts significantly more in energy than the $|\uparrow\downarrow\rangle$ state. Consequently, the oscillations in Fig. 6.2a are significantly faster than in Fig. 6.2b. Similarly, the decay time in Fig. 6.2b is significantly longer than in Fig. 6.2a because of the lower sensitivity to electrical noise. In Fig. 6.2c the pulse time is calibrated such that the total phase $\phi = 3\pi$. We measure this in a Ramsey-like experiment where we probe the phase acquired by the target qubit for different control qubit states. From Fig. 6.2c we can observe that the resulting oscillations are nicely out-of-phase, which demonstrates the CPHASE gate. We achieve a gate time $t_\mathrm{CPHASE} = 152\,\mathrm{ns}$, which is mostly limited by the adiabatic ramps which take $t_\mathrm{r} = 60\,\mathrm{ns}$. From a comparison with simulations we find that the contribution of both ramps to the total phase ϕ is approximately 1.7π.

This gate time can be significantly sped up with the implementation of a geometric CPHASE gate, that does not require adiabaticity [25]. For the implementation of this gate we synchronize the unwanted exchange oscillations with the total gate duration, i.e. our gate performs a CPHASE evolution while the exchange oscillations performs a complete cycle. For a perfectly diabatic pulse the condition for the exchange interaction is:

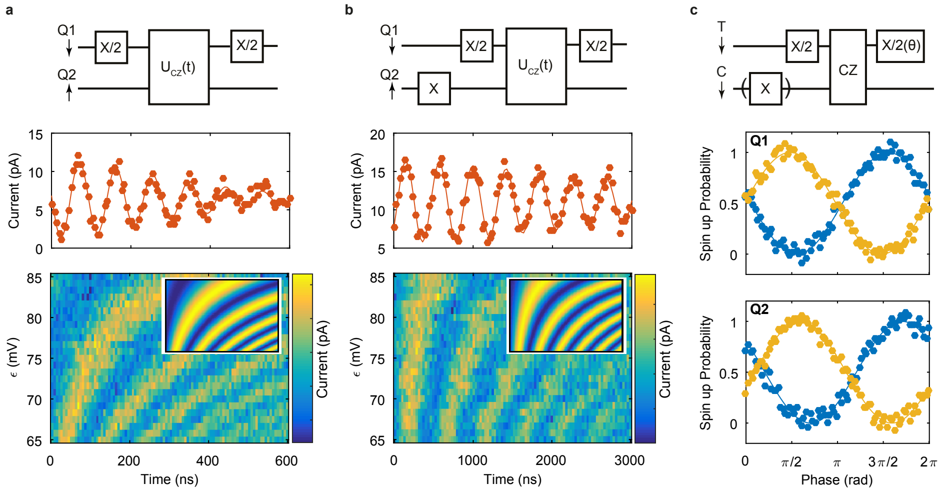

Figure 6.2: **a,b** Conditional phase oscillations by adiabatically pulsing the detuning energy ϵ to increase the exchange interaction J, measured using the quantum circuit depicted in the top panels. The antiparallel spin states acquire a phase with respect to the parallel states, resulting in coherent oscillations as a function of the duration of the detuning pulse. At smaller detuning values, the exchange interaction increases resulting in faster oscillations. Due to the exchange interaction, the energy difference $E_{\downarrow\uparrow} - E_{\downarrow\downarrow}$ (measured in **a**) is smaller than $E_{\uparrow\uparrow} - E_{\uparrow\downarrow}$ (measured in **b**), resulting in an acquired phase on the target qubit that is dependent on the state of the control qubit. **c-d** Demonstration of a CPHASE gate. The adiabatic detuning pulse is tuned such that the antiparallel spin states acquire a total phase of 3π. The exchanged is increased to J = 27.5 MHz using a ramp t_r = 60 ns and the total gate time t_{CPHASE} = 152 ns. To show the evolution of the spin states, the readout current has been converted to a normalized spin-up probability. The phase offset in **d** is due to finite miscalibrations of the single-qubit gates used in the sequence.

$$J = (4J_{\mathrm{res}} + \sqrt{3\Delta E_{\mathrm{z}}^2 + 4J_{\mathrm{res}}^2})/3, \tag{6.1}$$

where J_{res} is the residual exchange interaction at the point where we perform CROT gates.

Figures 6.3b and c show the experimental implementation of the geometric CPHASE gate. We sweep the amplitude of the detuning pulse and monitor the spin state probabilities (see Sec. 6.6) during exchange oscillations, and the total phase acquired by the antiparallel spin states. We notice that, when $\epsilon \approx 68\,\mathrm{mV}$, the antiparallel spin states execute a 2π rotation, while acquiring a total phase shift of π. At this value of detuning we measure $J \approx 10\,\mathrm{MHz}$ and therefore in agreement with Eq.6.1. The total gate time is reduced here to $t_{\mathrm{CPHASE}} = 67\,\mathrm{ns}$.

6.4. SWAP GATE

We now turn to the implementation of a SWAP gate, the originally proposed quantum gate for quantum dots [5]. Despite the experimental demonstration of exchange oscillations [6, 26, 27], its implementation together with single-qubit gates is rather challenging because of the requirement of a negligible Zeeman difference between the qubits. In the

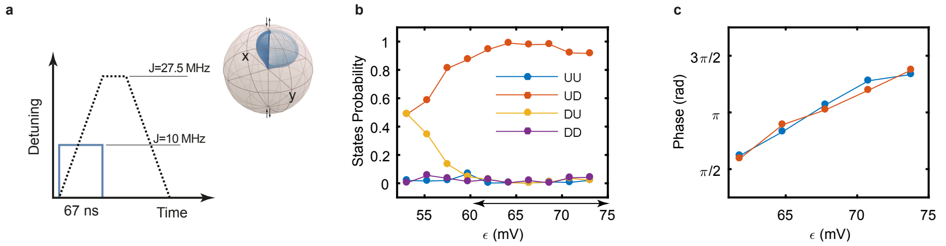

Figure 6.3: **a** The schematic shows the pulse sequences for an adiabatic (dashed black) and a diabatic (solid blue) CPHASE. **b** Four spin state probabilities as a function of the duration of a diabatic detuning pulse. Due to the finite Zeeman difference ($\Delta E_\mathrm{Z} = 11\,\mathrm{MHz}$) SWAP-interactions are not negligible when the detuning is pulsed diabatically. However, the exchange can be tuned such that the states undergo rotations of 2π. **c** Optimization of the CPHASE by tuning ϵ and measuring both the state probability and the phase. A diabatic CPHASE is obtained for $t_\mathrm{CPHASE} = 67$ ns.

following we will discuss a novel protocol that can overcome this problem and allow for a high-fidelity SWAP gate, even in the presence of a finite ΔE_Z.

In order to observe SWAP oscillations, we implement a sequence where we initialize in the $|{\downarrow\uparrow}\rangle$ state and pulse ϵ for a time t. Clear exchange oscillations between the $|{\downarrow\uparrow}\rangle$ and the $|{\uparrow\downarrow}\rangle$ state are visible when the detuning pulse is diabatic (see Fig. 6.4a), where the oscillation frequency is $f_\mathrm{SWAP} = \sqrt{J^2 + \Delta E_\mathrm{Z}^2}$. As we make the pulse more adiabatic by ramping ϵ, the oscillations disappear and the regime becomes suitable for a CPHASE implementation as discussed before. Even when the detuning pulse is perfectly diabatic, we do not obtain a perfect SWAP due to the finite ΔE_Z. Instead, the spin states rotate in the Bloch sphere around the tilted axis of rotation $\boldsymbol{r} = (J, 0, \Delta E_\mathrm{Z})^T$, similar to what happens for off-resonant driving. Figure 6.4c and d show that when starting in the $|{\downarrow\uparrow}\rangle$ state, a maximum $|{\uparrow\downarrow}\rangle$ state probability of 64% is obtained in $t_\mathrm{SWAP} = 18\,\mathrm{ns}$, which is in agreement with our simulated predictions (see Sec. 6.5).

Composite pulse sequences [28] can correct for the tilted axis of rotation. It is possible to achieve full population transfer with an exchange sequence consisting of alternating diabatic and adiabatic exchange pulses. The corresponding time evolution operators in the odd parity subspace are:

$$U_\mathrm{r} = e^{i\Phi_\mathrm{r}} e^{i\theta_\mathrm{r} \boldsymbol{r}\cdot\boldsymbol{\sigma}} \tag{6.2}$$

$$U_\mathrm{z} = e^{i\Phi_\mathrm{z}} e^{i\theta_\mathrm{z} \hat{Z}} \tag{6.3}$$

for a diabatic and an adiabatic pulse respectively. Here $\boldsymbol{\sigma} = (\hat{X}, \hat{Y}, \hat{Z})$ is the vector consisting of the Pauli matrices, $\Phi_\mathrm{r,z} = J t_\mathrm{r,z}/2$ the accumulated entangling phase during the pulse, and $\theta_\mathrm{r,z} = t_\mathrm{r,z}\sqrt{J^2 + \Delta E_\mathrm{Z}^2}/2$ the angle of rotation. The condition for a SWAP gate is $U_\mathrm{tot} = U_\mathrm{r} U_\mathrm{z} U_\mathrm{r} U_{\mathrm{z}_2} U_{\mathrm{r}_2} \cdots \equiv \hat{X}$. The number of necessary pulses depends on the angle of rotation; obviously a minimal pulse sequence requires $|\Delta E_\mathrm{Z}| \leq J$. Furthermore, it is essential to include the global phase which corresponds to a conditional phase evolution in the full two-qubit space and needs to vanish when implementing a SWAP gate.

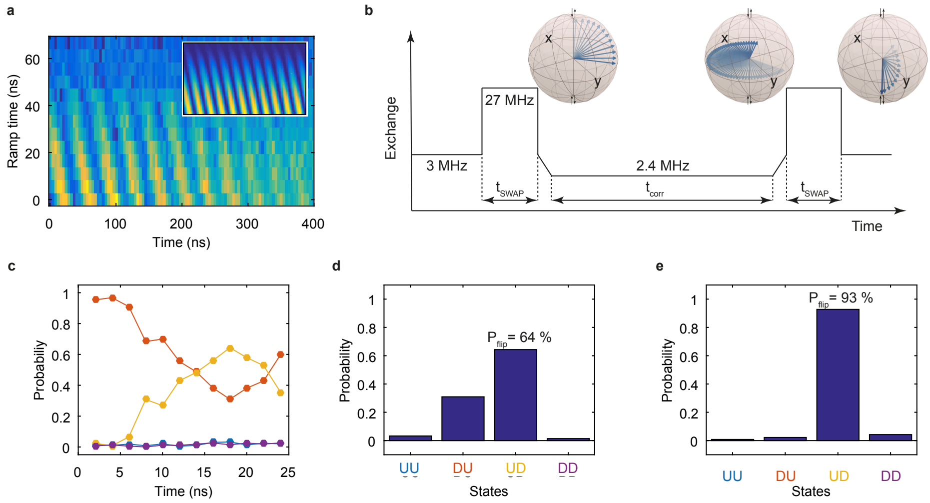

Figure 6.4: **a** SWAP oscillations as a function of the ramp time of a detuning pulse. When the pulsing becomes adiabatic with respect to variations in J, the exchange oscillations are suppressed. In order to maximize the readout signal we project the $|\uparrow\downarrow\rangle$ to the $|\uparrow\uparrow\rangle$ with a π pulse on f_2. **b** Pulse sequence of the composite SWAP gate to correct for errors coming from the finite Zeeman energy difference. The Bloch spheres on top show the time evolution when starting in the $|\downarrow\uparrow\rangle$ state, with the Bloch vector depicted in nanosecond time steps. We first diabatically pulse the exchange to J = 27 MHz, in order to bring the state on the equator of the singlet-triplet Bloch sphere. Then we correct for the phase offset with an adiabatic exchange pulse to J = 2.4 MHz. We complete the state flip with another exchange pulse to J = 27 MHz. **c,d** Probabilities of the four spin states as a function of the SWAP interaction time. The states $|\uparrow\uparrow\rangle$ and $|\downarrow\downarrow\rangle$ are not affected, while the states $|\downarrow\uparrow\rangle$ and $|\uparrow\downarrow\rangle$ oscillate. Due to the finite Zeeman difference we achieve a maximum $|\uparrow\downarrow\rangle$ state probability of 64 % for t_{SWAP} = 18 ns. The exchange interaction is set to J = 27 MHz. **e** Spin state probability after executing the composite SWAP sequence starting from the initial state $|\downarrow\uparrow\rangle$. Compared to a simple detuning pulse as shown in **d** we find a clear improvement in the spin flip SWAP probability.

This protocol is highly versatile and can also produce maximally entangling gates, i.e., $\sqrt{\mathrm{SWAP}}$ if $U_{\mathrm{tot}} \equiv i\hat{X}/2$ and iSWAP for $U_{\mathrm{tot}} \equiv i\hat{X}$.

A possible minimal length solution for a SWAP gate is sketched in Fig. 6.4b and the trajectory of the qubit state is seen in the inset. In the experiment, we calibrate the exchange interaction at all stages of the pulse, fix the time of the diabatic pulses to 12 ns and sweep the length of the adiabatic pulse t_{corr} in order to find the best point. We find an optimal t_{corr} = 62 ns and the four spin state probabilities for a total pulse duration t_{SWAP} = 88 ns are plotted in Fig. 6.4e. The SWAP probability exceeds 90%, where the remaining error is dominated by miscalibrations, inaccuracies in the gates needed to reconstruct the spin state probabilities, and state-preparation-and-measurement (SPAM) errors.

6.5. FIDELITY SIMULATIONS

For all the two-qubit gates we obtain the fidelities by numerically solving the time-dependent Schrodinger equation $i\hbar\dot{\Psi}(t) = H(t)\Psi(t)$ using a step size t = 50 ps. We have confirmed that a faster sampling rate does not change the simulation results. In order to resemble

a

	Gate time (ns)	F_{ideal}(%)	F_{noise}(%)
CROT	660	99.4	89.0
CPHASE	152	99.9	97.8
Diabatic CPHASE	67	99.9	99.4
SWAP	19	84.3	84.2
Composite SWAP	89	99.9	99.4

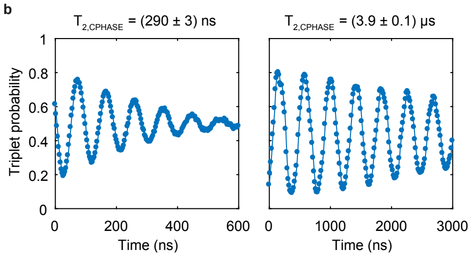

Figure 6.5: Gate times and simulated fidelities for all the two-qubit gates discussed in the main text. We note that the CROT in this context describes a conditional π-flip for a better comparison. We find agreement with fidelities from previous experiments [17], confirming that the simulated noise is an accurate estimate of the experimental noise source. Further improvement in the fidelities of the CROT and the CPHASE may be obtained by incorporating pulse shaping [29–33]. **b** Simulated data for the sequence used in Fig. 6.2a and b of the main text.

real setups and to avoid sampling problems we filter all time-dependent signals using a high-pass filter with a cut-off frequency of 300 MHz. All simulations are performed using the Heisenberg Hamiltonian

$$H(t) = \Delta E_z(\epsilon)(S_{z,1} - S_{z,2})/2 + J(\epsilon)(\boldsymbol{S}_1 \cdot \boldsymbol{S}_2 - 1/4), \tag{6.4}$$

where $\boldsymbol{S}_i = (S_{x,i}, S_{y,i}, S_{z,i})$ is the spin operator of the electron in quantum dot i. The parameters $\Delta E_z(\epsilon)$ and $J(\epsilon)$ are the qubit frequency difference and the exchange interaction which both depend on the detuning ϵ.

To include the effect of decoherence we add stochastic fluctuations of the detuning, $\epsilon \to \epsilon + \delta\epsilon(t)$ to each run of the time evolution and average the resulting density matrix. To emulate the effect of $1/f$ charge noise we generate time-dependent fluctuations $\delta\epsilon(t)$ following a $S(\omega) = A_\epsilon/f$ spectral density using the method described in Ref. [34, 35]. The amplitude of the noise A_ϵ is set such that it reproduces the decay time of the exchange oscillations measured experimentally. Using the same value of noise we then simulate the Ramsey sequences of Fig. 6.2a and b of the main text and we show the results in Figure 6.5b. The decay times that we extract are in agreement with the measured decays $T_{2,\text{CPHASE}\downarrow} = (397 \pm 24)$ ns and $T_{2,\text{CPHASE}\uparrow} = (3.9 \pm 0.6)$ μs.

Table 6.5a shows the fidelities associated with the two-qubit gates CROT, CPHASE, and SWAP. Here, F_{ideal} represents the simulated fidelities taking into account the relevant parameters, but neglecting any decoherence. We find $F_{\text{ideal}} > 99\%$ for all gates except the SWAP, which is limited in fidelity by the finite ΔE_z. We have also modelled the decoherence assuming $1/f$ noise as the main noise source. By fitting the experimental data in Fig 6.2a and b, we conclude that our model is able to reproduce the decoherence with good agreement. Based on these simulations we determine F_{noise}. The fidelity of the CROT and the CPHASE gate are significantly affected by the noise, due to the relatively long gate times, and we find that the predicted CROT fidelity $F_{\text{noise}} = 89$ % is close to the experimentally measured fidelity $F = 86$ % [17]. The SWAP, diabatic CPHASE and composite SWAP are less affected by the noise and in particular we predict that both the diabatic CPHASE and composite SWAP can be executed with fidelities above 99 %.

6.6. RECONSTRUCTION OF THE SPIN STATE PROBABILITIES

In order to readout the spin states we average all single-shot readout traces and subtract a reference sequence where no gates are performed. The corresponding readout signal is therefore a current that is proportional to the probability of having a blocked state. In order to be able to reconstruct the four probability amplitudes $|A|^2, |B|^2, |C|^2, |D|^2$ of a generic state $\psi = A|\uparrow\uparrow\rangle + B|\uparrow\downarrow\rangle + C|\downarrow\uparrow\rangle + D|\downarrow\downarrow\rangle$ it is necessary to know the current signal of the four spin states $\{\alpha \longrightarrow |\downarrow\uparrow\rangle, \beta \longrightarrow |\uparrow\uparrow\rangle, \gamma \longrightarrow |\downarrow\downarrow\rangle, \delta \longrightarrow |\uparrow\downarrow\rangle\}$. By initializing the $|\downarrow\uparrow\rangle$ state and then using the four frequencies $\mathrm{f}_1, \mathrm{f}_2, \mathrm{f}_3, \mathrm{f}_4$ we can reach all spin states and therefore measure the parameters $\alpha, \beta, \gamma, \delta$.

Once we measure the current signals for all spin states we need to gain information about the state ψ. We therefore apply the following sequences and measure the parameters $\phi_0, \phi_1, \phi_2, \phi_3$:

- Sequence: prepare state ψ then measure. We measure a current ϕ_0 equal to:

$$\phi_0 = |A|^2\beta + |B|^2\delta + |C|^2\alpha + |D|^2\gamma \tag{6.5}$$

- Sequence: prepare state ψ, π pulse on f4 then measure. We measure a current ϕ_1 equal to:

$$\phi_1 = |C|^2\beta + |B|^2\delta + |A|^2\alpha + |D|^2\gamma \tag{6.6}$$

- Sequence: prepare state ψ, π pulse on f1 then measure. We measure a current ϕ_2 equal to:

$$\phi_2 = |A|^2\beta + |B|^2\delta + |D|^2\alpha + |C|^2\gamma \tag{6.7}$$

- Sequence: prepare state ψ, π pulse on f2, π pulse on f4 then measure. We measure a current ϕ_3 equal to:

$$\phi_3 = |C|^2\beta + |A|^2\delta + |B|^2\alpha + |D|^2\gamma \tag{6.8}$$

Therefore we have the following system of equations, that we want to solve for the probabilities $|A|^2, |B|^2, |C|^2, |D|^2$:

$$\begin{bmatrix} \beta & \delta & \alpha & \gamma \\ \alpha & \delta & \beta & \gamma \\ \beta & \delta & \gamma & \alpha \\ \delta & \alpha & \beta & \gamma \end{bmatrix} \cdot \begin{bmatrix} |A|^2 \\ |B|^2 \\ |C|^2 \\ |D|^2 \end{bmatrix} = \begin{bmatrix} \phi_0 \\ \phi_1 \\ \phi_2 \\ \phi_3 \end{bmatrix} \tag{6.9}$$

We solve the system by inverting the matrix:

$$\begin{bmatrix} |A|^2 \\ |B|^2 \\ |C|^2 \\ |D|^2 \end{bmatrix} = \begin{bmatrix} \beta & \delta & \alpha & \gamma \\ \alpha & \delta & \beta & \gamma \\ \beta & \delta & \gamma & \alpha \\ \delta & \alpha & \beta & \gamma \end{bmatrix}^{-1} \cdot \begin{bmatrix} \phi_0 \\ \phi_1 \\ \phi_2 \\ \phi_3 \end{bmatrix} \tag{6.10}$$

Finally the resulting amplitudes are normalized. The extracted probabilities correspond to the diagonal parts of the density matrix ρ which may violate $\sum_i \rho_{ii} = 1$ due to measurement and gate errors. In order to ensure the physicality of our results we perform a maximum-likelihood estimation [36] using the diagonal elements of the density matrix.

REFERENCES

[1] L. Petit, M. Russ, H. Eenink, W. Lawrie, J. Clarke, L. Vandersypen, and M. Veldhorst, *High-fidelity two-qubit gates in silicon above one kelvin,* arXiv preprint arXiv:2007.09034 (2020).

[2] F. Arute, K. Arya, R. Babbush, D. Bacon, J. C. Bardin, R. Barends, R. Biswas, S. Boixo, F. G. Brandao, D. A. Buell, *et al.*, *Quantum supremacy using a programmable superconducting processor,* Nature **574**, 505 (2019).

[3] M. Reiher, N. Wiebe, K. M. Svore, D. Wecker, and M. Troyer, *Elucidating reaction mechanisms on quantum computers,* Proceedings of the National Academy of Sciences **114**, 7555 (2017).

[4] T. D. Ladd, F. Jelezko, R. Laflamme, Y. Nakamura, C. Monroe, and J. L. O'Brien, *Quantum computers,* Nature **464**, 45 (2010).

[5] D. Loss and D. P. DiVincenzo, *Quantum computation with quantum dots,* Physical Review A **57**, 120 (1998).

[6] J. R. Petta, A. C. Johnson, J. M. Taylor, E. A. Laird, A. Yacoby, M. D. Lukin, C. M. Marcus, M. P. Hanson, and A. C. Gossard, *Coherent Manipulation of Coupled Electron Spins in Semiconductor Quantum Dots,* Science **309**, 2180 (2005).

[7] T. Meunier, V. Calado, and L. Vandersypen, *Efficient controlled-phase gate for single-spin qubits in quantum dots,* Physical Review B **83**, 121403 (2011).

[8] M. Veldhorst, J. Hwang, C. Yang, A. Leenstra, B. de Ronde, J. Dehollain, J. Muhonen, F. Hudson, K. M. Itoh, A. Morello, *et al.*, *An addressable quantum dot qubit with fault-tolerant control-fidelity,* Nature Nanotechnology **9**, 981 (2014).

[9] E. Kawakami, P. Scarlino, D. R. Ward, F. R. Braakman, D. E. Savage, M. G. Lagally, M. Friesen, S. N. Coppersmith, M. A. Eriksson, and L. M. K. Vandersypen, *Electrical control of a long-lived spin qubit in a Si/SiGe quantum dot,* Nature Nanotechnology **9**, 666 (2014).

[10] J. Yoneda, K. Takeda, T. Otsuka, T. Nakajima, M. R. Delbecq, G. Allison, T. Honda, T. Kodera, S. Oda, Y. Hoshi, *et al.*, *A quantum-dot spin qubit with coherence limited by charge noise and fidelity higher than 99.9%,* Nature Nanotechnology **13**, 102 (2018).

[11] M. Veldhorst, C. H. Yang, J. C. C. Hwang, W. Huang, J. P. Dehollain, J. T. Muhonen, S. Simmons, A. Laucht, F. E. Hudson, K. M. Itoh, A. Morello, and A. S. Dzurak, *A two-qubit logic gate in silicon,* Nature **526**, 410 (2015).

[12] T. F. Watson, S. G. J. Philips, E. Kawakami, D. R. Ward, P. Scarlino, M. Veldhorst, D. E. Savage, M. G. Lagally, M. Friesen, S. N. Coppersmith, M. A. Eriksson, and L. M. K. Vandersypen, *A programmable two-qubit quantum processor in silicon,* Nature **555**, 633 (2018).

[13] X. Xue, T. Watson, J. Helsen, D. R. Ward, D. E. Savage, M. G. Lagally, S. N. Coppersmith, M. Eriksson, S. Wehner, and L. Vandersypen, *Benchmarking gate fidelities in a si/sige two-qubit device,* Physical Review X **9**, 021011 (2019).

[14] D. M. Zajac, A. J. Sigillito, M. Russ, F. Borjans, J. M. Taylor, G. Burkard, and J. R. Petta, *Resonantly driven CNOT gate for electron spins,* Science **359**, 439 (2018).

[15] W. Huang, C. Yang, K. Chan, T. Tanttu, B. Hensen, R. Leon, M. Fogarty, J. Hwang, F. Hudson, K. M. Itoh, *et al.*, *Fidelity benchmarks for two-qubit gates in silicon,* Nature **569**, 532 (2019).

[16] N. Hendrickx, D. Franke, A. Sammak, G. Scappucci, and M. Veldhorst, *Fast two-qubit logic with holes in germanium,* Nature **577**, 487 (2020).

[17] L. Petit, H. Eenink, M. Russ, W. Lawrie, N. Hendrickx, S. Philips, J. Clarke, L. Vandersypen, and M. Veldhorst, *Universal quantum logic in hot silicon qubits,* Nature **580**, 355 (2020).

[18] A. Sigillito, M. Gullans, L. Edge, M. Borselli, and J. Petta, *Coherent transfer of quantum information in a silicon double quantum dot using resonant swap gates,* npj Quantum Information **5**, 1 (2019).

[19] A. Barenco, C. H. Bennett, R. Cleve, D. P. DiVincenzo, N. Margolus, P. Shor, T. Sleator, J. A. Smolin, and H. Weinfurter, *Elementary gates for quantum computation,* Physical Review A **52**, 3457 (1995).

[20] M. Veldhorst, H. G. J. Eenink, C. H. Yang, and A. S. Dzurak, *Silicon CMOS architecture for a spin-based quantum computer,* Nature Communication **8**, 1766 (2017).

[21] L. M. K. Vandersypen, H. Bluhm, J. S. Clarke, A. S. Dzurak, R. Ishihara, A. Morello, D. J. Reilly, L. R. Schreiber, and M. Veldhorst, *Interfacing spin qubits in quantum dots and donors—hot, dense, and coherent,* npj Quantum Information **3**, 34 (2017).

[22] R. Li, L. Petit, D. P. Franke, J. P. Dehollain, J. Helsen, M. Steudtner, N. K. Thomas, Z. R. Yoscovits, K. J. Singh, S. Wehner, *et al.*, *A crossbar network for silicon quantum dot qubits,* Science Advances **4**, eaar3960 (2018).

[23] M. Urdampilleta, D. J. Niegemann, E. Chanrion, B. Jadot, C. Spence, P.-A. Mortemousque, L. Hutin, B. Bertrand, S. Barraud, R. Maurand, *et al.*, *Gate-based high fidelity spin read-out in a cmos device,* Nature Nanotechnology **14**, 737 (2019).

[24] M. Russ, D. M. Zajac, A. J. Sigillito, F. Borjans, J. M. Taylor, J. R. Petta, and G. Burkard, *High-fidelity quantum gates in si/sige double quantum dots,* Physical Review B **97**, 085421 (2018).

[25] G. Burkard, D. Loss, D. P. DiVincenzo, and J. A. Smolin, *Physical optimization of quantum error correction circuits,* Physical Review B **60**, 11404 (1999).

[26] B. M. Maune, M. G. Borselli, B. Huang, T. D. Ladd, P. W. Deelman, K. S. Holabird, A. A. Kiselev, I. Alvarado-Rodriguez, R. S. Ross, A. E. Schmitz, *et al.*, *Coherent singlet-triplet oscillations in a silicon-based double quantum dot,* Nature **481**, 344 (2012).

[27] Y. He, S. Gorman, D. Keith, L. Kranz, J. Keizer, and M. Simmons, *A two-qubit gate between phosphorus donor electrons in silicon,* Nature **571**, 371 (2019).

[28] L. M. Vandersypen and I. L. Chuang, *Nmr techniques for quantum control and computation,* Reviews of Modern Physics **76**, 1037 (2005).

[29] J. M. Martinis and M. R. Geller, *Fast adiabatic qubit gates using only σ z control,* Physical Review A **90**, 022307 (2014).

[30] U. Güngördü and J. Kestner, *Pulse sequence designed for robust c-phase gates in simos and si/sige double quantum dots,* Physical Review B **98**, 165301 (2018).

[31] F. Calderon-Vargas, G. S. Barron, X.-H. Deng, A. Sigillito, E. Barnes, and S. E. Economou, *Fast high-fidelity entangling gates for spin qubits in si double quantum dots,* Physical Review B **100**, 035304 (2019).

[32] U. Güngördü and J. Kestner, *Analytically parametrized solutions for robust quantum control using smooth pulses,* Physical Review A **100**, 062310 (2019).

[33] U. Güngördü and J. Kestner, *Robust implementation of quantum gates despite always-on exchange coupling in silicon double quantum dots,* Physical Review B **101**, 155301 (2020).

[34] J. V. Koski, A. J. Landig, M. Russ, J. C. Abadillo-Uriel, P. Scarlino, B. Kratochwil, C. Reichl, W. Wegscheider, G. Burkard, M. Friesen, *et al.*, *Strong photon coupling to the quadrupole moment of an electron in a solid-state qubit,* Nature Physics **16**, 642 (2020).

[35] Y.-C. Yang, S. Coppersmith, and M. Friesen, *Achieving high-fidelity single-qubit gates in a strongly driven charge qubit with 1/f charge noise,* npj Quantum Information **5**, 1 (2019).

[36] D. F. V. James, P. G. Kwiat, W. J. Munro, and A. G. White, *Measurement of qubits,* Physical Review A **64**, 052312 (2001).

7

A CROSSBAR NETWORK FOR SILICON QUANTUM DOT QUBITS

Identifying scalable quantum computing architectures is one of the greatest scientific challenges today. Current quantum dot chip designs require a high number of input-output connections (IOs) per qubit and this makes the wiring of large systems practically impossible. In order to increase the number of qubits to the thousands or millions needed for practical quantum information, we present in this chapter an architecture based on shared control and a scalable number of lines. Crucially, the control lines define the qubit grid, such that no local components are required. The design enables qubit coupling beyond nearest neighbors, providing prospects for non-planar quantum error correction protocols. A double stripline on top of the structure can drive high fidelity single-qubit rotations. Qubit addressability and readout are enabled by self-aligned inhomogeneous magnetic fields induced by direct currents through superconducting gates. Finally, qubit coupling is based on the exchange interaction, and we show that parallel two-qubit gates can be performed at the detuning noise insensitive point. While the architecture requires a high level of uniformity in the materials and dimensions to enable shared control, it stands out for its simplicity and provides prospects for large-scale quantum computation in the near future.

Parts of this chapter have been published in **Science Advances 4**, eaar3960 (2018) [1].

7.1. CROSSBAR TECHNOLOGY

The widespread interest in quantum computing has motivated the development of conceptual architectures across a range of disciplines [2–6]. Remarkable differences between the various approaches become apparent when considering the physical size of the qubit. In particular, 10^9 qubits defined by the spin states of semiconductor quantum dots could fit in an area of less than 5 mm × 5 mm, which is orders of magnitude smaller than what would be required by microwave-trapped ions or superconducting qubits [3, 6]. Small components can provide essential benefits in terms of scalability, and efforts to demonstrate the physical operations have already culminated in the realization of high-fidelity single-qubit rotations, two-qubit logic gates and small quantum algorithms [7–11]. However, as current qubit technology requires control lines for every qubit, a key challenge is to avoid an interconnect bottleneck for full control over a large qubit grid [12].

Conventional processors can have more than 2 billion transistors on a 21.5 × 32.5 mm^2 die [13]. Such a high packaging density crucially relies on a limited number of input-output connections (IOs). Transistor-to-IO ratios can be as high as 10^6 [12] because of the integration of the so-called crossbar technology. Combinations of row lines (RLs) and column lines (CLs) enable the identification of unique points on a grid structure, providing a mechanism for large-scale parallel and rapid read/write instructions. In decades of advancements in semiconductor technology, this concept has resulted in today's most powerful supercomputers. The idea to implement similar shared control schemes for quantum systems has been introduced for donor-based systems [4] and later proposed for quantum dot spins [5, 12]. In the work by Hill et al. [4], qubits are defined on the nuclear spin states of phosphorus donors in silicon, and a scheme is introduced where electrons can be shuttled to and from the donor using shared control. The change in charge occupation after shuttling shifts the resonance frequency of the nuclear spin qubit and thus provides qubit addressability. In the work by Veldhorst et al. [5], floating gates addressed via transistor circuits connected to a crossbar array control quantum dot qubits. This stimulated early proof-of-principle operations, such as local transistor-controlled charge detection [14], but requires extensive developments in downscaling and developing new devices such as vertical transistors. Thus, while both proposals offer the prospect of a significant reduction in the number of connections to external control logic, they also rely on feature sizes and integration schemes that are not compatible with today's industry standards and that are far beyond current experimental capabilities.

Here, we propose a crossbar scheme for a two-dimensional (2D) array of quantum dots that can operate a large number of qubits with high fidelity. The structure is simple and elegant in design and does not require extremely small feature sizes, but instead relies on a high level of uniformity. Specifically, we require that a single voltage applied to a common gate can bring individual dots to the single-electron occupancy. In addition, depending on the operation mode, we require that the variation of tunnel coupling between quantum dots can be engineered to be within one order of magnitude. Continuous progress in fabrication has already led to individual double-dot systems with this level of charge uniformity [15, 16]. We envisage that metrics, such as variation in threshold voltage, charging energy, and tunnel coupling, will need to improve by approximately

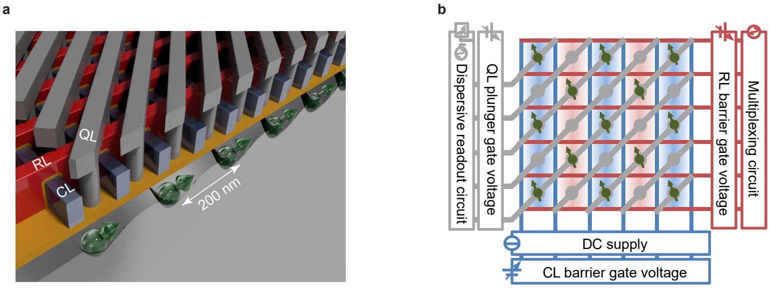

Figure 7.1: **a** Three-dimensional model of the array gate structure. The dielectrics in between the various gate layers are left out for clarity. **b** Schematic representation of the 2D quantum dot array. CLs (blue), RLs (red), and QLs (gray) connect the qubit grid to outside electronics for control and readout. A combination of these lines enables qubit selectivity. In the state shown here, half of the quantum dots are occupied with a single electron, where the electron spin encodes the qubit state. The electrons can be shuttled around via the gate voltages, providing a means to couple to nearest neighbors for two-qubit logic gates and readout and to couple to remote qubits for long-range entanglement.

an order of magnitude to use common gates in large quantum dot grids, and a promising platform to achieve this is advanced semiconductor manufacturing. Building upon these arrays, we introduce a spin qubit module that combines global charge control, local tunability, and electron shuttling between dots with alternating local magnetic fields and global electron spin resonance (ESR) control. Truly large-scale quantum computing can be achieved by connecting multiple of these qubit modules.

7.2. QUBIT GRID LAYOUT

Figure 7.1a schematically shows the gate layout of the qubit module containing a 2D quantum dot array. The qubits are based on the spin states of single electrons that are induced by electric gates in isotopically purified silicon (^{28}Si) quantum dots, reducing decoherence due to nuclear spin noise [8]. The architecture is agnostic to the integration scheme. The quantum dots can be located at a Si-SiO$_2$ interface [8], where the abrupt change in band structure can cause a large valley splitting energy, leading to well-isolated qubit states. Alternatively, the quantum dots can be formed in a Si-SiGe quantum well stack [7], where the epitaxial nature of the SiGe interface may be beneficial to meet the required uniformity for global operation as considered in this proposal.

The architecture consists of a crossbar gate structure of three in-plane layers (see Fig. 7.1a and b and superconducting striplines on top). The striplines deliver global radio frequency (RF) pulses to manipulate the spin state, as will be discussed below. The first layer hosts the CLs, which supply voltages to the horizontal barrier gates. The CLs also carry direct currents (DC) for the generation of the magnetic field pattern (see also Fig. 7.2c and d). These gates are deposited as the first layer to accommodate a well-defined cross section and are made of superconducting material. The subsequent RLs are isolated from the first layer of gates and supply the voltages to the vertical barrier gates. The plunger gates are formed through vias that connect to the qubit lines (QLs). This gating scheme does not require smaller manufacturing elements than the quantum dots and the interdot tunnel barriers. Here, we consider barrier and plunger gate widths of 30 and 40 nm, respectively, and quantum dot pitch spacing of 100 nm. These numbers enable more than 1000 qubits to fit in an area smaller than 5 µm x 5 µm (note that, in this architecture, half of the quantum dots host a qubit, increasing the area by a factor of 2). These dimensions are compatible with advanced semiconductor manufacturing and multiple patterning [17].

Figure 7.1b shows a conceptual image of a qubit module. In the idle state, each qubit has four empty neighboring dots. This is achieved by setting the bias voltages applied to the diagonal qubit gates, alternating between accumulation and depletion modes. This sparse occupation has several advantages: it increases the number of control gates per qubit without changing the physical gating density, the sparsely spaced qubits reduce crosstalk, and the empty sites will enable the shuttling of qubits between different sites. The gate pattern allows for selective addressing of qubits with the combined operation of the different gate layers, as discussed below. For N qubits occupying a square dot array, the combined control reduces the total number of gate lines to $N_{\mathrm{totalwires}} \approx 4\sqrt{2N}+1$. The analog control signals can be fed through the qubit network at the periphery, and no additional control elements are needed within the grid. This allows for a dense packing of the quantum dots.

Since each gate is shared by a line of quantum dots, a high level of uniformity across the whole structure is required. These requirements can, however, be relaxed significantly when aiming for a parallel qubit operation in a line-by-line manner. Here, the long coherence times of silicon qubits become crucial [8]. We require that the tunnel coupling t_0 can be globally controlled to below 10 Hz in the off state and in the range of 10 to 100 GHz in the on state, depending on the operation mode. The lower bound is set by the error threshold due to unwanted shuttling during a quantum algorithm. We note that, while our architecture does not pose a theoretical upper bound to t_0, as arbitrarily large detuning energy ϵ could be applied to the empty dots to suppress unwanted processes, very large t_0 will require impractically large voltages on the gates. Similarly, variations in the chemical potential energy $\Delta\mu$ could be overcome by applying an even larger detuning energy ϵ, together by exploiting the regime where the tunnel barriers can be pulsed on and off. However, we require $\Delta\mu < E_C$, where E_C is the charging energy. This significantly reduces overhead in correcting pulses and pulsing amplitude and increases operation speed.

Another challenge is to overcome crosstalk, such that physical parameters as ϵ and t_0 can be controlled individually [16]. Here, the highly repeatable nature and the presence of only straight lines in our architecture are strongly favorable. Compensating the crosstalk of an individual line by tuning the associated neighbor lines provides a highly symmetric approach. In the following discussion, we assume the presence of such compensation but refer to the main lines only.

7.3. SINGLE-QUBIT CONTROL

Single-qubit rotations are performed using global ESR striplines (see Fig. 7.2a) providing in-plane RF magnetic fields [8]. A modest external DC magnetic field is applied in the out-of-plane direction. Here, we consider an amplitude of 3.6 mT, which corresponds to a resonance frequency ν_0 of 100 MHz for the electron spin. This rather low mag-

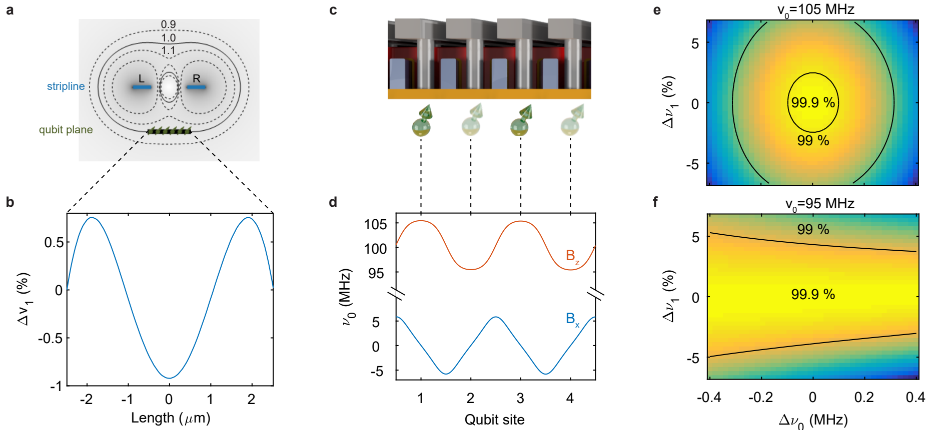

Figure 7.2: **a** Cross section of the stripline pair (2 μm in width and 6 μm in pitch) positioned 4 μm above the qubit plane. The gray background with black contour lines visualizes the RF magnetic field generated by driving currents through the striplines. **b** The double stripline is optimized to minimize the variations in RF magnetic field at the qubit plane, and we find peak-to-peak values below 2%. **c** Cross section of the qubit plane. A DC alternating in direction between even and odd CLs together with an external out-of-plane field generates a static field that alternates column by column. **d** Corresponding resonance frequency profile. For CLs with dimensions 30 nm wide and 60 nm high and positioned 20 nm above the qubit plane, the required current $I_{\mathrm{CL}} \approx 70\,\mu\mathrm{A}$ and current density $j_{\mathrm{CL}} \approx 4\times10^{10}\,\mathrm{A/m^2}$. The field component B_z has local maxima and minima at the qubit sites, where B_x vanishes, providing qubit addressability and first-order insensitivity to qubit placement. **e-f** Column-selective qubit pulses are engineered using GRAPE. The GRAPE pulse is designed to tolerate static variations in the ν_0 and ν_1. We conclude that single-qubit rotations can be performed with fidelity higher than 99.9 % in the 2D qubit array. Here, we use an electron g-factor of 2 and show the static field by the resonance frequency ν_0 and the ESR field by the normal on-resonance Rabi frequency ν_1.

netic field and resonance frequency ease the RF circuit design requirements. In addition, the qubit-to-qubit resonance frequency variation due to spin-orbit coupling [18, 19] is strongly reduced in low magnetic fields and further minimized by applying the magnetic field perpendicular to the interface [20]. The ensemble ESR linewidth can then become narrow enough to achieve high-fidelity operation with a global ESR signal. Moreover, we expect improved qubit coherence due to a strongly reduced sensitivity to electrical noise in low fields, as coupling to charge noise via spin-orbit coupling is strongly reduced [20].

Local spin rotations could, in principle, also be implemented by integrating nanomagnets and operation based on electric dipole spin resonance (EDSR) [7]. To obtain Rabi frequencies f_{Rabi} beyond 1 MHz, the required transverse field gradient is 0.1 to 0.5 mT/nm for typical driving amplitudes and dot sizes [7]. However, while EDSR has proven powerful in single-qubit devices, the integration of nanomagnets in a dense 2D array is much more demanding. In particular, achieving the large required transverse field gradients will also lead to longitudinal field gradients. These will likely affect qubit coherence, shuttling, and two-qubit logic gates. Furthermore, a large gradient appears incompatible with the low-field operation proposed here. Therefore, qubit operation via ESR, requiring minimal field differences, is preferable for spin manipulation in this 2D array design.

To model the striplines and analyze the uniformity and amplitude of the RF fields they generate, we use the Microwave Studio software package from Computer Simulation Technology (CST-MWS). To reach high uniformity across the 2D qubit array, we designed a superconducting stripline pair. We use our CST-MWS model to optimize the relevant dimensions of the stripline design. Furthermore,to achieve homogeneous fields, the current distribution through the striplines has to be taken into account. For thin-film superconducting striplines, this is, to a large extent, determined by the effective penetration depth λ_{eff}. We find that already for $\lambda_{\text{eff}} > 0.5\,\mu\text{m}$, the corresponding RF field inhomogeneity across the 2D array can be less than $\delta\nu = 2\%$ as shown in Fig. 7.2b. In addition, Rabi driving at 10 MHz requires 0.6 mA in each stripline and reasonable current densities $j_{\text{stripline}} = 3 \times 10^9\,\text{A/m}^2$ in the stripline pair for a thickness of 100 nm.

To achieve qubit addressability, a column-by-column alternating magnetic field is generated by passing DCs with alternating directions through the CL, as shown in Fig. 7.2c and d. The targeted $\delta\nu_{\text{CL}} = 10\,\text{MHz}$ frequency difference between columns requires current densities $j_{\text{CL}} \approx 4 \times 10^{10}\,\text{A/m}^2$ in the gate lines. The integration of superconducting lines as considered here suppresses heat dissipation and minimizes, in addition, potential differences along the lines. The expected field profile along a row of qubits is plotted in Fig. 7.2d. Spin-orbit coupling in silicon is strongly enhanced close to an interface and in the presence of large vertical electrical fields, which leads to significant qubit-to-qubit variations in resonance frequency [18, 19, 21]. These variations depend on the microscopic interface, and even a single atomic step edge can have a strong impact; it will thus be a significant challenge to overcome these variations by fabrication methods only. In typical silicon metal-oxide-semiconductor quantum dots, the variations in the g-factor are up to $\Delta g/g = 1 \times 10^{-2}$ [18, 21]. In SiGe devices, the variations are predicted to be an order of magnitude smaller, $\Delta g/g = 1 \times 10^{-3}$ [19]. Possible optimization strategies to reduce variations could focus on the perpendicular electric field or on the material stack. However, by operating in the low magnetic field regime and by applying the field perpendicular to the interface [20] as proposed here, the qubit-to-qubit variation is expected to vanish, and we take a conservative estimate $\delta\nu_{\text{SOC}} = 50\,\text{kHz}$.

7

Imperfect device fabrication can result in local variations of the magnetic field. This impact is minimized because the magnetic field is self-aligned with the quantum dot barriers defined by the CLs. Furthermore, the magnetic field pattern is designed to have local minima or maxima at the qubit positions, such that the qubit energy splittings are, to first order, insensitive to variations in location. The dominant contributions to variations in ν_0 will thus come from variations in the geometry of the gates. For a 1-nm root mean square variation in gate geometry, which can be achieved with current semiconductor manufacturing technology [17], we estimate the corresponding resonance frequency linewidth to be $\delta\nu_{\text{fab}} = 100\,\text{kHz}$. On the basis of these considerations, we find a total variation $\delta\nu_0 = \delta\nu_{\text{fab}} + \delta\nu_{\text{SOC}} = 150\,\text{kHz}$.

For the implementation of global high-fidelity single-qubit operations, it is central that the RF pulses are forgiving with respect to the inhomogeneity in field, as discussed above. At the same time, the pulses need to be highly frequency-selective to ensure that no unintended qubit rotations or phase shifts are induced in the off-resonant columns. Considering these challenges, we applied gradient ascent pulse engineering (GRAPE) for ESR spin control [22], as shown Fig. 7.2e and f. With this technique, we can achieve single-qubit fidelities above 99.9 percent and crosstalk below 0.1 percent and perform a

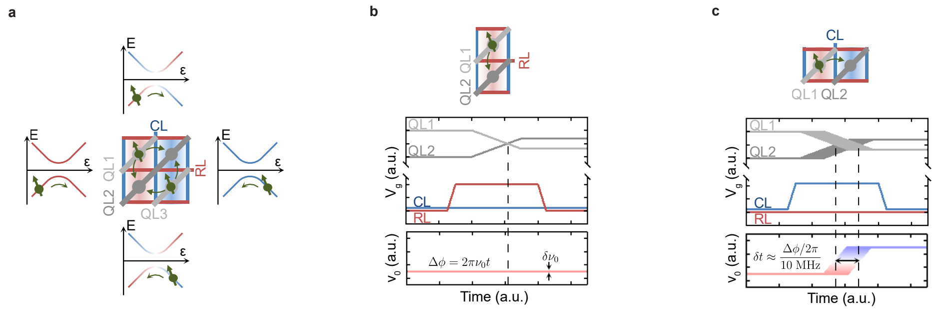

Figure 7.3: **a** By controlling the tunnel coupling and potentials of the dots, qubits can be shuttled around. **b** Shuttling along a column. The sequence consists of setting the tunnel coupling by RL, followed by pulsing the detuning energy. This process leaves the qubit resonance frequency unaffected except for unintended qubit-to-qubit variations. **c** Shuttling along a row. This process results in an additional 10 MHz shift in the qubit resonance frequency due to the magnetic field difference between adjacent columns. The shuttling is tuned by controlling the pulsing time on QL1 and QL2. The resulting time delay Δt leads to a controllable phase $\Delta\phi$ applied to the qubit, and this is the basis for our phase updates and Z-gates.

$\pi/2$ rotation within 250 ns. The tolerance levels for this fidelity are up to 300 kHz in ν_0 and more than 3 percent in ν_1. For comparison, the expected qubit-to-qubit variation based on the discussion above falls well within the 99.9 percent fidelity domain. We note that the values reported denote peak-to-peak variations, such that many qubits will have significantly higher fidelity. This implies that further optimization could be done if a certain number of faulty qubits can be tolerated.

7.4. SHUTTLING QUBITS FOR ADDRESSABILITY AND ENTANGLEMENT

We now turn to the shuttling of electrons [23, 24] as a means to create addressability for single- and two-qubit logic gates, as well as an efficient method for (remote) qubit swap. The general principle behind the crossbar operation is the combined control of ϵ and t_0. Since detuning and tunneling are controlled by different layers of gates, each qubit can be selectively addressed at the corresponding crossing point.

Figure 7.3 visualizes qubit shuttling along a row or column. Shuttling involves a change in the qubit resonance frequency. Therefore, the electron wave function has to be shifted diabatically with respect to the spin Hamiltonian, so that we can shuttle the qubit between different sites while preserving its spin state. By using a nonlinear pulsing scheme, we can operate the qubit shuttling up to at least 1 GHz with a fidelity higher than 99.9 percent when accounting for small t_0 and a large pulsing amplitude for uniformity requirements. The difference in the Larmor frequency between adjacent columns can be exploited to construct fast Z-gates operating at 10 MHz (see Fig. 7.3c). This can be used to correct phase errors or to implement a Z-gate in a quantum algorithm simply by temporarily moving a qubit to an adjacent column for a properly calibrated duration.

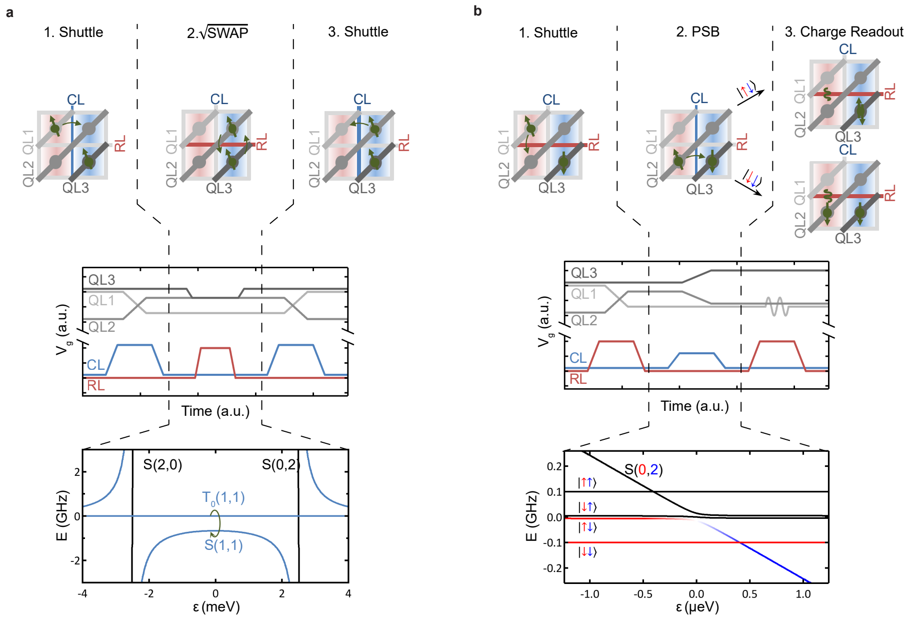

Figure 7.4: **a** Sequence for $\sqrt{\text{SWAP}}$ gates. By shuttling the respective qubits to the same column, the resonance frequency difference is minimized, enabling a high-fidelity $\sqrt{\text{SWAP}}$. The logic gate is performed at the symmetry point, making the qubits to first-order insensitive to detuning noise, and the interaction is controlled by the associated RL. **b** Spin qubit readout. Here, the respective qubits are shuttled to reside in the same row. The ancillary qubit, located at the blue column with the larger Zeeman energy, is manipulated to the spin-down state. The measurement qubit is adiabatically pulsed. The qubit shuttles when the state is spin up and is blocked when the state is spin down because of the Pauli spin blockade (PSB). Subsequently, the tunnel coupling is turned off, and the charge is locked. Dispersive charge state readout occurs by exploiting an empty neighbor dot.

7.5. TWO-QUBIT LOGIC GATES AND PSB READOUT

Two types of two-qubit gates can be implemented with quantum dots, namely, the $\sqrt{\text{SWAP}}$ and the controlled-phase (CPHASE) gate [9, 10, 25, 26]. A direct implementation of the CPHASE gate, however, requires the Zeeman energy difference to be much larger than the exchange coupling, $\delta E_z \gg J$, to reach high fidelity. The small field gradient $\delta E_z = 10\,\text{MHz}$ considered here will not fully suppress SWAP-type rotations reducing the fidelity. As discussed in the previous chapters a possible solution could be to engineer composite pulses, but here we focus on $\sqrt{\text{SWAP}}$ as the central two-qubit gate (see Fig. 7.4a). Together with single-qubit rotations, this provides a universal quantum gate set. For example, a CNOT is obtained by interleaving a Z-gate in between two $\sqrt{\text{SWAP}}$ operations, where the Z-gate can be conveniently realized by using the shuttling scheme. To execute the $\sqrt{\text{SWAP}}$, we shuttle two qubits into the same column such that the g-factor difference is minimized, and we tune the qubit exchange by controlling the tunneling barrier gate while keeping the two qubits at the charge symmetry point with the qubit gates [25, 26].

In the low magnetic field regime discussed here, reservoir-based spin initialization and readout are not possible because of thermal broadening. Therefore, we use the Pauli spin blockade between two electrons on neighboring sites for spin initialization and readout. This method has the additional advantage of not requiring a reservoir next to the qubit. The protocol relies on the difference in Zeeman energy between the two quantum dots to enable spin parity projection. This difference in energy is created by the same column-by-column alternating magnetic field used to create qubit addressability, and readout is performed between neighboring quantum dots in different columns.

The Pauli spin blockade spin-to-charge conversion scheme is plotted in Fig. 7.4b. Instead of shuttling along a row, which brings two qubits to adjacent sites in the same column (same resonance frequency), the qubit is now moved along a column. This brings it next to a qubit in a different column, providing the difference in Zeeman energy that is necessary for readout. In the sequence shown in Fig. 7.4b, the qubit with the smaller Zeeman energy (red background) will be read out. The qubit with the larger Zeeman energy (blue background) serves as an ancillary qubit and must be in the spin-down state, so that other triplet states (see black lines in Fig. 7.4b) can be neglected. If required, single-qubit pulses could be applied to manipulate the ancillary qubit to the spin-down state. By tuning to the configuration where the singlet state becomes the ground state on the ancillary dot, the Pauli spin blockade will prevent (allow) the spin-down (up) electron to shuttle to the ancillary qubit. The above process completes the spin-to-charge conversion, and the spin state can be inferred from the charge occupation. A conversion fidelity higher than 99.9 percent can be achieved with a 3 MHz gate pulsing speed. We note that, in another protocol, the ancillary qubit can be in the spin-up state, provided that it resides in the column with the smaller Zeeman energy. This possibility could prove to be powerful in quantum error correction cycles, as it avoids the need to actively correct errors. In addition, the reverse of the Pauli spin blockade spin-to-charge conversion pulsing process is used for qubit initialization. In the scheme shown in Fig. 7.4b, if the Pauli spin blockade prevented the qubit to move to the ancillary qubit in the readout step, then it is and remains in the spin-down state. If the qubit moved to the ancillary qubit, it was in the spin-up state before readout. After detuning back, it will return to the spin-up state. In both cases, the ancillary qubit will end up in the spin-down state.

Directly after the Pauli spin blockade spin-to-charge conversion, we switch off the interdot tunnel coupling with CL so that the charge state is disconnected from the spin configuration. In this mode, the state is not sensitive to spin relaxation, thereby increasing the readout fidelity. This can be exploited for delayed readout schemes, such as charge sensor–based readout, by shuttling to the periphery of the 2D array. However, here, we consider gate-based dispersive readout [14, 27] for an on-site readout of the charge state, as shown in Fig. 7.4b. By applying an RF carrier signal to the qubit gates and coupling the dot to an adjacent empty dot, the charge state can be extracted from the dispersive signal. When there is charge occupation, the interdot oscillation driven by the RF carrier gives an additional quantum capacitance, leading to a different reflected signal compared to the state without charge occupation. By measuring the reflected signal, we thus determine the qubit state.

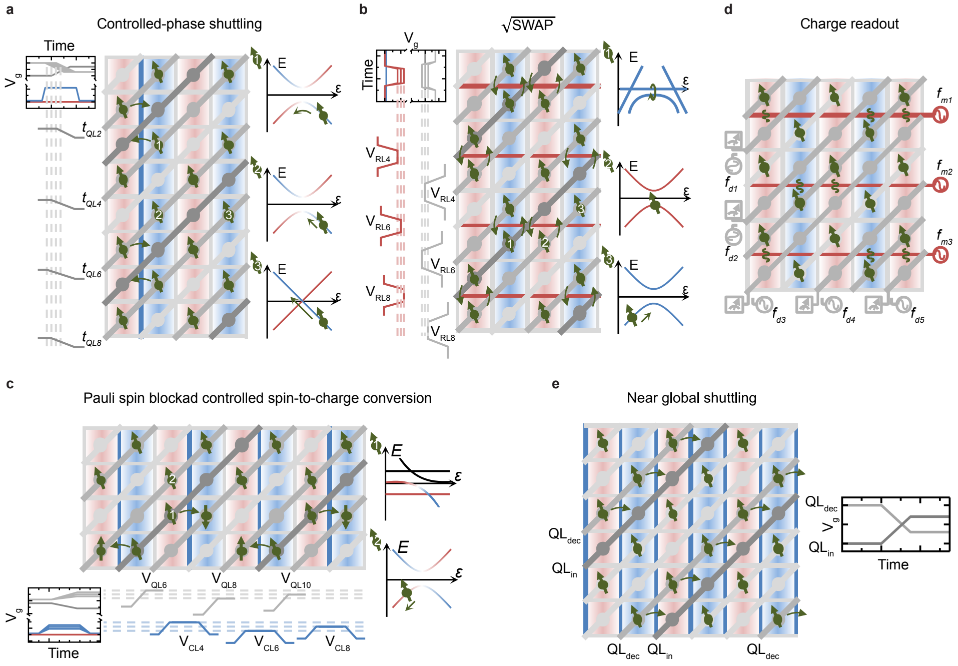

Figure 7.5: **a-c** Simultaneous operation of controlled-phase shuttling **a**, two-qubit $\sqrt{\text{SWAP}}$ operations **b**, and spin-to-charge conversion **c** can be achieved in a line-by-line manner. In each figure, inset (1) denotes the energy-detuning diagram of the targeted qubit(s). Insets (2) and (3) show the consequence on the remaining qubits, where detuning, tunnel coupling, or the local magnetic field minimizes errors. **d-e** Shuttling without phase control **d** and charge readout **e** can be performed in a near-global manner. **a** Shuttling of qubits. Parallelism is obtained along one direction, and tunability is obtained along another direction, and the respective gates control the timing and detuning to overcome qubit-to-qubit variations. Here, the target qubits shuttle from column to column, whereas the other qubits are blocked by ϵ or t_0. **b** Two-qubit logic gates. $\sqrt{\text{SWAP}}$ operations only occur between tunnel-coupled neighboring qubits. The remaining qubits do not interact but could shuttle in a column. The resulting (small) phase shift can be corrected by the consecutive shuttle event in the line-by-line operation. In **c**, Pauli spin blockade spin-to-charge conversion occurs between tunnel-coupled qubits. Qubits coupled to an empty dot do not shuttle, prevented by the energy alignment, since we require $\Delta\mu < E_C$. **d** Shuttling without phase control enables to construct a variety of shuttle patterns that can be operated almost globally; the schematic here shows the simultaneous shuttling of half of the qubits one site to the right. **e** The dispersive charge readout, performed after the spin-to-charge conversion shown in **c**, can be performed simultaneously by including frequency multiplexing. The RF carrier on QL (fd) is then modulated by the application of additional multiplexing RF pulses (fm) to RL.

7.6. PARALLEL OPERATION

For an efficient quantum computing scheme, simultaneous operation is essential. Here, we discuss how the local operations introduced above can be advanced toward line-by-line or even near-global operation. Contrary to local operations, parallel operations result in active gates crossing at quantum dots that are not targeted (see Fig. 7.5). This may lead to undesired operations. However, these can be prevented by selectively occupying the quantum dots and specific control of ϵ or t_0, such that away from the targeted locations signals are only applied to empty quantum dots or to quantum dots with empty neighbors. We also note that the crossbar control scheme could affect non-targeted qubits under the active gates, for example, via Stark shifts. Understanding and managing the consequences of these errors is thus highly important. In our architecture, we minimize these errors by operating at low magnetic field, designing qubit columns with well-separated resonance frequencies, and using adiabatic pulsing schemes such that the crosstalk errors are significantly smaller than the errors on the targeted qubits. Furthermore, we note that these errors can be largely corrected in subsequent operations with a manageable overhead, for example, by implementing an additional phase-controlled shuttling step.

Figure 7.5a shows an example of a line-by-line operation of controlled-phase shuttling. To properly control the timing, it is crucial to individually pulse the QL. Still, parallel shuttling operations can be implemented along one column or row, enabled by lifting the barriers controlled by one CL or RL, respectively. These CLs can be time-controlled individually to correct the qubit-to-qubit variations, such that the shuttled qubits have the correct phase after the shuttling. The line-by-line shuttle can be performed within 1 ns with a fidelity beyond 99.9%.

An approach to performing simultaneous two-qubit logic operations on the qubit module could be to shuttle line by line all target qubits to the associated control qubits and then perform $\sqrt{\mathrm{SWAP}}$ operations line by line. However, this will lead to qubit configurations where targeted qubits share gate lines disabling individual gate control, which is essential for high-fidelity operation. To overcome this, we propose sequences whereby a single column (or row) of qubits is shuttled first, followed by the desired operation and shuttle back, and then the sequence is continued by operating the next line of qubits of the module until all qubits are addressed. This protocol is demonstrated in Fig. 7.5b, which shows the configuration after shuttling a single column of qubits. To overcome variations in tunnel couplings and chemical potentials, we tune the amplitude and duration of the pulses applied to the respective RLs and CLs individually for each two-qubit gate to achieve the desired operation. For example, operations can be performed at the detuning-noise insensitive charge symmetry point [25, 26]. Consequently, the line-by-line control does not limit the operation speed, and we envision operation frequencies in the range of 10 to 100 MHz for two-qubit logic gates.

Simultaneous readout consists of a spin-to-charge conversion step and charge readout step. First, a row of qubits is shuttled, resulting in the configuration shown in Fig. 7.5c. After that, the parameters ϵ and t_0 can be individually controlled to convert spin to charge. In this specific sequence here, qubits are alternately shuttled up or down along the row, which leads to a configuration that is typically compatible with error correction sequences [28, 29]. However, there may be instances where a different configuration is required, and this could reduce the spin-to-charge conversion to half the speed compared to line-by-line.

Global charge readout requires us to distinguish between qubits connected to the same QL. This is achieved via frequency multiplexing, as shown in Fig. 7.5d. Here, an additional voltage modulation is applied to the RL. The separation of spin-to-charge conversion and charge readout in different steps has a particular advantage. While the initial spin-to-charge conversion must be performed line-by-line, it can be done relatively fast. The readout of charge is likely slower, and to overcome the non-uniformity in

$\Delta\mu$, a large detuning has to be applied. Instead of a single-step readout, we sequentially read out for different detuning and group the qubits according to their detuning. This sequential readout, as compared to the line-by-line approach, has the advantage that is independent on the number of qubits and will be efficient for large qubit modules. The total readout time will strongly depend on the performance of dispersive readout at the single-qubit level, now under intensive research. However, the protocol here shows that the slowdown with increasing numbers of qubits can be controlled.

Near-global operation is possible when phase control is not required. This may have multiple applications, for example, in achieving long-range coupling. In these protocols, multiple shuttles can be performed with a single phase match at the start or at an arbitrary point. An example of global shuttling is shown in Fig. 7.5e, where half of the qubits are simultaneously moved. Shuttling requires adiabatic movement with respect to the tunnel coupling, and the demand is most stringent close to the anticrossing point. Because of the qubit-to-qubit variations, it may not be possible to go beyond a linear detuning pulse, as each pair can have the anticrossing at a different location. This consequently limits the shuttle speed. Nonetheless, for a $\Delta\mu = 2\,\text{meV}$, shuttling can be at a 1-GHz rate when $t_0 > 25$ GHz.

7.7. WHERE WE ARE NOW

One of the greatest challenges in the area of scalability is avoiding an interconnect bottleneck. This chapter contains a proposal of a scalable solution for spin qubits based on crossbar technology. While this technology limits control, we have developed general operation schemes based on partial sequential control. The increased operation time due to sequential control is warranted by the very long coherence times of quantum dot spin qubits, with experimental demonstrations already up to 28 ms [8]. We have shown operation schemes for phase-controlled shuttling, two-qubit logic gates, and spin-to-charge conversion. These operations can have a targeted execution time well below 1 µs. The resulting loss of coherence due to the waiting time when operating in a line-by-line manner could be well below 10^{-3} in a 1000-qubit module using suitable echo sequences. The shuttling proposed here can be performed simultaneously within 1 ns, enabling even more than 10^7 operations, and could provide an excellent method to create long-range entanglement or remote qubit SWAP. Readout could become fast by global operation, and measurement-free quantum error correction schemes could reduce the need for frequent readout [30, 31].

While the proposed structure is compatible with existing technology, several aspects of the design require an experimental demonstration. Studies of the uniformity level on extended quantum dot arrays will validate the shared gate control scheme. Spin qubit operation in moderate magnetic fields have been demonstrated [32], but more work is needed to investigate the limits of single-qubit operation fidelity. After encouraging results of shuttling electron spin states in GaAs quantum dots [24], these experiments should be repeated in Si and, in particular, in ^{28}Si to investigate the fidelity that can be reached for the coherent shuttling, as proposed here. Studies of the fidelity of dispersive charge detection will enable to compare simultaneous readout with alternative shuttling and serial detection by one or several fast charge sensors. A feasibility study of quantum error correction [29] on this architecture on the single logical qubit scale suggests extremely low error rates, while the global shuttling scheme promises avenues to incorporate multiple logical qubits in a single module. Further scaling going beyond these modules will introduce new challenges, and interfacing protocols should account for the extra elements and the accompanying errors. In particular, long-range coupling of qubits will be crucial for ultimate scaling, and the errors due to the limited control inside these couplers should be included in future error analysis. If advances in qubit control continue to improve and lead to all fidelities higher than 99.9%, then the architecture discussed here provides an excellent way forward to large-scale quantum computation.

REFERENCES

[1] R. Li, L. Petit, D. P. Franke, J. P. Dehollain, J. Helsen, M. Steudtner, N. K. Thomas, Z. R. Yoscovits, K. J. Singh, S. Wehner, *et al.*, *A crossbar network for silicon quantum dot qubits,* Science Advances **4**, eaar3960 (2018).

[2] D. Loss and D. P. DiVincenzo, *Quantum computation with quantum dots,* Physical Review A **57**, 120 (1998).

[3] A. G. Fowler, M. Mariantoni, J. M. Martinis, and A. N. Cleland, *Surface codes: Towards practical large-scale quantum computation,* Physical Review A **86**, 032324 (2012).

[4] C. D. Hill, E. Peretz, S. J. Hile, M. G. House, M. Fuechsle, S. Rogge, M. Y. Simmons, and L. C. L. Hollenberg, *A surface code quantum computer in silicon,* Science Advances **1**, e1500707 (2015).

[5] M. Veldhorst, H. G. J. Eenink, C. H. Yang, and A. S. Dzurak, *Silicon CMOS architecture for a spin-based quantum computer,* Nature Communication **8**, 1766 (2017).

[6] B. Lekitsch, S. Weidt, A. G. Fowler, K. Mølmer, S. J. Devitt, C. Wunderlich, and W. K. Hensinger, *Blueprint for a microwave trapped ion quantum computer,* Science Advances **3**, e1601540 (2017).

[7] E. Kawakami, P. Scarlino, D. R. Ward, F. R. Braakman, D. E. Savage, M. G. Lagally, M. Friesen, S. N. Coppersmith, M. A. Eriksson, and L. M. K. Vandersypen, *Electrical control of a long-lived spin qubit in a Si/SiGe quantum dot,* Nature Nanotechnology **9**, 666 (2014).

[8] M. Veldhorst, J. Hwang, C. Yang, A. Leenstra, B. de Ronde, J. Dehollain, J. Muhonen, F. Hudson, K. M. Itoh, A. Morello, *et al.*, *An addressable quantum dot qubit with fault-tolerant control-fidelity,* Nature Nanotechnology **9**, 981 (2014).

[9] M. Veldhorst, C. H. Yang, J. C. C. Hwang, W. Huang, J. P. Dehollain, J. T. Muhonen, S. Simmons, A. Laucht, F. E. Hudson, K. M. Itoh, A. Morello, and A. S. Dzurak, *A two-qubit logic gate in silicon,* Nature **526**, 410 (2015).

[10] T. F. Watson, S. G. J. Philips, E. Kawakami, D. R. Ward, P. Scarlino, M. Veldhorst, D. E. Savage, M. G. Lagally, M. Friesen, S. N. Coppersmith, M. A. Eriksson, and L. M. K. Vandersypen, *A programmable two-qubit quantum processor in silicon,* Nature **555**, 633 (2018).

[11] D. M. Zajac, A. J. Sigillito, M. Russ, F. Borjans, J. M. Taylor, G. Burkard, and J. R. Petta, *Resonantly driven CNOT gate for electron spins,* Science **359**, 439 (2018).

[12] L. M. K. Vandersypen, H. Bluhm, J. S. Clarke, A. S. Dzurak, R. Ishihara, A. Morello, D. J. Reilly, L. R. Schreiber, and M. Veldhorst, *Interfacing spin qubits in quantum dots and donors—hot, dense, and coherent,* npj Quantum Information **3**, 34 (2017).

[13] B. Stackhouse, S. Bhimji, C. Bostak, D. Bradley, B. Cherkauer, J. Desai, E. Francom, M. Gowan, P. Gronowski, D. Krueger, *et al.*, *A 65 nm 2-billion transistor quad-core itanium processor,* IEEE Journal of Solid-State Circuits **44**, 18 (2008).

[14] S. Schaal, S. Barraud, J. Morton, and M. F. Gonzalez-Zalba, *Conditional dispersive readout of a cmos single-electron memory cell,* Physical Review Applied **9**, 054016 (2018).

[15] M. G. Borselli, K. Eng, R. S. Ross, T. M. Hazard, K. S. Holabird, B. Huang, A. A. Kiselev, P. W. Deelman, L. D. Warren, I. Milosavljevic, *et al.*, *Undoped accumulation-mode si/sige quantum dots,* Nanotechnology **26**, 375202 (2015).

[16] T. Hensgens, T. Fujita, L. Janssen, X. Li, C. J. Van Diepen, C. Reichl, W. Wegscheider, S. Das Sarma, and L. M. K. Vandersypen, *Quantum simulation of a Fermi–Hubbard model using a semiconductor quantum dot array,* Nature **548**, 70 (2017).

[17] W. van der Zande, *Euvl exposure tools for hvm: It's under (and about) control,* in *Proceedings of the EUV and Soft X-ray Source Workshop* (2016).

[18] M. Veldhorst, R. Ruskov, C. H. Yang, J. C. C. Hwang, F. E. Hudson, M. E. Flatté, C. Tahan, K. M. Itoh, A. Morello, and A. S. Dzurak, *Spin-orbit coupling and operation of multivalley spin qubits,* Physical Review B **92**, 201401 (2015).

[19] R. Ferdous, E. Kawakami, P. Scarlino, M. P. Nowak, D. Ward, D. Savage, M. Lagally, S. Coppersmith, M. Friesen, M. A. Eriksson, *et al.*, *Valley dependent anisotropic spin splitting in silicon quantum dots,* npj Quantum Information **4**, 1 (2018).

[20] R. M. Jock, N. T. Jacobson, P. Harvey-Collard, A. M. Mounce, V. Srinivasa, D. R. Ward, J. Anderson, R. Manginell, J. R. Wendt, M. Rudolph, *et al.*, *A silicon metal-oxide-semiconductor electron spin-orbit qubit,* Nature communications **9**, 1 (2018).

[21] R. Ferdous, K. W. Chan, M. Veldhorst, J. Hwang, C. Yang, H. Sahasrabudhe, G. Klimeck, A. Morello, A. S. Dzurak, and R. Rahman, *Interface-induced spin-orbit interaction in silicon quantum dots and prospects for scalability,* Physical Review B **97**, 241401 (2018).

[22] N. Khaneja, T. Reiss, C. Kehlet, T. Schulte-Herbrüggen, and S. J. Glaser, *Optimal control of coupled spin dynamics: design of nmr pulse sequences by gradient ascent algorithms,* Journal of magnetic resonance **172**, 296 (2005).

[23] J. Taylor, H.-A. Engel, W. Dür, A. Yacoby, C. Marcus, P. Zoller, and M. Lukin, *Fault-tolerant architecture for quantum computation using electrically controlled semiconductor spins,* Nature Physics **1**, 177 (2005).

[24] T. A. Baart, M. Shafiei, T. Fujita, C. Reichl, W. Wegscheider, and L. M. K. Vandersypen, *Single-spin ccd,* Nature Nanotechnology **11**, 330 (2016).

[25] M. Reed, B. Maune, R. Andrews, M. Borselli, K. Eng, M. Jura, A. Kiselev, T. Ladd, S. Merkel, I. Milosavljevic, *et al.*, *Reduced sensitivity to charge noise in semiconductor spin qubits via symmetric operation,* Physical Review Letters **116**, 110402 (2016).

[26] F. Martins, F. K. Malinowski, P. D. Nissen, E. Barnes, S. Fallahi, G. C. Gardner, M. J. Manfra, C. M. Marcus, and F. Kuemmeth, *Noise suppression using symmetric exchange gates in spin qubits,* Physical Review Letters **116**, 116801 (2016).

[27] J. Colless, A. Mahoney, J. Hornibrook, A. Doherty, H. Lu, A. Gossard, and D. Reilly, *Dispersive readout of a few-electron double quantum dot with fast rf gate sensors,* Physical Review Letters **110**, 046805 (2013).

[28] A. G. Fowler, M. Mariantoni, J. M. Martinis, and A. N. Cleland, *Surface codes: Towards practical large-scale quantum computation,* Physical Review A **86**, 032324 (2012).

[29] J. Helsen, M. Steudtner, M. Veldhorst, and S. Wehner, *Quantum error correction in crossbar architectures,* Quantum Science Technology **3**, 035005 (2018).

[30] V. Nebendahl, H. Häffner, and C. Roos, *Optimal control of entangling operations for trapped-ion quantum computing,* Physical Review A **79**, 012312 (2009).

[31] G. A. Paz-Silva, G. K. Brennen, and J. Twamley, *Fault tolerance with noisy and slow measurements and preparation,* Physical Review Letters **105**, 100501 (2010).

[32] R. Zhao, T. Tanttu, K. Y. Tan, B. Hensen, K. W. Chan, J. Hwang, R. Leon, C. H. Yang, W. Gilbert, F. Hudson, *et al.*, *Single-spin qubits in isotopically enriched silicon at low magnetic field,* Nature Communications **10**, 1 (2019).

8

OUTLOOK

This thesis is focused on the optimization of the performance and control of electron spin qubits at higher temperatures (Chapters 3, 4, 5, 6) and in dense two-dimensional arrays (Chapter 7). In this final chapter I explore possible improvements and future experiments, and position the discussion in the broader context of the field of spin qubits in quantum dots.

8.1. FUTURE DIRECTIONS

In the first four chapters of the thesis I discussed how electron spins in silicon quantum dots can be properly isolated and controlled, with sufficiently long coherence times, at temperatures above one Kelvin. In the following, I am going to discuss the areas where I see major possibilities for improvements in the short-term. The first aspect to be addressed is the qubit readout, which can be improved by the adoption of radio-frequency reflectometry. Secondly, I will move to quantum operations and explore what avenues exist to improve the control fidelities. The final section contains a discussion about recent developments in one- and two-dimensional spin qubit arrays.

8.1.1. QUBIT READOUT

In all the experiments discussed in this thesis, readout is achieved by monitoring the DC current of a single-electron-transistor, which is amplified and filtered at room temperature. This type of technique gives usually a measurement bandwidth of less than 100 kHz, limited by the RC equivalent circuit of the wiring and the current to voltage converter. An improvement in the readout speed, while keeping a good signal to noise ratio, is highly desirable since it allows for faster calibrations and more complicated experiments. One possibility is to move the amplification stage at the mixing chamber of the dilution refrigerator, which strongly reduces the impact of cabling capacitances [1]. In the following I will explore a different direction which is the adoption of radio frequency (rf) reflectometry [2].

In an rf reflectometry setup, the charge sensor is connected to an rf tank circuit. Any shift in the conductance of the sensor will result in a shift of the resonance frequency of the equivalent LRC circuit, which can be measured with a bandwidth around 1 MHz [3–5]. While rf reflectometry has been proven to be a successful technique in GaAs, its implementation in silicon presents new challenges. First of all, accumulation mode devices usually have a larger stray capacitance, coming from the large overlap between gates and the two-dimensional electron gas (2DEG). This parasitic capacitance negatively affects the readout performances since part of the rf signal goes in the lossy capacitive channel. Secondly, the reduced substrate mobility leads to larger electrical resistance of the charge sensor and the ohmic path, resulting in reduced sensitivity. These effects are amplified in particular in Si-MOS substrates, where, in comparison to Si-SiGe, the lower electron mobility and the enhanced proximity of the gates to the two-dimensional electron gases, make the implementation of rf reflectometry rather challenging.

These problems can be overcome by careful device design. First of all, new confinement gates can be introduced with the goal of cutting the 2DEGs running below the accumulation gates, therefore minimizing the capacitance. Secondly, the n++ doped region, which serve as source and drain for the charge sensor, can be moved as close as possible to the active device region in order to reduce the contact resistance. These solutions have been proven to be successful in Si-SiGe and can be also applied to Si-MOS devices [4]. Alternatively, it is possible to send the rf signal through the accumulation gate by using the larger gate capacitance as coupling mechanism with the charge sensor. Additional confinement gates should then be used to minimize the resistance between the 2DEG and the ohmic and to prevent leakage of the rf signal.

Spin readout can also be performed by detecting the complex impedance of the spin-dependent electron tunneling between quantum dots. This approach is particularly beneficial as the number of qubits to control increases, since it does not rely on nearby charge sensors. Gate-based spin readout can be achieved by connecting off-chip lumped element resonators [6, 7] or on-chip superconducting resonators [8]. In the latter case, single-shot readout can be performed in μs timescales. Here, Si-MOS again presents the challenge of inherently larger parasitic capacitances, but these can be overcome using the same expedients discussed before.

8.1.2. QUBIT CONTROL

Chapter 5 shows universal control of a two-qubit system with the CROT gate fidelity limited to 86%. Chapter 6 discusses new implementations of two-qubit gates on the same device and predicts fidelities above that fault tolerant-threshold, even though more quantitative measurements, like randomized benchmarking or quantum process tomography, are needed to confirm the quality of the gates.

The relatively short dephasing times of $2-3\,\mu s$ are one of the main limiting factors for the two-qubit gates performances. These are of particular relevance in the case of the CROT, given the longer gate time. As the dephasing times decrease at larger values of exchange interaction, it is particularly beneficial to be able to turn on and off the coupling between the electrons during single- and two-qubit gates. While such a degree of control has been demonstrated in chapter 3, the effect of the barrier gates for the device used in chapter 5 and 6 is less pronounced and the exchange is controlled via the detuning. A factor that can seriously limit the tunnel coupling control is the alignment between the barrier and plunger layers. As confirmed by SEM imaging of different samples, misalignments in our devices can amount up to 10-20 nm, which can drastically affect the influence of the barrier gates, these being 30-40 nm in width. For this reason we have started in our group the procedure of inspecting the devices with atomic force microscopy (AFM) during the fabrication process, to ensure that all layers are properly aligned. The improved device tunability, together with the control schemes discussed in chapter 6, should also be able to push the two-qubit operations beyond the fault tolerant thresholds.

The mechanisms affecting the coherence times at these high temperatures also need further investigation. While the temperature dependence of T_1 has been investigated and modeled in detail in chapter 4, the dependence of the dephasing times has been studied over a much smaller range. Other studies [9] have reported a weak temperature dependence from 10 mK up to 1.5 K, but more research is needed to understand the exact underlying physical mechanisms. The qubit noise spectrum could potentially reveal more information about the origin of the noise acting on the qubit. This can be mapped using dynamical decoupling sequences, which effectively can make the qubit sensitive to different parts of the noise spectrum. Recent experiments have shown how, at base fridge temperature, the spectrum follows a $1/f$ frequency dependence over a wide range of frequencies [10]. However, similar investigations at higher temperatures have not been conducted yet.

Once readout and single- and two-qubit gate fidelities have been optimized, experiments can be expanded to include an additional quantum dot. The third qubit can either be used for quantum operations or as an ancilla for readout based on Pauli spin blockade. This would allow for independent readout of the other two spins, simplifying the characterization and the study of the system. Such experiments can be implemented in the same device as the one described in chapter 5 since it features three plunger gates and two barrier gates. In order to maximize the sensitivity, the ancilla qubit should be positioned under the plunger gate which is the closest to the sensor. The main challenge would be here tuning the tunnel couplings between the three electron spins. However, dynamical control of the coupling would only be strictly required for two qubits, while the ancilla qubit and its neighbor could be kept at constant coupling, greatly alleviating the control requirements. A more advanced control scheme would allow for more sophisticated sequences aimed at improving spin-to-charge conversion fidelities and coherence times. Overall, I think these experiments could be far-reaching and, at the same time, perfectly feasible in the short-term period.

8.1.3. ONE AND TWO-DIMENSIONAL QUBIT ARRAYS

Now that many of the fundamental requirements for quantum computation have been realized with spin qubits, the focus is increasingly shifting towards the most relevant challenge: scaling to large-scale quantum systems. Linear quantum dot arrays, hosting up to 12 sites, have already been demonstrated experimentally [11–13], although arbitrary quantum operations have been limited to two qubits. The idea of two-dimensional arrays is also very appealing, because of the larger qubit connectivity that could be employed in quantum algorithms and error correction protocols. Two-dimensional arrays have already been used in GaAs for quantum simulations [14, 15] and demonstrated as a proof-of-principle in CMOS and planar germanium based devices [13, 16–19].

High mobility substrates, like Si-SiGe and Ge-SiGe have an intrinsic advantage in the operation of larger single- and two-dimensional arrays. In fact, their superior mobility guarantees very uniform quantum dots that can be tuned to a high degree of control. On the other hand, Si-MOS quantum dot qubits can count on the reproducibility and yield provided by semiconductor industrial standards, which give prospects that quantum chips can be fabricated in mass-manufacturing facilities. Unsurprisingly, the first demonstrations of two-dimensional arrays in silicon have come from foundry-fabricated devices.

Many of the challenges in moving towards two dimensional structures have already been discussed in chapter 7. These go from readout protocols and qubit driving strategies, to long range coupling mechanisms. With an increased number of qubits, tuning and calibration also become crucial points in spin qubit demonstrations. Automated procedures can greatly speed up experiments and become fundamental when operating large-scale devices. Tuning the charge occupancy and tunnel coupling can now be efficiently automated in linear arrays [11, 20–22], inspired by machine learning and image recognition techniques. What would have an even stronger impact is if also qubit frequencies, Rabi frequencies, exchange interaction and readout sequences could be automated. It is important to note that this requires some significant software developments. Ideally the calibrations routines should be automatically handled by software routines, capable of checking if some parameters need to be updated and in case running the corresponding experiment. In this way all parameters are constantly kept in tune and experiments can be executed much faster.

Undoubtedly building large-scale quantum systems present gigantic challenges. However, the pace at which the field is growing and the strong interest of large tech companies confirms that there is room for optimism. I am confident that the progress we see today is just the tip of the iceberg and that many more achievements will surprise us in the coming years.

REFERENCES

[1] L. A. Tracy, D. R. Luhman, S. M. Carr, N. C. Bishop, G. A. Ten Eyck, T. Pluym, J. R. Wendt, M. P. Lilly, and M. S. Carroll, *Single shot spin readout using a cryogenic high-electron-mobility transistor amplifier at sub-kelvin temperatures,* Applied Physics Letters **108**, 063101 (2016).

[2] R. Schoelkopf, P. Wahlgren, A. Kozhevnikov, P. Delsing, and D. Prober, *The radio-frequency single-electron transistor (rf-set): A fast and ultrasensitive electrometer,* Science **280**, 1238 (1998).

[3] D. Reilly, C. Marcus, M. Hanson, and A. Gossard, *Fast single-charge sensing with a rf quantum point contact,* Applied Physics Letters **91**, 162101 (2007).

[4] E. J. Connors, J. Nelson, and J. M. Nichol, *Rapid high-fidelity spin-state readout in si/si-ge quantum dots via rf reflectometry,* Physical Review Applied **13**, 024019 (2020).

[5] A. Noiri, K. Takeda, J. Yoneda, T. Nakajima, T. Kodera, and S. Tarucha, *Radio-frequency-detected fast charge sensing in undoped silicon quantum dots,* Nano Letters **20**, 947 (2020).

[6] A. West, B. Hensen, A. Jouan, T. Tanttu, C.-H. Yang, A. Rossi, M. F. Gonzalez-Zalba, F. Hudson, A. Morello, D. J. Reilly, *et al.*, *Gate-based single-shot readout of spins in silicon,* Nature Nanotechnology **14**, 437 (2019).

[7] M. Urdampilleta, D. J. Niegemann, E. Chanrion, B. Jadot, C. Spence, P.-A. Mortemousque, L. Hutin, B. Bertrand, S. Barraud, R. Maurand, *et al.*, *Gate-based high fidelity spin read-out in a cmos device,* Nature Nanotechnology **14**, 737 (2019).

[8] G. Zheng, N. Samkharadze, M. L. Noordam, N. Kalhor, D. Brousse, A. Sammak, G. Scappucci, and L. M. Vandersypen, *Rapid gate-based spin read-out in silicon using an on-chip resonator,* Nature Nanotechnology **14**, 742 (2019).

[9] C. H. Yang, R. Leon, J. Hwang, A. Saraiva, T. Tanttu, W. Huang, J. C. Lemyre, K. W. Chan, K. Tan, F. E. Hudson, *et al.*, *Operation of a silicon quantum processor unit cell above one kelvin,* Nature **580**, 350 (2020).

[10] J. Yoneda, K. Takeda, T. Otsuka, T. Nakajima, M. R. Delbecq, G. Allison, T. Honda, T. Kodera, S. Oda, Y. Hoshi, *et al.*, *A quantum-dot spin qubit with coherence limited by charge noise and fidelity higher than 99.9%,* Nature Nanotechnology **13**, 102 (2018).

[11] C. Volk, A. Zwerver, U. Mukhopadhyay, P. Eendebak, C. Van Diepen, J. Dehollain, T. Hensgens, T. Fujita, C. Reichl, W. Wegscheider, *et al.*, *Loading a quantum-dot based "qubyte" register,* npj Quantum Information **5**, 1 (2019).

[12] D. Zajac, T. Hazard, X. Mi, E. Nielsen, and J. R. Petta, *Scalable gate architecture for a one-dimensional array of semiconductor spin qubits,* Physical Review Applied **6**, 054013 (2016).

[13] W. Lawrie, H. Eenink, N. Hendrickx, J. Boter, L. Petit, S. Amitonov, M. Lodari, B. Paquelet Wuetz, C. Volk, S. Philips, *et al.*, *Quantum dot arrays in silicon and germanium,* Applied Physics Letters **116**, 080501 (2020).

[14] T. Hensgens, T. Fujita, L. Janssen, X. Li, C. J. Van Diepen, C. Reichl, W. Wegscheider, S. Das Sarma, and L. M. K. Vandersypen, *Quantum simulation of a Fermi–Hubbard model using a semiconductor quantum dot array,* Nature **548**, 70 (2017).

[15] J. P. Dehollain, U. Mukhopadhyay, V. P. Michal, Y. Wang, B. Wunsch, C. Reichl, W. Wegscheider, M. S. Rudner, E. Demler, and L. M. Vandersypen, *Nagaoka ferromagnetism observed in a quantum dot plaquette,* Nature **579**, 528 (2020).

[16] N. Hendrickx, W. Lawrie, L. Petit, A. Sammak, G. Scappucci, and M. Veldhorst, *A single-hole spin qubit,* Nature Communications **11**, 1 (2020).

[17] F. Ansaloni, A. Chatterjee, H. Bohuslavskyi, B. Bertrand, L. Hutin, M. Vinet, and F. Kuemmeth, *Single-electron control in a foundry-fabricated two-dimensional qubit array,* arXiv preprint arXiv:2004.00894 (2020).

[18] E. Chanrion, D. J. Niegemann, B. Bertrand, C. Spence, B. Jadot, J. Li, P.-A. Mortemousque, L. Hutin, R. Maurand, X. Jehl, *et al.*, *Charge detection in an array of cmos quantum dots,* arXiv preprint arXiv:2004.01009 (2020).

[19] W. Gilbert, A. Saraiva, W. H. Lim, C. H. Yang, A. Laucht, B. Bertrand, N. Rambal, L. Hutin, C. C. Escott, M. Vinet, *et al.*, *Single-electron operation of a silicon-cmos 2x2 quantum dot array with integrated charge sensing,* arXiv preprint arXiv:2004.11558 (2020).

[20] C. Van Diepen, P. T. Eendebak, B. T. Buijtendorp, U. Mukhopadhyay, T. Fujita, C. Reichl, W. Wegscheider, and L. M. Vandersypen, *Automated tuning of inter-dot tunnel coupling in double quantum dots,* Applied Physics Letters **113**, 033101 (2018).

[21] A. Mills, M. Feldman, C. Monical, P. Lewis, K. Larson, A. Mounce, and J. R. Petta, *Computer-automated tuning procedures for semiconductor quantum dot arrays,* Applied Physics Letters **115**, 113501 (2019).

[22] S. S. Kalantre, J. P. Zwolak, S. Ragole, X. Wu, N. M. Zimmerman, M. D. Stewart, and J. M. Taylor, *Machine learning techniques for state recognition and auto-tuning in quantum dots,* npj Quantum Information **5**, 1 (2019).

SUMMARY

In the last decade silicon has emerged as a potential material platform for quantum information. The main attraction comes from the fact that silicon technologies have been developed extensively in the last semiconductor revolution, and this gives hope that quantum dots can be fabricated one day with the same ease transistors are made today. However, building a large-scale quantum computer presents also complications that go beyond fabrication. The heat-dissipation challenge is one of these. As many other qubit platforms, also quantum dot qubits are cooled down at temperatures close to absolute zero in order to overcome the problem of decoherence. While this can be advantageous in few-qubit experiments, it becomes soon impractical as the qubit number increases. The first part of the thesis describes a series of experiments that demonstrate how Si-MOS quantum dot qubits can be successfully operated beyond one Kelvin, where the increase in cooling power is substantial.

The first step is to demonstrate that electrons have sufficiently large energy scales to be properly isolated and controlled at these high temperatures. In the first experimental chapter of the thesis we demonstrate a highly uniform double quantum dot system at the temperature of 0.5 K. The on-chip single-electron-transistor (SET) shows very regular oscillations and an exceptional sensitivity to dot-reservoir and interdot transitions. The electrons in the quantum dot can also be completely decoupled from the reservoir, resulting in a fully isolated system. In order to perform quantum operations it is not only crucial to isolate electrons, but also to couple them. While this is routinely achieved in Si-SiGe heterostructures, it is usually more challenging in Si-MOS due to the larger disorder at the Si-SiO$_2$ interface. However, we find that in the same device we can control the tunnel coupling between the electrons, in a range from below 1 Hz up to 13 GHz. This would allow to isolate the electrons for single-qubit operations and to couple them for two-qubit gates or readout using Pauli spin blockade.

Part of the challenges concerning operation of 'hot' spin qubits lies in the temperature dependence of two parameters: the spin lifetime and the charge noise, which are thoroughly studied in chapter 4. The spin lifetime is usually very long in silicon, due to a weak spin-orbit coupling, and it can approach seconds at low magnetic fields. However, the temperature increases the excitations in the phonon bath and activates two-phonon transitions, which have a steep temperature dependence. These processes, which we experimentally find to start around 500 mK, can ultimately limit qubit performances. However, the spin lifetime can be significantly improved by working in a low magnetic field and high valley splitting regime. Si-MOS quantum dot qubits have a large valley splitting, usually of several hundreds of µeV, and a low magnetic field can be set by reading out the qubits with Pauli spin blockade. This guarantees that useful spin lifetimes can still be found at temperatures close to one Kelvin. In particular, in chapter 4 we measure values exceeding 1 ms at 1.1 K, and discuss how they can be further improved in case of a larger valley splitting.

The second parameter with an important temperature dependence is the charge noise. Electrical fluctuations are of particular relevance in quantum dots because they can couple to the spins as effective magnetic noise via several mechanisms. These can be spin-orbit coupling, magnetic gradients coming from micro magnets or a finite exchange interaction. In quantum dots, defects that can trap or release charges give rise to such electrical fluctuations. These are thermally activated processes and are therefore affected by temperature. By using an on-chip single-electron-transistor as charge sensor, we measure these fluctuations and find a linear temperature dependence from 10 mK up to 4 K. Such a moderate increase is highly beneficial for ‘hot’ qubits, since it suggests that qubit operation will only moderately affected by temperature.

Having characterized the two main temperature dependent parameters, the next chapter shows ‘hot’ qubit control. This is achieved in a Si-MOS double quantum dot operated at 1.1 K, where readout happens via Pauli spin blockade to limit the impact of temperature. This allows also to lower the operating magnetic field to 0.25 T, which softens the requirements for the control electronics. The two qubits show coherence times above 2 µs, which allow for control fidelities above 99%. As opposed to the spin lifetime, the dephasing time is expected to show a much weaker temperature dependence and this is confirmed by measuring a nearly flat dependence between 0.5 and 1.2 K.

Universal quantum computation requires also a universal two-qubit gate, which can be realized by turning on the exchange interaction between the electrons. This shifts the resonance frequencies of the two qubits and enables the execution of coherent controlled rotations (CROTs). The universality of the gate set can be demonstrated via two-qubit randomized benchmarking, where we find a two-qubit CROT fidelity of 86%.

The CROT fidelity is limited by the slow gate time of 660 ns, which is comparable to the coherence times of the two qubits. However, pulsing the exchange interaction can be used to realize different two-qubit gates, such as the CPHASE and the SWAP, which can be executed on much faster time scales. Chapter 6 demonstrates these operations on the same device operating a 1.1 K, achieving a CPHASE gate in 67 ns and a SWAP gate in 89 ns. These two gates are usually mutually exclusive, since the SWAP requires an exchange interaction much larger than the Zeeman splitting, while a CPHASE requires the opposite condition. However, by designing composite sequences we overcome these limitations and demonstrate both gates simultaneously. The performances of both gates are assessed via numerical simulations, which include electrical noise, and we find fidelities exceeding 99%.

One of the greatest challenges in quantum computing today is to design qubit architectures. In the case of quantum dots, this is complicated by the high number of input-output (IOs) connectors that every qubit requires. Wiring large systems with a similarly high number of IOs will inevitably result in an interconnect bottleneck. The last chapter of the this thesis addresses this issue, by proposing a qubit architecture based on a shared number of lines. The architecture consists of a two-dimensional grid where single-gates control multiple plungers and barrier gates, for a total number of wires which scales as the square root of the number of qubits. Single-qubit control is achieved by using a global electron-spin-resonance (ESR) stripline and shaped pulsing, while the $\sqrt{\mathrm{SWAP}}$ is the implemented universal two-qubit gate. Efficient quantum computing schemes requires simultaneous operations. The proposed architecture supports parallel operation, by appropriately shuttling the qubits to different sites. Overall, despite the shared control, arbitrary high-fidelity quantum operations can be realized in the grid, paving the way to large-scale quantum computation in the near future.

Luca Petit

SAMENVATTING

In het laatste decennium is silicium opgekomen als een potentieel materiaal voor quantuminformatietechnologie. Een van de belangrijkste redenen hiertoe is het feit dat de siliciumtechnologie sterk ontwikkeld is ten tijde van de halfgeleiderrevolutie, wat de hoop geeft dat quantum dots in de toekomst met hetzelfde gemak gefabriceerd kunnen worden als transistors vandaag. Echter, het bouwen van een quantumcomputer op grote schaal omvat meer complicaties dan alleen de fabricage. Een van de uitdagingen is het omgaan met de warmtedissipatie. Zoals bij vele andere qubitplatforms, worden quantum dots afgekoeld tot nabij het absolute nulpunt om decoherentie van de quantumstaat te minimaliseren. Alhoewel dit voordelig kan zijn in experimenten met een klein aantal qubits, is de lage temperatuur onpraktisch wanneer het aantal qubits groter wordt. Het eerste deel van dit proefschrift beschrijft een serie experimenten waarin gedemonstreerd wordt hoe Si-MOS quantum dot qubits succesvol gebruikt kunnen worden op een temperatuur van boven één Kelvin, waar het beschikbare koelvermogen substantieel groter is.

De eerste stap hiertoe is het demonstreren dat de energieschaal van de elektronstaat bij de verhoogde temperatuur nog dusdanig groot is dat het elektron geïsoleerd en beïnvloed kan worden. In het eerste experimentele hoofdstuk van dit proefschrift demonstreren we een zeer uniform dubbelquantumdotsysteem op een temperatuur van 0.5 K. De enkel-elektrontransistor laat regelmatige oscillaties en een exceptionele gevoeligheid voor dot-reservoir- en interdottransities zien. De elektronen in de quantum dot kunnen volledig ontkoppeld worden van het ladingsreservoir, om zo een volledig geïsoleerd systeem te vormen. Om quantumoperaties uit te kunnen voeren is het essentieel om de elektronen niet alleen te kunnen isoleren, maar ook te kunnen koppelen. Alhoewel dit regelmatig gedemonstreerd is in Si-SiGe heterostructuren, is het typisch lastiger in Si-MOS vanwege de grotere wanorde die aanwezig is op het Si-SiO$_2$ grensvlak. Wij demonsteren echter dat de tunnelkoppeling tussen de elektronen in hetzelfde device over een bereik van één Hz tot dertien GHz gecontroleerd kan worden. Dit maakt het mogelijk om de elektronen dynamisch te isoleren voor het uitvoeren van eenqubitoperaties en te koppelen voor het uitvoeren van tweequbitoperaties of uitlezing middels Paulispinblokkade.

Een van de uitdagingen bij het werken met 'warme' spin qubits is de temperatuursafhankelijkheid van zowel de vervaltijd van de spinstaat alsmede van de ladingsruis. Deze afhankelijkheden worden beide bestudeerd in hoofdstuk 4. Door de kleine spinbaankoppeling is de spinvervaltijd over het algemeen zeer lang in silicium en deze kan bij lage magneetvelden enkele secondes bedragen. Echter, door het verhogen van de temperatuur wordt ook het fononbad sterker aangeslagen, waardoor tweefonontransitities met een steile temperatuursafhankelijkheid geactiveerd worden. Deze processen, waarvan wij zien dat ze bij 500 mK op beginnen te spelen, kunnen uiteindelijk de qubitprestaties verminderen. De vervaltijd van de spin kan echter worden verbeterd door te werken in een regime van laag magneetveld en grote valleisplitsing. Si-MOS quantum dots hebben over het algemeen een grote valleisplitsing van enkele honderden microelektronvolts en het doen van Paulispinblokkade-uitlezing maakt het werken met lage magneetvelden mogelijk. Dit tezamen zorgt ervoor dat de vervaltijd bij een temperatuur van één Kelvin nog altijd groot genoeg kan zijn. In hoofdstuk 4 rapporteren we vervaltijden van groter dan 1 milliseconde op een temperatuur van 1.1 K en bespreken we hoe deze nog verder verbeterd kunnen worden wanneer de valleisplitsing groter is.

De tweede relevante parameter is de ladingsruis. Het is noodzakelijk om deze elektrische fluctuaties te beschouwen, aangezien ze in quantum dots via verschillende mechanismen aan de spinstaat kunnen koppelen. Deze koppeling kan gemedieerd worden door bijvoorbeeld spin-baankoppeling, een gradient in het magneetveld, veroorzaakt door een micromagneet, of een eindige exchange-interactie. In quantum dot qubits kunnen dit soort ladingsfluctuaties veroorzaakt worden door defecten in de kristalstructuur die een lading opsluiten of loslaten. Dit is een thermisch geactiveerd proces en is daarom afhankelijk van de temperatuur van het systeem. We kunnen deze fluctuaties meten door een geïntegreerde enkel-elektrontransistor te gebruiken als ladingssensor en observeren een lineaire temperatuursafhankelijkheid van de fluctuaties tussen de 10 mK en 4 K. Deze gematigde stijging is veelbelovend voor het opereren van 'warme' qubits, aangezien het suggereert dat de invloed van de temperatuur op de qubitwerking slechts beperkt is.

Nu het effect van de temperatuur op de twee belangrijkste parameters gekarakteriseerd is, vervolgt het volgende hoofdstuk met het opereren van een 'warme' qubit. Dit wordt bereikt in een Si-MOS dubbele quantum dot op een temperatuur van 1.1 K, waarbij uitlezing uitgevoerd wordt middels Paulispinblokkade om het effect van de temperatuur hierop te minimaliseren. Dit stelt ons ook in staat om het magneetveld te verlagen tot 0.25 T, hetgeen tevens de eisen die aan de bedieningselektronica gesteld worden, versoepelt. De twee qubits hebben coherentietijden van boven de twee microseconde, wat zorgt voor een controlebetrouwbaarheid van de qubits van boven de 99%. Van de coherentietijd van de spin wordt verwacht dat deze, in tegenstelling tot de vervaltijd, een zeer kleine afhankelijkheid van de temperatuur vertoont. Dit wordt bevestigd door de vrijwel vlakke afhankelijkheid die we observeren tussen de 0.5 en 1.2 K.

Om universele quantumberekeningen mogelijk te maken, is het noodzakelijk om ook te beschikken over een tweequbitpoort. Deze poort kan verkregen worden door de exchange-interactie tussen de qubits aan te zetten, waardoor de resonantiefrequenties van de twee qubits verschuiven. Dit maakt het mogelijk om gecontroleerde coherente rotaties (CROTs) uit te voeren. De universaliteit van de verzameling quantumpoorten kan worden gedemonstreerd middels twee-qubit randomized benchmarking, waarmee we een CROT-betrouwbaarheid van de twee qubits van 86% vinden.

De CROT-betrouwbaarheid wordt beperkt door de relatief lange duur van de operatie van 660 nanoseconde, vergelijkbaar met de coherentietijd van de twee qubits. Echter, door de exchange¬-interactie te pulseren, kan ook een ander type twee-qubitpoort gemaakt worden, zoals bijvoorbeeld de CPHASE- en de SWAP-poorten, die beiden een veel kortere tijdsduur hebben. In hoofdstuk 6 demonstreren we deze beide operaties op hetzelfde device bij een temperatuur van 1.1 K, waarbij een CPHASE-poort in 67 ns en de SWAP-poort in 89 ns bereikt kan worden. Deze twee poorten zijn normaliter wederzijds exclusief, aangezien de SWAP-poort een exchange-interactie vereist die veel groter is dan het Zeeman-energieverschil, waar de CPHASE-poort de tegenovergestelde eis stelt. Echter, door samengestelde sequenties te ontwerpen, kan deze beperking overkomen worden en kunnen beide poorten tegelijk worden uitgevoerd. De kwaliteit van beide poorten is via numerieke simulaties beoordeeld, waarbij ook elektrische ruis in beschouwing genomen wordt, en we vinden betrouwbaarheden van groter dan 99%. Een van de grootste uitdagingen op de weg naar de quantum computer is het ontwerpen van een qubitarchitectuur. In het geval van quantum dots wordt dit gecompliceerd door het grote aantal ingang- en uitgangverbindingen (IO's) dat elke qubit vereist. Het aansluiten van een groot systeem met een even groot aantal IO's zal onvermijdelijk leiden tot een knelpunt bij het maken van deze verbindingen. Het laatste hoofdstuk pakt dit punt aan doormiddel van een voorgestelde qubitarchitectuur gebaseerd op gedeelde aanstuurlijnen. De architectuur bestaat uit een tweedimensionaal rooster, waarbij enkele lijnen meerdere plunjer- en barrière-elektrodes aansturen, om zo tot een totaal aantal aansluitingen te komen dat schaalt met de vierkantswortel van het aantal qubits. Eenqubitpoorten worden uitgevoerd doormiddel van een globale elektron-spinresonantie striplijn en voorgevormde pulsen, terwijl de $\sqrt{\text{SWAP}}$-poort gebruikt wordt als universele tweequbitpoort. Om efficiënte quantumberekingen uit te kunnen voeren, is noodzakelijk dat er simultaan operaties uitgevoerd kunnen worden. De voorgestelde architectuur ondersteunt dit door de qubits tussen verschillende posities in het rooster heen-en-weer te bewegen. Het zou daarom mogelijk moeten zijn om zeer hoge betrouwbaarheid quantumoperaties uit te voeren, ondanks de gedeelde aanstuurlijnen, om op die manier de weg vrij te maken voor quantumberekingen op grote schaal in de nabije toekomst.

Luca Petit

Curriculum Vitæ

Luca Petit

14-07-1992	Born in Rome, Italy.
2011-2014	**Bachelor in Physics** *cum Laude*. Università degli studi di Roma La Sapienza *Thesis:* Study of the low temperature photoluminescence spectra of InP.
2014-2016	**Master's joint degree in Nanotechnologies for ICTs** *cum Laude*. Politecnico di Torino, Grenoble INP Phelma and Ecole Polytechnique Fédérale de Lausanne. *Thesis:* Scanning Probe Thermometry of Metal-Insulator Transition Oxides.
2015	**Research Intern**. Nanoelectronic Devices Laboratory – Ecole Polytechnique Fédérale de Lausanne. Simulations of CMOS devices exploiting the metal-insulator transition of VO_2.
2016	**Research Intern**. IBM Research - Zurich Laboratory. Development and operation of a vacuum thermal scanning probe microscope.
2016-2020	**PhD. Physics** Delft University of Technology *Thesis:* Universal quantum logic in hot silicon qubits.

LIST OF PUBLICATIONS

10. **L. Petit**, M. Russ, H.G.J. Eenink, W.I.L. Lawrie, J.S. Clarke, L.M.K. Vandersypen, M. Veldhorst, *High-fidelity two-qubit gates in silicon above one Kelvin*, arXiv preprint arXiv:2007.09034 (2020).
9. W.I.L. Lawrie, N.W. Hendrickx, F. van Riggelen, M. Russ, **L. Petit**, A. Sammak, G. Scappucci, M. Veldhorst, *Spin relaxation benchmarks and individual qubit addressability for holes in quantum dots*, **Nano letters 20** (10), 7237–7242, (2020)
8. N.W. Hendrickx, W.I.L. Lawrie, **L. Petit**, A. Sammak, G. Scappucci, M. Veldhorst, *A single-hole spin qubit*, **Nature Communications 11**, (2020).
7. **L. Petit**, H.G.J. Eenink, M. Russ, W.I.L. Lawrie, N.W. Hendrickx, J.S. Clarke, L.M.K. Vandersypen, M. Veldhorst, *Universal quantum logic in hot silicon qubits*, **Nature 580**, 355-359 (2020).
6. W.I.L. Lawrie, H.G.J. Eenink, N.W. Hendrickx, J.M. Boter, **L. Petit**, S.V. Amitonov, M. Lodari, B. Paquelet Wuetz, C. Volk, S.G.J. Philips, G. Droulers, N. Kalhor, F. van Riggelen, D. Brousse, A. Sammak, L.M.K. Vandersypen, G. Scappucci, M. Veldhorst, *Quantum Dot Arrays in Silicon and Germanium*, **Applied Physics Letters 116**, 080501 (2020).
5. H.G.J. Eenink*, **L. Petit***, W.I.L. Lawrie, J.S. Clarke, L.M.K. Vandersypen, M. Veldhorst, *Tunable Coupling and Isolation of Single Electrons in Silicon Metal-Oxide-Semiconductor Quantum Dots*, **Nano letters 19** (12), 8653-8657 (2019).
4. **L. Petit**, J.M. Boter, H.G.J. Eenink, G. Droulers, M.L.V. Tagliaferri, R. Li, D.P. Franke, K.J. Singh, J.S. Clarke, R.N. Schouten, V.V. Dobrovitski, L.M.K. Vandersypen, M. Veldhorst, *Spin lifetime and charge noise in hot silicon quantum dot qubits*, **Physical Review Letters 121** (7), 076801 (2018).
3. R. Li, **L. Petit**, D. P. Franke, J. P. Dehollain, J. Helsen, M. Steudtner, N. K. Thomas, Z. R. Yoscovits, K. J. Singh, S. Wehner, L. M. K. Vandersypen, J. S. Clarke, M. Veldhorst, *A crossbar network for silicon quantum dot qubits*, **Science Advances 4** (7), eaar3960 (2018).
2. W. A. Vitale, M. Tamagnone, C. F. Moldovan, N. Émond, E. A. Casu, **L. Petit**, B. L. Drogoff, Mo. Chaker, J. R. Mosig, A. M. Ionescu, *Field-enhanced design of steep-slope VO_2 switches for low actuation voltage*, **46th European Solid-State Device Research Conference (ESSDERC)**, 352-355 (2016).
1. W. A. Vitale, **L. Petit**, C. F. Moldovan, M. Fernández-Bolaños, A. Paone, A. Schüler, A. M. Ionescu, *Electrothermal actuation of vanadium dioxide for tunable capacitors and microwave filters with integrated microheaters*, **Sensors and Actuators A: Physical 241**, 245-253 (2016).

---

*These authors contributed equally to the work.